

The Vera C. Rubin Observatory Data Preview 1

1
2
3
4
5
6
7
8
9
10
11
12
13
14
15
16
17
18
19
20
21
22
23
24
25
26
27
28
29
30
31
32
33
34
35
36
37
38
39
40
41
42
43
44
45
46
47
48
49

VERA C. RUBIN OBSERVATORY TEAM,¹ TATIANA ACERO-CUELLAR ² EMILY ACOSTA ¹ CHRISTINA L. ADAIR ³
PRAKRUTH ADARI ⁴ JENNIFER K. ADELMAN-McCARTHY ⁵ ANASTASIA ALEXOV ¹ RUSS ALLBERY ¹
ROBYN ALLSMAN,¹ YUSRA ALSAYYAD ⁶ JHONATAN AMADO ⁵ NATHAN AMOUROUX ⁷ PIERRE ANTILOGUS ⁸
ALEXIS ARACENA ALCAYAGA,⁹ GONZALO ARAVENA-ROJAS ⁹ CLAUDIO H. ARAYA CORTES,⁹ ÉRIC AUBOURG ¹⁰
TIM S. AXELROD ¹¹ JOHN BANOVETZ ¹² CARLOS BARRÍA,⁹ AMANDA E. BAUER ¹³ BRIAN J. BAUMAN,¹⁴
ELLEN BECHTOL ¹⁵ KEITH BECHTOL ^{1,16} ANDREW C. BECKER ¹⁷ VALERIE R. BECKER ¹⁸ MARK G. BECKETT ¹⁹
ERIC C. BELLM ²⁰ PEDRO H. BERNARDINELLI ²¹ FEDERICA B. BIANCO ^{2,22,23} ROBERT D. BLUM ¹⁸
JOANNE BOGART,²⁴ ADAM BOLTON ³ MICHAEL T. BOOTH,¹ JAMES F. BOSCH ⁶ ALEXANDRE BOUCAUD ²⁵
DOMINIQUE BOUTIGNY ⁷ ROBERT A. BOVILL,¹ ANDREW BRADSHAW,^{3,24} JOHAN BREGEON ²⁶ BRIAN J. BRONDEL ²⁷
ALEXANDER BROUGHTON ²⁴ AUDREY BUDLONG ²⁸ DIMITRI BUFFAT,²⁶ RODOLFO CANESTRARI ²⁹
NEVEN CAPLAR ²⁰ JEFFREY L. CARLIN ¹ ROSS CEBALLO ¹⁸ COLIN ORION CHANDLER ^{30,20,31}
CHIHWAY CHANG ³² GLENAVER CHARLES-EMERSON,¹ HSIEN-FANG CHIANG ³ JAMES CHIANG ²⁴ YUMI CHOI ³³
ERIC J. CHRISTENSEN,⁹ CHARLES F. CLAVER,¹ ANDY W. CLEMENTS,¹ JOSEPH J. COCKRUM,¹ FRANCO COLLEONI,⁹
CÉLINE COMBET ²⁶ ANDREW J. CONNOLLY ²¹ JULIO EDUARDO CONSTANZO CÓRDOVA ⁹ HANS E CONTRERAS,⁹
JOHN FRANKLIN CRENSHAW ²¹ SYLVIE DAGORET-CAMPAGNE ³⁴ SCOTT F. DANIEL,²⁰ FELIPE DARUICH,⁹
GUILLAUME DAUBARD ⁸ GREG DAUES,³⁵ ERIK DENNIHY ¹ STEPHANIE J. H. DEPPE ¹⁸ SETH W. DIGEL ³
PETER E. DOHERTY,³⁶ ALEX DRLICA-WAGNER ⁵ GREGORY P. DUBOIS-FELSMANN ³⁷ FROSSIE ECONOMOU ¹
ORION EIGER ^{3,24} LUKAS EISERT ³ ALAN M. EISNER ³⁸ ANTHONY ENGLERT ³⁹ BADEN ERB,⁹ JUAN A. FABREGA,⁹
PARKER FAGRELIUS,¹ KEVIN FANNING ³ ANGELO FAUSTI NETO ¹ PETER S. FERGUSON ^{21,16} AGNÈS FERTÉ ³
MERLIN FISHER-LEVINE ⁴⁰ GLORIA FONSECA ALVAREZ ³³ MICHAEL D. FOSS,³ DOMINIQUE FOCHEZ ⁴¹
DAN C. FUCHS ³ EMMANUEL GANGLER ⁴² IGOR GAPONENKO,³ JULEN GARCIA ⁴³ JOHN H GATES,³
RANPAL K. GILL ²⁷ ENRICO GIRO ⁴⁴ THOMAS GLANZMAN ³ ROBINSON GODOY,⁹ IAIN GOODENOW,¹
MIRANDA R. GORSUCH ¹⁶ MICHELLE GOWER ³⁵ MIKAEL GRANVIK ^{45,46} SARAH GREENSTREET ³³ WEN GUAN ¹²
THIBAUT GUILLEMIN ⁷ LEANNE P. GUY ⁹ DIANE HASCALL,³ AREN NATHANIEL HEINZE ²¹ FABIO HERNANDEZ ⁴⁷
KENNETH HERNER ⁵ ARDIS HERROLD,¹ CLARE R. HIGGS ¹⁸ JOSHUA HOBLITT ¹ ERIN LEIGH HOWARD ²⁰
MINHEE HYUN ⁹ PATRICK INGRAHAM ¹¹ DAVID H. IRVING ¹⁸ ŽELJKO IVEZIĆ ^{1,20} SUZANNE H. JACOBY,¹
BUELL T. JANNUZI ⁴⁸ SREEVANI JARUGULA ⁵ M. JAMES JEE ^{49,50} TIM JENNESS ¹ TOBY C. JENNINGS ³
ANDREA JEREMIE ⁷ GARRETT JERNIGAN,^{51,*} DAVID JIMÉNEZ MEJÍAS,⁹ ANTHONY S. JOHNSON ³ R. LYNNE JONES ²⁰
ROGER WILLIAM LEWIS JONES ⁵² CLAIRE JURAMY-GILLES ⁸ MARIO JURÍĆ ²¹ STEVEN M. KAHN ⁵³
J. BRYCE KALMBACH ³ YIJUNG KANG ^{24,9} ARUN KANAWADI ^{54,6} JEFFREY P. KANTOR,¹ EDWARD KARAVAKIS ¹²
KSHITIJ KELKAR ⁹ LEE S. KELVIN ⁶ IVAN V. KOTOV,¹² GÁBOR KOVÁCS ²¹ MIKOLAJ KOWALIK ³⁵
VICTOR L. KRABBENDAM,¹ K. SIMON KRUGHOFF ^{1,*} PETR KUBÁNEK ⁹ JACOB A. KURLANDER ²¹ MILE KUSULJA,²⁶
CRAIG S. LAGE ⁵⁰ PAULO J. A. LAGO ²⁷ KATHERINE LALLOTIS ⁵⁵ TRAVIS LANGE ³ DIDIER LAPORTE,⁸
RYAN M. LAU ³³ JUAN CARLOS LAZARTE,³ QUENTIN LE BOULC'H ⁴⁷ PIERRE-FRANÇOIS LÉGET ⁶
LAURENT LE GUILLOU ⁸ BENJAMIN LEVINE ⁴ MING LIANG,¹ SHUANG LIANG,³ KIAN-TAT LIM ³
ANJA VON DER LINDEN ⁴ HUAN LIN ⁵ MARGAUX LOPEZ ³ JUAN J. LOPEZ TORO,⁹ PETER LOVE,⁵²
ROBERT H. LUPTON ⁶ NATE B. LUST ⁶ LAUREN A. MACARTHUR ⁶ SEAN PATRICK MACBRIDE ⁵⁶
GREG M. MADEJSKI,²⁴ GABRIELE MAINETTI ⁴⁷ STEVEN J. MARGHEIM ²⁷ THOMAS W. MARKIEWICZ ³
PHIL MARSHALL ³ STUART MARSHALL,²⁴ GUIDO MAULEN,⁹ MORGAN MAY,^{57,12} JEREMY McCORMICK ³
DAVID MCKAY ⁵⁸ ROBERT MCKERCHER,¹ GUILLEM MEGIAS HOMAR ⁵⁹ AARON M. MEISNER ³³
FELIPE MENANTEAU,³⁵ HEATHER R. MENTZER ³⁸ KRISTEN METZGER,¹⁸ JOSHUA E. MEYERS ²⁴ MICHELLE MILLER,³³
DAVID J. MILLS,¹ JOACHIM MOEYENS ²¹ MARC MONIEZ,³⁴ FRED E. MOOLEKAMP ⁶⁰ C. A. L. MORALES MARÍN ⁹
FRITZ MUELLER ³ JAMES R. MULLANEY ⁶¹ FREDDY MUÑOZ ARANCIBIA,¹ KATE NAPIER ²⁴ HOMER NEAL,³
ERIC H. NEILSEN, JR. ⁵ JEREMY NEVEU ³⁴ TIMOTHY NOBLE,⁶² ERFAN NOURBAKHSH ⁶ KNUT OLSEN ³³
WILLIAM O'MULLANE ⁹ DMITRY ONOPRIENKO,³ MARCO ORIUNNO ³ SHAWN OSIER,³ RUSSELL E. OWEN,²⁰
AASHAY PAI ³² JOHN K. PAREJKO ²⁰ HYE YUN PARK ⁵⁴ JAMES B. PARSONS,^{35,*} MARIA T. PATTERSON ²⁰
MARINA S. PAVLOVIC ⁹ KARLA PEÑA RAMÍREZ ⁹ JOHN R. PETERSON ⁶³ STEPHEN R. PIETROWICZ ³⁵
ANDRÉS A. PLAZAS MALAGÓN ^{3,24} REBEKAH POLEN,⁵⁴ HANNAH MARY MARGARET POLLEK,³ PAUL A. PRICE ⁶

Corresponding author: Leanne P. Guy; Tim Jenness; James Mullaney

BRUNO C. QUINT¹, JOSÉ MIGUEL QUINTERO MARIN,⁹ MARKUS RABUS¹,⁶⁴ BENJAMIN RACINE¹,⁴¹ VELJKO RADEKA,¹²
 MANON RAMEL,²⁶ ARIANNA RANABHAT¹,⁶⁵ ANDREW P. RASMUSSEN¹,²⁴ DAVID A. RATHFELDER,⁶⁶
 MEREDITH L. RAWLS¹,^{20,21} SOPHIE L. REED¹,⁶ KEVIN A. REIL¹,³ DAVID J. REISS,²⁰ MICHAEL A. REUTER¹,¹
 TIAGO RIBEIRO¹,¹ MICKAEL RIGAUT¹,⁶⁷ VINCENT J. RIOT¹,¹⁴ STEVEN M. RITZ¹,³⁸ MARIO F. RIVERA RIVERA,⁹
 BRANT E. ROBERTSON¹,³⁸ WILLIAM ROBY¹,³⁷ GABRIELE RODEGHIERO¹,⁶⁸ AARON ROODMAN¹,²⁴
 LUCA ROSIGNOLI¹,^{69,68} CÉCILE ROUCELLE¹,²⁵ MATTHEW R. RUMORE¹,¹² STEFANO RUSSO,⁸ ELI S. RYKOFF¹,²⁴
 ANDREI SALNIKOV¹,³ BRUNO O. SÁNCHEZ¹,⁴¹ DAVID SANMARTIN¹,⁹ CLARE SAUNDERS¹,⁶ RAFE H. SCHINDLER,²⁴
 SAMUEL J. SCHMIDT¹,⁵⁰ JACQUES SEBAG,⁹ BRIAN SELVY,¹ EDGARD ESTEBAN SEPULVEDA VALENZUELA,⁹
 GONZALO SERICHE¹,⁹ JACQUELINE C. SERON-NAVARETE¹,⁹ IGNACIO SEVILLA-NOARBE¹,⁷⁰ ALYSHA SHUGART¹,⁹
 JONATHAN SICK¹,^{71,1} CRISTIÁN SILVA¹,⁹ MATHEW C. SIMS¹,⁷² JALADH SINGHAL¹,³⁷ KEVIN BENJAMIN SIRUNO,⁹
 COLIN T. SLATER¹,²⁰ BRIANNA M. SMART¹,²⁰ ADAM SNYDER¹,⁵⁰ CHRISTINE SOLDAHL,³
 IOANA SOTUELA ELORRIAGA¹,⁹ BRIAN STALDER¹,¹ HERNAN STOCKEBRAND¹,⁹ ALAN L. STRAUSS¹,¹⁸
 MICHAEL A. STRAUSS¹,⁶ KRZYSZTOF SUBERLAK¹,²⁰ IAN S. SULLIVAN¹,²⁰ JOHN D. SWINBANK¹,^{73,6} DIEGO TAPIA¹,⁹
 ALESSIO TARANTO¹,^{68,69} DAN S. TARANU¹,⁶ JOHN GREGG THAYER¹,³ SANDRINE THOMAS¹,¹
 ADAM J. THORNTON¹,¹ ROBERTO TIGHE,⁹ LAURA TORIBIO SAN CIPRIANO,⁷⁰ TE-WEI TSAI¹,¹ DOUGLAS L. TUCKER¹,⁵
 MAX TURRI,³ J. ANTHONY TYSON¹,⁵⁰ ELANA K. URBACH¹,⁷⁴ YOUSUKE UTSUMI¹,⁷⁵ BRIAN VAN KLAVEREN,³
 WOUTER VAN REEVEN¹,⁹ PETER ANTHONY VAUCHER¹,³ PAULINA VENEGAS,⁹ APRAJITA VERMA¹,⁷⁶
 ANTONIA SIERRA VILLARREAL¹,³ STELIOS VOUTSINAS¹,¹ CHRISTOPHER W. WALTER¹,⁵⁴ YUANKUN (DAVID) WANG¹,²¹
 CHRISTOPHER Z. WATERS¹,⁶ CHRISTINA C. WILLIAMS¹,³³ BETH WILLMAN¹,⁷⁷ MATTHIAS WITTGEN¹,³
 W. M. WOOD-VASEY¹,⁷⁸ WEI YANG¹,³ ZHAOYU YANG¹,¹² BRIAN P. YANNY¹,⁵ PETER YOACHIM¹,²⁰
 TIANQING ZHANG¹,⁷⁸ AND CONGHAO ZHOU¹,³⁸

¹Vera C. Rubin Observatory Project Office, 950 N. Cherry Ave., Tucson, AZ 85719, USA

²Department of Physics and Astronomy, University of Delaware, Newark, DE 19716-2570, USA

³SLAC National Accelerator Laboratory, 2575 Sand Hill Rd., Menlo Park, CA 94025, USA

⁴Department of Physics and Astronomy, Stony Brook University, Stony Brook, NY 11794, USA

⁵Fermi National Accelerator Laboratory, P. O. Box 500, Batavia, IL 60510, USA

⁶Department of Astrophysical Sciences, Princeton University, Princeton, NJ 08544, USA

⁷Université Savoie Mont-Blanc, CNRS/IN2P3, LAPP, 9 Chemin de Bellevue, F-74940 Annecy-le-Vieux, France

⁸Sorbonne Université, Université Paris Cité, CNRS/IN2P3, LPNHE, 4 place Jussieu, F-75005 Paris, France

⁹Vera C. Rubin Observatory, Avenida Juan Cisternas #1500, La Serena, Chile

¹⁰Université Paris Cité, CNRS/IN2P3, CEA, APC, 4 rue Elsa Morante, F-75013 Paris, France

¹¹Steward Observatory, The University of Arizona, 933 N. Cherry Ave., Tucson, AZ 85721, USA

¹²Brookhaven National Laboratory, Upton, NY 11973, USA

¹³Yerkes Observatory, 373 W. Geneva St., Williams Bay, WI 53191, USA

¹⁴Lawrence Livermore National Laboratory, 7000 East Avenue, Livermore, CA 94550, USA

¹⁵Wisconsin IceCube Particle Astrophysics Center, University of Wisconsin—Madison, Madison, WI 53706, USA

¹⁶Department of Physics, University of Wisconsin-Madison, Madison, WI 53706, USA

¹⁷Amazon Web Services, Seattle, WA 98121, USA

¹⁸Vera C. Rubin Observatory/NSF NOIRLab, 950 N. Cherry Ave., Tucson, AZ 85719, USA

¹⁹Institute for Astronomy, University of Edinburgh, Royal Observatory, Blackford Hill, Edinburgh EH9 3HJ, UK

²⁰University of Washington, Dept. of Astronomy, Box 351580, Seattle, WA 98195, USA

²¹Institute for Data-intensive Research in Astrophysics and Cosmology, University of Washington, 3910 15th Avenue NE, Seattle, WA 98195, USA

²²Joseph R. Biden, Jr., School of Public Policy and Administration, University of Delaware, Newark, DE 19717 USA

²³Data Science Institute, University of Delaware, Newark, DE 19717 USA

²⁴Kavli Institute for Particle Astrophysics and Cosmology, SLAC National Accelerator Laboratory, 2575 Sand Hill Rd., Menlo Park, CA 94025, USA

²⁵Université Paris Cité, CNRS/IN2P3, APC, 4 rue Elsa Morante, F-75013 Paris, France

²⁶Université Grenoble Alpes, CNRS/IN2P3, LPSC, 53 avenue des Martyrs, F-38026 Grenoble, France

²⁷Vera C. Rubin Observatory/NSF NOIRLab, Casilla 603, La Serena, Chile

²⁸University of Washington, Dept. of Physics, Box 351580, Seattle, WA 98195, USA

²⁹INAF Istituto di Astrofisica Spaziale e Fisica Cosmica di Palermo, Via Ugo la Malfa 153, 90146, Palermo, Italy

³⁰LSST Interdisciplinary Network for Collaboration and Computing, Tucson, USA

³¹Department of Astronomy and Planetary Science, Northern Arizona University, P.O. Box 6010, Flagstaff, AZ 86011, USA

³²Department of Astronomy and Astrophysics, University of Chicago, 5640 South Ellis Avenue, Chicago, IL 60637, USA

³³NSF NOIRLab, 950 N. Cherry Ave., Tucson, AZ 85719, USA

- 106 ³⁴ *Université Paris-Saclay, CNRS/IN2P3, IJCLab, 15 Rue Georges Clemenceau, F-91405 Orsay, France*
 107 ³⁵ *NCSA, University of Illinois at Urbana-Champaign, 1205 W. Clark St., Urbana, IL 61801, USA*
 108 ³⁶ *Smithsonian Astrophysical Observatory, 60 Garden St., Cambridge MA 02138, USA*
 109 ³⁷ *Caltech/IPAC, California Institute of Technology, MS 100-22, Pasadena, CA 91125-2200, USA*
 110 ³⁸ *Santa Cruz Institute for Particle Physics and Physics Department, University of California–Santa Cruz, 1156 High St., Santa Cruz,*
 111 *CA 95064, USA*
 112 ³⁹ *Department of Physics, Brown University, 182 Hope Street, Providence, RI 02912, USA*
 113 ⁴⁰ *D4D CONSULTING LTD., Suite 1 Second Floor, Everdene House, Deansleigh Road, Bournemouth, UK BH7 7DU*
 114 ⁴¹ *Aix Marseille Université, CNRS/IN2P3, CPPM, 163 avenue de Luminy, F-13288 Marseille, France*
 115 ⁴² *Université Clermont Auvergne, CNRS/IN2P3, LPCA, 4 Avenue Blaise Pascal, F-63000 Clermont-Ferrand, France*
 116 ⁴³ *C. Iñaki Goenaga, 5, 20600, Guipúzcoa, Spain*
 117 ⁴⁴ *INAF Osservatorio Astronomico di Trieste, Via Giovan Battista Tiepolo 11, 34143, Trieste, Italy*
 118 ⁴⁵ *Department of Physics, P.O. Box 64, 00014 University of Helsinki, Finland*
 119 ⁴⁶ *Asteroid Engineering Laboratory, Luleå University of Technology, Box 848, SE-981 28 Kiruna, Sweden*
 120 ⁴⁷ *CNRS/IN2P3, CC-IN2P3, 21 avenue Pierre de Coubertin, F-69627 Villeurbanne, France*
 121 ⁴⁸ *University of Arizona, Department of Astronomy and Steward Observatory, 933 N. Cherry Ave, Tucson, AZ 85721, USA*
 122 ⁴⁹ *Department of Astronomy, Yonsei University, 50 Yonsei-ro, Seoul 03722, Republic of Korea*
 123 ⁵⁰ *Physics Department, University of California, One Shields Avenue, Davis, CA 95616, USA*
 124 ⁵¹ *Space Sciences Lab, University of California, 7 Gauss Way, Berkeley, CA 94720-7450, USA*
 125 ⁵² *Lancaster University, Lancaster, UK*
 126 ⁵³ *Physics Department, University of California, 366 Physics North, MC 7300 Berkeley, CA 94720, USA*
 127 ⁵⁴ *Department of Physics, Duke University, Durham, NC 27708, USA*
 128 ⁵⁵ *Center for Cosmology and Astro-Particle Physics, The Ohio State University, Columbus, OH 43210, USA*
 129 ⁵⁶ *Physik-Institut, University of Zurich, Winterthurerstrasse 190, 8057 Zurich, Switzerland*
 130 ⁵⁷ *Department of Physics Columbia University, New York, NY 10027, USA*
 131 ⁵⁸ *EPCC, University of Edinburgh, 47 Potterrow, Edinburgh, EH8 9BT, UK*
 132 ⁵⁹ *Division of Physics, Mathematics and Astronomy, California Institute of Technology, Pasadena, CA 91125, USA*
 133 ⁶⁰ *soZen Inc., 105 Clearview Dr, Penfield, NY 14526*
 134 ⁶¹ *Astrophysics Research Cluster, School of Mathematical and Physical Sciences, University of Sheffield, Sheffield, S3 7RH, United*
 135 *Kingdom*
 136 ⁶² *Science and Technology Facilities Council, Rutherford Appleton Laboratory, Harwell, UK*
 137 ⁶³ *Department of Physics and Astronomy, Purdue University, 525 Northwestern Ave., West Lafayette, IN 47907, USA*
 138 ⁶⁴ *Departamento de Matemática y Física Aplicadas, Facultad de Ingeniería, Universidad Católica de la Santísima Concepción, Alonso de*
 139 *Rivera 2850, Concepción, Chile*
 140 ⁶⁵ *Australian Astronomical Optics, Macquarie University, North Ryde, NSW, Australia*
 141 ⁶⁶ *AURA, 950 N. Cherry Ave., Tucson, AZ 85719, USA*
 142 ⁶⁷ *Université Claude Bernard Lyon 1, CNRS/IN2P3, IP2I, 4 Rue Enrico Fermi, F-69622 Villeurbanne, France*
 143 ⁶⁸ *INAF Osservatorio di Astrofisica e Scienza dello Spazio Bologna, Via P. Gobetti 93/3, 40129, Bologna, Italy*
 144 ⁶⁹ *Department of Physics and Astronomy (DIFA), University of Bologna, Via P. Gobetti 93/2, 40129, Bologna, Italy*
 145 ⁷⁰ *Centro de Investigaciones Energéticas, Medioambientales y Tecnológicas, Av. Complutense 40, 28040 Madrid, Spain*
 146 ⁷¹ *J.Sick Codes Inc., Penetanguishene, Ontario, Canada*
 147 ⁷² *Science and Technology Facilities Council, UK Research and Innovation, Polaris House, North Star Avenue, Swindon, SN2 1SZ, UK*
 148 ⁷³ *ASTRON, Oude Hoogeveensedijk 4, 7991 PD, Dwingeloo, The Netherlands*
 149 ⁷⁴ *Department of Physics, Harvard University, 17 Oxford St., Cambridge MA 02138, USA*
 150 ⁷⁵ *National Astronomical Observatory of Japan, Chile Observatory, Los Abedules 3085, Vitacura, Santiago, Chile*
 151 ⁷⁶ *Department of Physics, University of Oxford, Denys Wilkinson Building, Keble Road, Oxford, OX1 3RH, UK*
 152 ⁷⁷ *LSST Discovery Alliance, 933 N. Cherry Ave., Tucson, AZ 85719, USA*
 153 ⁷⁸ *Department of Physics and Astronomy, University of Pittsburgh, 3941 O’Hara Street, Pittsburgh, PA 15260, USA*

(Dated: January 30, 2026)

ABSTRACT

We present Rubin Data Preview 1 (DP1), the first data from the NSF-DOE Vera C. Rubin Observatory, comprising raw and calibrated single-epoch images, coadds, difference images, detection catalogs, and ancillary data products. DP1 is based on 1792 optical/near-infrared exposures acquired over 48 distinct nights by the Rubin Commissioning Camera, LSSTComCam, on the Si-

159 monyi Survey Telescope at the Summit Facility on Cerro Pachón, Chile in late 2024. DP1 covers
 160 ~ 15 deg² distributed across seven roughly equal-sized non-contiguous fields, each independently ob-
 161 served in six broad photometric bands, *ugrizy*. The median FWHM of the point-spread function
 162 across all bands is approximately 1''14, with the sharpest images reaching about 0''58. The 5σ point
 163 source depths for coadded images in the deepest field, the Extended Chandra Deep Field South, are:
 164 $u = 24.55, g = 26.18, r = 25.96, i = 25.71, z = 25.07, y = 23.1$. Other fields are no more than 2.2
 165 magnitudes shallower in any band, where they have nonzero coverage. DP1 contains approximately
 166 2.3 million distinct astrophysical objects, of which 1.6 million are extended in at least one band in
 167 coadds, and 431 solar system objects, of which 93 are new discoveries. DP1 is approximately 3.5 TB
 168 in size and is available to Rubin data rights holders via the Rubin Science Platform, a cloud-based
 169 environment for the analysis of petascale astronomical data. While small compared to future LSST
 170 releases, its high quality and diversity of data support a broad range of early science investigations
 171 ahead of full operations in 2026.

172 *Keywords:* Rubin Observatory – LSST

173 1. INTRODUCTION

174 The National Science Foundation (NSF)–Department
 175 of Energy (DOE) Vera C. Rubin Observatory is a
 176 ground-based, wide-field optical/near-infrared facility
 177 located on Cerro Pachón in northern Chile. Named in
 178 honor of Vera C. Rubin, a pioneering astronomer whose
 179 groundbreaking work in the 20th century provided the
 180 first convincing evidence for the existence of dark mat-
 181 ter (V. C. Rubin & W. K. Ford 1970; V. C. Rubin et al.
 182 1980), the observatory’s prime mission is to carry out the
 183 Legacy Survey of Space and Time (formerly Large Syn-
 184 optic Survey Telescope) (LSST) (Ž. Ivezić et al. 2019a).
 185 This 10-year survey is designed to obtain rapid-cadence,
 186 multi-band imaging of the entire visible southern sky
 187 approximately every 3–4 nights. Over its main 18,000
 188 deg² footprint, the LSST is expected to reach a depth
 189 of ~ 27 magnitude in the r-band, with ~ 800 visits per
 190 pointing in all filters (F. B. Bianco et al. 2022).

191 The Rubin Observatory system consists of four main
 192 components: the *Simonyi Survey Telescope*, featuring
 193 an 8.4 m diameter (6.5 m effective aperture) primary
 194 mirror that delivers a wide field of view; a 3.2-gigapixel
 195 camera, capable of imaging 9.6 square degrees per ex-
 196 posure⁷⁹ with seeing-limited quality in six broadband
 197 filters, *ugrizy* (320–1050 nm); an automated *Data Man-*
 198 *agement System* that processes and archives tens of ter-
 199 abytes of data per night, generating science-ready data
 200 products within minutes for a global community of sci-
 201 entists; and an *Education and Public Outreach (EPO)*

202 program that provides real-time data access, interactive
 203 tools, and educational content to engage the public. The
 204 integrated system’s étendue⁸⁰ of 319 m² deg², is over an
 205 order of magnitude larger than that of any previous op-
 206 tical observatory, enabling a fast, large-scale survey with
 207 exceptional depth in a fraction of the time compared to
 208 other observatories.

209 The observatory’s design is driven by four key science
 210 themes: probing dark energy and dark matter; taking
 211 an inventory of the solar system; exploring the tran-
 212 sient and variable optical sky; and mapping the Milky
 213 Way (Ž. Ivezić et al. 2019a). These themes inform the
 214 optimization of a range of system parameters, includ-
 215 ing image quality, photometric and astrometric accu-
 216 racy, the depth of a single visit and the co-added survey
 217 depth, the filter complement, the total number of visits
 218 per pointing as well as the distribution of visits on the
 219 sky, and total sky coverage. Additionally, they inform
 220 the design of the data processing and access systems.
 221 By optimizing the system parameters to support a wide
 222 range of scientific goals, we maximize the observatory’s
 223 scientific output across all areas, making Rubin a pow-
 224 erful discovery machine capable of addressing a broad
 225 range of astrophysical questions.

226 Throughout the duration of the *LSST*, Rubin Obser-
 227 vatory will issue a series of Data Releases, each repre-
 228 senting a complete reprocessing of all *LSST* data col-
 229 lected up to that point. Prior to the start of the *LSST*
 230 survey, commissioning activities will generate a signifi-
 231 cant volume of science-grade data. To make this early
 232 data available to the community, the Rubin Early Sci-
 233 ence Program (L. P. Guy et al. 2026) was established.

* Author is deceased

⁷⁹ We define an “exposure” as the process of exposing all detectors in the focal plane. It is synonymous with the term “visit” in *Data Preview 1 (DP1)*. By contrast, an “image” is the output of a single detector following an exposure.

⁸⁰ The product of the primary mirror area and the angular area of its field of view for a given set of observing conditions.

234 One key component of this program is a series of Data
 235 Previews; early versions of the [LSST Data Releases](#).
 236 These previews include preliminary data products derived
 237 from both simulated and commissioning data, which,
 238 together with early versions of the data access
 239 services, are intended to support high-impact early sci-
 240 ence, facilitate community readiness, and inform the de-
 241 velopment of Rubin’s operational capabilities ahead of
 242 the start of full survey operations. All data and services
 243 provided through the Rubin Early Science Program are
 244 offered on a shared-risk basis ⁸¹.

245 This paper describes Rubin’s second of three planned
 246 Data Previews: [DP1 \(NSF-DOE Vera C. Rubin Observa-](#)
 247 [tory 2025a\)](#). The first, [Data Preview 0 \(DP0\)](#), con-
 248 tained data products produced from the processing of
 249 simulated [LSST-like](#) data sets. These were released to-
 250 gether with a very early version of the Rubin [Science](#)
 251 [Platform \(M. Jurić et al. 2019\)](#), which provided the data
 252 access services. [DP0](#) was released in multiple phases;
 253 [DP0.1](#), [DP0.2](#), and [DP0.3](#), each building upon the pre-
 254 vious and incorporating new data and functionalities.
 255 [DP0.1](#) and [DP0.2](#) uses data from the [cosmoDC2](#) simula-
 256 tions ([LSST Dark Energy Science Collaboration \(LSST](#)
 257 [DESC\) et al. 2021\)](#) prepared by the Dark Energy Science
 258 Collaboration ([DESC](#)), whereas [DP0.3](#) is based on simu-
 259 lated datasets from the [Solar System Science Collabora-](#)
 260 [tion \(SSSC\)](#). Online documentation for [DP0](#) is available
 261 at <https://dp0.lsst.io>.

262 [DP1](#) contains data products derived from the repro-
 263 cessing of science-grade exposures acquired by the [Ru-](#)
 264 [bin Commissioning Camera \(LSSTComCam\)](#), in late
 265 2024. The third and final Data Preview, [Data Preview](#)
 266 [2 \(DP2\)](#), is planned to be based on a reprocessing of all
 267 science-grade data taken with the Rubin’s [LSST Science](#)
 268 [Camera \(LSSTCam\)](#) during commissioning.

269 All Rubin Data Releases and Previews are subject
 270 to a two-year proprietary period, with immediate ac-
 271 cess granted exclusively to LSST data rights holders ([R.](#)
 272 [Blum & the Rubin Operations Team 2020\)](#). Data rights
 273 holders⁸² After the two-year proprietary period, [DP1](#)
 274 will be made public. However, even once the data be-
 275 come public, access for non-data rights holders will not
 276 be provided through Rubin Data Access Centers in the
 277 US and Chile ([R. Blum & the Rubin Operations Team](#)

278 [2020\)](#). Alternative access mechanisms are still under
 279 discussion and have not yet been finalized.

280 In this paper, we describe the contents and valida-
 281 tion of Rubin [DP1](#), the first Data Preview to deliver
 282 data derived from observations conducted by the Vera
 283 C. Rubin Observatory, as well as the data-access mecha-
 284 nisms and community-support services that accompany
 285 it. [DP1](#) is based on the reprocessing of 1792 science-
 286 grade exposures acquired during the first on-sky com-
 287 missioning campaign, conducted over 48 nights between
 288 2024-10-24 and 2024-12-11. It covers a total area of
 289 approximately ~ 15 deg² distributed across seven dis-
 290 tinct non-contiguous fields. The data products include
 291 raw and calibrated single-epoch images, coadded images,
 292 difference images, detection catalogs, and other derived
 293 data products. [DP1](#) is about 3.5 TB in size and con-
 294 tains around 2.3 million distinct astronomical objects,
 295 detected in 2644 coadded images. Full [DP1](#) release doc-
 296 umentation is available at <https://dp1.lsst.io>. Despite
 297 Rubin Observatory still being in commissioning and not
 298 yet complete at the time the observations were acquired,
 299 Rubin [DP1](#) provides an important first look at the data,
 300 showcasing its characteristics and capabilities.

301 The structure of this paper is as follows. In section
 302 [2](#) we describe the observatory system and overall con-
 303 struction and commissioning status at the time of data
 304 acquisition, the seven fields included in [DP1](#), and the
 305 observing strategy used. Section [3](#) summarizes the con-
 306 tents of [DP1](#) and the data products contained in the
 307 release. The data processing pipelines are described in
 308 section [4](#), followed by a description of the data valida-
 309 tion and performance assessment in section [5](#). Section
 310 [6](#) describes the Rubin [Science Platform \(RSP\)](#), a cloud-
 311 based data science infrastructure that provides tools and
 312 services to Rubin data rights holders to access, visual-
 313 ize and analyze peta-scale data generated by the [LSST](#).
 314 Section [7](#) presents the Rubin Observatory’s model for
 315 community support, which emphasizes self-help via doc-
 316 umentation and tutorials, and employs an open platform
 317 for issue reporting that enables crowd-sourced solutions.
 318 Finally, a summary of the [DP1](#) release and information
 319 on expected future releases of data is given in section [8](#).
 320 The appendix contains a useful glossary of terms used
 321 throughout this paper.

322 All magnitudes quoted are in the AB system ([J. B.](#)
 323 [Oke & J. E. Gunn 1983\)](#), unless otherwise specified.

324 2. ON-SKY COMMISSIONING CAMPAIGN

325 The first Rubin on-sky commissioning campaign was
 326 conducted using the [LSSTComCam](#). The campaign’s
 327 primary objective was to optically align the Simonyi
 328 Survey Telescope and verify its ability to deliver accept-

⁸¹ Shared risk means early access with caveats: the community benefits from getting a head start on science, preparing analyses, and providing feedback, while also accepting that the system may not work as well as it will during full operations.

⁸² Individuals or institutions with formal authorization to access proprietary data collected by the Vera C. Rubin Observatory. See <https://www.lsst.org/scientists/international-drh-list>

able image quality using *LSSTComCam*. In addition, the campaign provided valuable operations experience to facilitate commissioning the full *LSSTCam* (T. Lange et al. 2024; A. Roodman et al. 2024). We note that commissioning *LSSTComCam* was not an objective of the campaign. Instead, *LSSTComCam* was used as a tool to support broader observatory commissioning, including early testing of the *Active Optics System* (AOS) and the *LSST Science Pipelines*. As a result, many artifacts present in the data are specific to *LSSTComCam* and will be addressed only if they persist with *LSSTCam*. Accordingly, the image quality achieved during this campaign, and in the *DP1* data, may not reflect the performance ultimately expected from *LSSTCam*.

Approximately 16,000 exposures⁸³ were collected during this campaign, the majority in support of AOS commissioning, system-level verification, and end-to-end testing of the telescope’s hardware and software. This included over 10000 exposures for AOS commissioning, more than 2000 bias and dark calibration frames, and over 2000 exposures dedicated to commissioning the *LSST Science Pipelines*. For *DP1*, we have selected a subset of 1792 science-grade exposures from this campaign that are most useful for the community to begin preparing for early science.

At the time of the campaign, the observatory was still under construction, with several key components, such as dome thermal control, full mirror control, and the final AOS configuration either incomplete or still undergoing commissioning. As a result, image quality varied widely throughout the campaign and exhibited a broader distribution than is expected with *LSSTCam*. Despite these limitations, the campaign successfully demonstrated system integration and established a functional observatory.

2.1. *Simonyi Survey Telescope*

The *Simonyi Survey Telescope* (B. Stalder et al. 2024) features a unique three-mirror design, including an 8.4-meter *Primary Mirror Tertiary Mirror* (M1M3) fabricated from a single substrate and a 3.5-meter *Secondary Mirror* (M2). This compact configuration supports a wide 3.5-degree field of view while enabling exceptional stability, allowing the telescope to slew and settle in under five seconds. To achieve the scientific goals of the 10-year *LSST*, the Observatory must maintain high image quality across its wide field of view (Ž. Ivezić et al.

2019b). This is accomplished through the AOS (B. Xin et al. 2015; G. Megias Homar et al. 2024), which corrects, between successive exposures, wavefront distortions caused by optical misalignments and mirror surface deformations, primarily due to the effect of gravitational and thermal loads.

The AOS, which comprises an open-loop component and a closed-loop component, optimizes image quality by aligning the camera and M2 relative to M1M3, as well as adjusting the shapes of all three mirrors to nanometer precision. The AOS open-loop component corrects for predictable distortions and misalignments, while the closed-loop component addresses unpredictable or slowly varying aberrations using feedback from the corner wavefront sensors. The closed-loop wavefront sensing technique is curvature wavefront sensing, which infers wavefront errors in the optical system by analyzing extra- and intra-focal star images (S. Thomas et al. 2023). Since *LSSTComCam* lacks dedicated wavefront sensors, wavefront errors were instead estimated by defocusing the telescope ± 1.5 mm on either side of focus and applying the curvature wavefront sensing pipeline to the resulting images. Each night began with an initial alignment correction using a laser tracker to position the system within the capture range of the closed-loop algorithm (G. Megias Homar et al. 2024). Once this coarse alignment was complete, the AOS refined the optical alignment and applied mirror surfaces corrections to optimize the image quality across the *LSSTComCam* field of view.

During *LSST Science Pipelines* commissioning (§2.4), observations were conducted using the AOS in open-loop mode only, without closed-loop corrections between exposures. Closed-loop operation, which requires additional intra- and extra-focal images with *LSSTComCam*, was not compatible with the continuous data acquisition needed by the pipelines. The image quality for these data was monitored by measuring the *Point Spread Function* (PSF) *Full Width at Half-Maximum* (FWHM), and closed-loop sequences were periodically run when image quality degradation was observed.

2.2. *The LSST Commissioning Camera*

LSSTComCam (B. Stalder et al. 2022, 2020; J. Howard et al. 2018; SLAC National Accelerator Laboratory & NSF-DOE Vera C. Rubin Observatory 2024) is a 144-megapixel version of the 3.2-gigapixel *LSSTCam*. It covers approximately 5% of the *LSSTCam* focal plane area, with a field of view of ~ 0.5 deg² ($40' \times 40'$), compared to *LSSTCam*’s 9.6 deg². It was developed to validate camera interfaces with other observatory components and evaluate overall system performance prior to

⁸³ We define an exposure as the process of exposing all *LSSTComCam* detectors. It is synonymous with visit in *DP1*. By contrast, an image is the output of a single *LSSTComCam* detector following an exposure.

the start of **LSSTCam** commissioning. Although **LSST-ComCam** has a smaller imaging area, it shares the same plate scale of $0''.2$ per pixel and is housed in a support structure that replicates the mass, center of gravity, and physical dimensions of **LSSTCam**. All mechanical and utility interfaces to the telescope are implemented identically, enabling full end-to-end testing of observatory systems, including readout electronics, image acquisition, and data pipelines. Although the **LSSTComCam** cryostat employs a different cooling system (Cryotels) to that of **LSSTCam**, it included a refrigeration pathfinder to validate the cryogenic system intended for **LSSTCam**.

The **LSSTCam** focal plane comprises 25 modular rafts arranged in a 5×5 grid, of which 21 are science rafts dedicated to imaging and 4 are corner rafts used for guiding and wavefront sensing. **LSSTCam** employs CCD sensors from two vendors: **Imaging Technology Laboratory, University of Arizona (UA)** (ITL) and **Teledyne (E2V)**. In contrast, **LSSTComCam** contains only a single science raft equipped exclusively with ITL sensors. **Figure 1** presents a schematic of the **LSSTCam** focal plane, with the **LSSTComCam** raft positioned at the center, corresponding to the **LSSTCam** central science raft location. The perspective is from above, looking down through the **LSSTComCam** lenses onto the focal plane.

Each science raft is a self-contained unit comprising nine $4K \times 4K$ **Charge-Coupled Device (CCD)** (G. E. Smith 2010) sensors arranged in a 3×3 mosaic, complete with integrated readout electronics and cooling systems. Each sensor is subdivided into 16 segments arranged in a 2×8 layout, with each segment consisting of 512×2048 pixels and read out in parallel using individual amplifiers. This design is identical across all science rafts. To maintain uniform performance and calibration, each raft is populated exclusively with sensors from a single vendor.

LSSTComCam consists of a single science raft, designated Raft 22 (R22), equipped solely with ITL sensors. These sensors were selected from the best-performing remaining ITL devices after the **LSSTCam** rafts were fully populated. Some exhibit known issues such as high readout noise (e.g., Detector 8) and elevated **Charge Transfer Inefficiency (CTI)** (e.g., Detector 5). Consequently, certain image artifacts present in the DP1 dataset may be specific to **LSSTComCam**. **Figure 2** shows the **LSST-ComCam** R22 focal plane layout and the placement and numbering scheme of sensors (S) and amplifiers (C). This configuration is identical across all science rafts in **LSSTCam**. The **LSSTCam** and **LSSTComCam** focal planes are described in detail in A. A. Plazas Malagón et al. (2025).

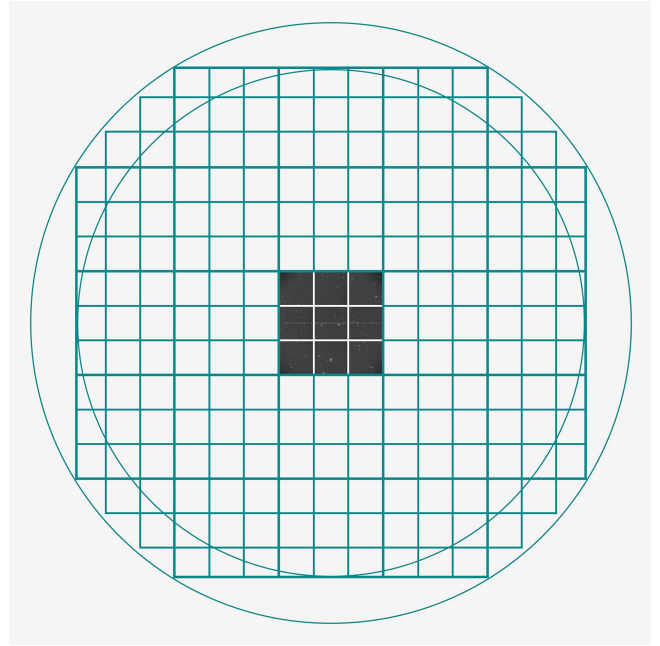


Figure 1. **LSSTComCam** focal plane layout illustrating the placement of its nine sensors, shown in gray, which form a raft. The view is looking down from above the focal plane through the **LSSTComCam** lenses. **LSSTComCam** is Raft 22 (R22). We also indicate the location of the **LSSTCam** sensors (open squares) to highlight the field-of-view of **LSST-ComCam** in relation to that of **LSSTCam**.

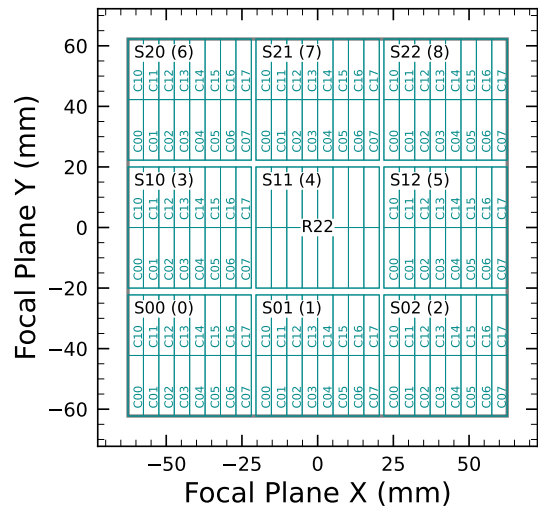


Figure 2. **LSSTComCam** focal plane layout, showing Raft 22 (R22) and the placement and numbering scheme of sensors (S) and amplifiers (C). The view is from above, looking through the **LSSTComCam** lenses onto the focal plane. Each sensor contains 16 amplifiers, and the raft is composed of a 3×3 array of sensors. The detector number for each sensor is indicated in parentheses.

2.2.1. Filter Complement

LSSTComCam supports imaging with six broadband filters *ugrizy* spanning 320–1050 nm, identical in design to LSSTCam. However, its filter exchanger can hold only three filters at a time, compared to five with LSSTCam. The full-system throughput of the six LSSTComCam filters, which encompasses contributions from a standard atmosphere at airmass 1.2, telescope optics, camera surfaces, and the mean ITL detector quantum efficiency is shown in Figure 3. The corresponding transmission curves are provided as a DP1 data product, see §3.6.1

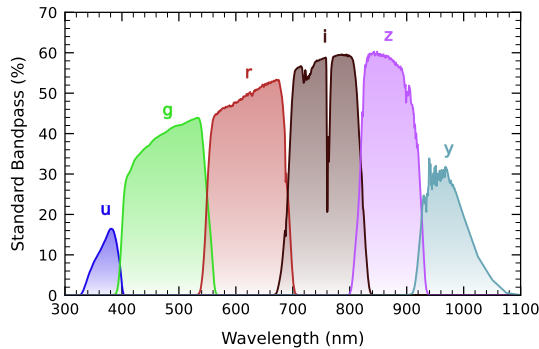


Figure 3. LSSTComCam standard bandpasses, illustrating full system throughput. The bandpasses include a standard atmosphere at airmass 1.2, telescope optics, camera surfaces, and mean ITL detector quantum efficiency. The corresponding transmission curves are provided as a DP1 data product.

2.2.2. Timing Calibration

The absolute time accuracy of data taken with LSSTComCam relies on the Network Time Protocol (NTP) for clock synchronization, which should be accurate to approximately 1 millisecond. In order to evaluate the absolute timing accuracy of the entire system we observed the geosynchronous satellite EUTELSAT 117 West B with a set of 10 usable 10-second exposures over two nights. EUTELSAT 117 West B is part the Global Positioning System (GPS) system and serves as one of the Wide Area Augmentation System (WAAS) satellites operated for the U.S. Federal Aviation Administration (FAA) and used to broadcast GPS corrections to air traffic.

As these satellites are part of the GPS system, their positions are tracked very precisely and the record of their locations is published after the fact and can be downloaded. Following the technique previously employed by other surveys, (J. L. Tonry et al. 2018), we observed the satellite while tracking the sky and then downloaded the data-files with its precise locations from

the National Satellite Test Bed web site⁸⁴. By comparing the measured and predicted locations of the start of the satellite track on the sky, we determined that (relative to the start of integration-time recorded in the Flexible Image Transport System (FITS) headers) our time was accurate to 53.6 ± 11.0 milliseconds.

This work continues to be an area of ongoing study, with the exact timing of when the shutter open command is issued, and the complete profile of the shutter movement not yet determined. However the open command is on average near 29 milliseconds later. Incorporating the delays into the fit reduces the offset to 24.8 ± 11.0 milliseconds.

The full shutter takes approximately 396 milliseconds to completely open. As the LSSTComCam sensors are centered in the aperture, the center of the focal plane should be exposed about half-way through the shutter open procedure, 198 milliseconds after the open command. There are uncertainties on the full motion profile, and the blade direction motions are currently not known, but the fraction of the shutter aperture subtended by the focal plane is 52%. This implies that that the shutter will pass any pixel between 198 ± 103 milliseconds. Subtracting this from the fitted delay of 24.8 milliseconds and adding the fitted error of 11.0 milliseconds in quadrature, results in a current conservative estimate of the delay of -173.2 ± 104.1 milliseconds, consistent with and smaller than the constraints on the timing offset determined using astrometric residuals from known asteroid associations presented in §5.9.2.

2.3. Flat Field System

During the on-sky campaign, key components of the Rubin calibration system (P. Ingraham et al. 2022), including the flat field screen, had not yet been installed. As a result, flat fielding for DP1 relied entirely on twilight flats. While twilight flats pose challenges such as non-uniform illumination and star print-through, they were the only available option during LSSTComCam commissioning and for DP1 processing. To mitigate these limitations, dithered, tracked exposures were taken over a broad range of azimuth and rotator angles to construct combined flat calibration frames. Exposure times were dynamically adjusted to reach target signal levels of between 10,000 and 20,000 electrons. Future campaigns with LSSTCam will benefit from more stable and uniform flat fielding using the Rubin flat field system, described in P. Fagrelius & E. S. Rykoff (2025).

⁸⁴ <https://www.nstb.tc.faa.gov/nstbarchive.html>

2.4. LSST Science Pipelines Commissioning

Commissioning of the LSST Science Pipelines, (Rubin Observatory Science Pipelines Developers 2025), began once the telescope was able to routinely deliver sub-arcsecond image quality. The goals included testing the internal astrometric and photometric calibration across a range of observing conditions, validating the difference image analysis and Prompt Processing (K.-T. Lim 2023) framework, and accumulating over 200 visits per band to evaluate deep coadded images with integrated exposure times roughly equivalent to those of the planned LSST Wide-Fast-Deep (WFD) 10-year depth. To support these goals, seven target fields were selected that span a range of stellar densities, overlap with external reference datasets, and collectively span the full breadth of the four primary LSST science themes. These seven fields form the basis of the DP1 dataset. Figure 4 shows the locations of these seven fields on the sky, overlaid on the LSST baseline survey footprint (R. L. Jones et al. 2021; P. Yoachim 2022; Rubin’s Survey Cadence Optimization Committee et al. 2022, 2023, 2025), along with sky coverage of both the LSSTCam and LSSTComCam focal planes. Each of the seven target fields was observed repeatedly in multiple bands over many nights. A typical observing epoch on a given target field consisted of 5-20 visits in each of the three loaded filters. Only images taken as 1x30 second exposures have been included in DP1. All images were acquired using the Rubin Feature-Based Scheduler (FBS), version 3.0 (E. Naghib et al. 2019; P. Yoachim et al. 2024). Table 1 lists the seven DP1 fields and their pointing centers, and provides a summary of the band coverage in each.

Figure 5 shows the temporal sampling of observations by filter and by night. The figure indicates the dates on which each field was observed in a given band but does not convey the total number of observations obtained per filter on any individual night. Gaps in coverage across some bands arise from the fact that LSSTComCam can only accommodate three filters at a time (see §2.2). As the campaign progressed, the temporal sampling became denser across all fields, reflecting improved efficiency and increased time allocated for science observations. The Extended Chandra Deep Field-South Survey (ECDFS) field received the most consistent and densest temporal sampling. It is important to note that the time sampling in the DP1 dataset differs significantly from what will be seen in the final LSST data. All fields except for the low ecliptic latitude field, Rubin_SV_38_7, used a small random dithering pattern. The random translational dithers of the telescope boresight were applied for each visit, with offsets of up to 0.2 degrees around the pointing center (Table 1). The

rotational dithers of the camera rotator were typically approximately 1 degree per visit, with larger random offsets at each filter change, which worked to keep operational efficiency high. The Rubin_SV_38_7 field used a different dither pattern to optimize coverage of Solar System Objects and test Solar System Object linking across multiple nights. These observations used a 2x2 grid of LSSTComCam pointings to cover an area of about 1.3 degreex1.3 degrees. The visits cycled between the grid’s four pointing centers, each separated by 0.65 degrees, and used small random translational dithers to fill chip gaps with the goal of acquiring 3-4 visits per pointing center per band in each observing epoch. The ra/dec vale giving in table 1 for this field is approximately the center of the 4 files.

Figure 6 shows sky coverage maps showing the distribution of visits in each of the seven DP1 fields, color coded by band. The images clearly show the focal plane chip gaps and dithering pattern. DP1 Only the detectors for which single frame processing succeeded are included in the plots, which explains why the central region of 47_Tuc looks thinner than the other fields (see §5.10). Table 2 reports the 5 σ point source depths for coadded images per field and per band, where coverage in a band is non-zero, together with the expected 10-year LSST depths derived from the baseline simulated survey (F. B. Bianco et al. 2022).

2.5. Delivered Image Quality

The delivered image quality is influenced by contributions from both the observing system (i.e., dome, telescope and camera) and the atmosphere. During the campaign, the Rubin Differential Image Motion Monitor (DIMM) was not operational, so atmospheric seeing was estimated using live data from the Southern Astrophysical Research Telescope (SOAR) Ring-Image Next Generation Scintillation Sensor (RINGSS) seeing monitor, also located on Cerro Pachón. Although accelerometers mounted on the mirror cell and top-end assembly were available to track dynamic optics effects, such as mirror oscillations that can degrade optical alignment, this data was not used during the campaign. Mount encoder data were used to measure the mount jitter in every image, with a measured median contribution of 0.004 arcseconds to image degradation. As the pointing model was not fine tuned, tracking errors could range from 0.2 to 0.4 arcseconds per image, depending on RA and Dec. Dome and mirror-induced seeing were not measured during the campaign.

The DP1 median delivered image quality, quantified as the PSF at FWHM across all filters and target fields, is 1".14. The best images achieve a PSF FWHM of ap

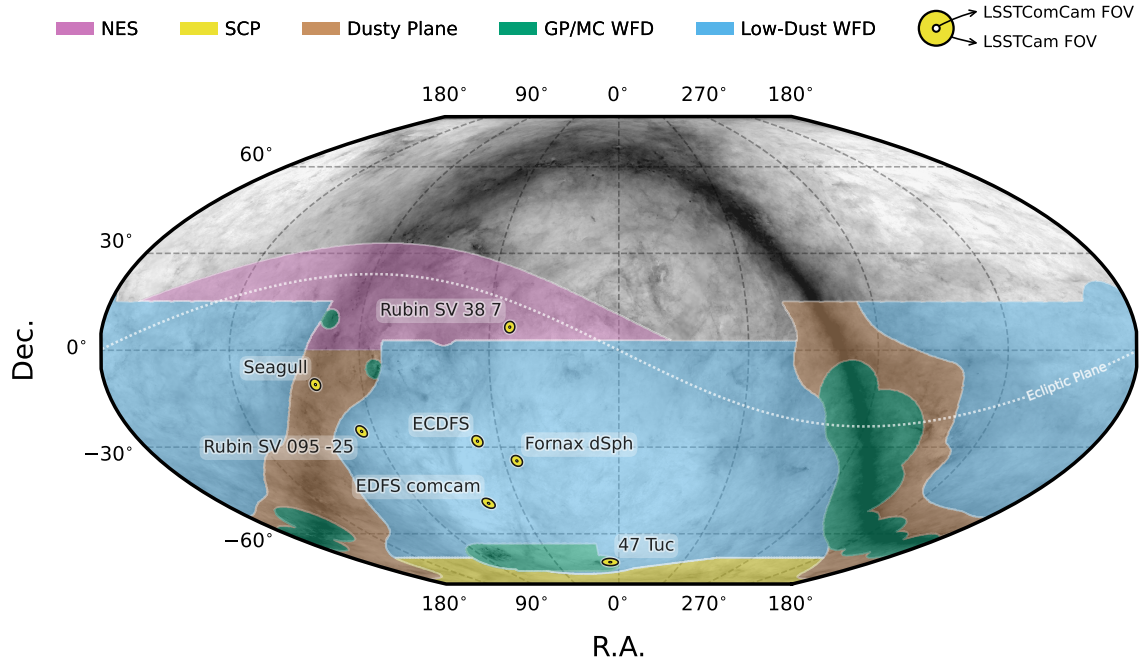


Figure 4. Locations of the seven DP1 fields overlaid on the LSST baseline survey footprint. NES: North Ecliptic Spur, SCP: South Celestial Pole, Low-Dust WFD: regions away from the Galactic Plane (GP) observed with a WFD cadence, GP/MC WFD: Galactic Plane and Magellanic Clouds regions observed with a WFD cadence. The field of view covered by the LSSTCam and LSSTComCam focal planes is shown as concentric yellow circles about the pointing center of each field.

Table 1. DP1 fields and pointing centers with the number of exposures in each band per field. ICRS coordinates are in units of decimal degrees, and are specified as J2000.

Field Code	Field Name	RA	DEC	Band						Total
				deg	deg	<i>u</i>	<i>g</i>	<i>r</i>	<i>i</i>	
47_Tuc	47 Tucanae Globular Cluster	6.128	-72.090	6	10	32	19	0	5	72
ECDFS	Extended Chandra Deep Field South	53.160	-28.100	43	230	237	162	153	30	855
EDFS_comcam	Rubin SV Euclid Deep Field South	59.150	-48.730	20	61	87	42	42	20	272
Fornax_dSph	Fornax Dwarf Spheroidal Galaxy	40.080	-34.450	0	5	25	12	0	0	42
Rubin_SV_095_-25	Rubin SV Low Galactic Latitude Field	95.040	-25.000	33	82	84	23	60	10	292
Rubin_SV_38_7	Rubin SV Low Ecliptic Latitude Field	37.980	7.015	0	44	40	55	20	0	159
Seagull	Seagull Nebula	106.300	-10.510	10	37	43	0	10	0	100
Total				112	469	548	313	285	65	1792

668 proximately $0''.58$. Both the per-sensor PSF FWHM and
 669 the overall median vary depending on the filter and the
 670 specific target field. The median delivered image quality
 671 per band and target field is provided in Table 3. Fig-
 672 ure 7 shows the distribution of PSF FWHM (in arcsec)
 673 over all 16071 individual sensors images. Ongoing efforts
 674 aim to quantify all sources of image degradation, includ-
 675 ing contributions from the camera system; static and
 676 dynamic optical components; telescope mount motion;
 677 observatory-induced seeing from the dome and primary

679 mirror; and atmospheric conditions. For the LSST, the
 680 design specification for the median delivered image qual-
 681 ity, referenced to the zenith and 550 nm, is $0''.7$. This
 682 value corresponds to the measured median atmospheric
 683 seeing at the Cerro Pachón site and a system contribu-
 684 tion to delivered image quality of $0''.35$ added in quadra-
 685 ture.

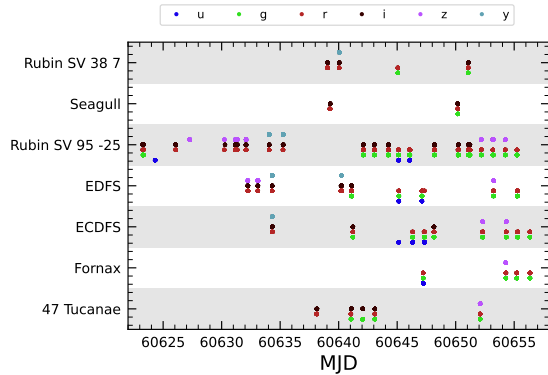


Figure 5. Temporal distribution of DP1 observations, grouped by field as a function of Modified Julian Date (MJD) and color-coded by filter. Each point indicates that a given field was observed at least once in the corresponding filter on that date.

Table 2. DP1 median 5σ coadded point-source detection limits per field and band, expressed in magnitudes, compared with the expected 10-year LSST values derived from the baseline simulated survey (F. B. Bianco et al. 2022).

Field Code	Band					
	<i>u</i>	<i>g</i>	<i>r</i>	<i>i</i>	<i>z</i>	<i>y</i>
47_Tuc	-	24.03	24.24	23.90	-	21.79
ECDFS	24.55	26.18	25.96	25.71	25.07	23.10
EDFS_comcam	23.42	25.77	25.72	25.17	24.47	23.14
Fornax_dSph	-	24.53	25.07	24.64	-	-
Rubin_SV_095_-25	24.29	25.46	24.95	24.86	24.32	22.68
Rubin_SV_38_7	-	25.46	25.15	24.86	23.52	-
Seagull	23.51	24.72	24.19	-	23.30	-
LSST 10-year	25.73	26.86	26.88	26.34	25.63	24.87

3. OVERVIEW OF THE CONTENTS OF RUBIN DP1

In this section we describe the Rubin DP1 data products and provide summary statistics for each. For more detailed information, we refer the reader to the DOI-registered DP1 release documentation available at <https://dp1.lsst.io> and the catalog schemas available at <https://sdm-schemas.lsst.io>.⁸⁵

The DP1 science data products are derived from the 15972 individual CCD images taken across 1792 expo-

Table 3. DP1 Median image quality per field and per band quantified as the PSF at FWHM in arcseconds.

Field Code	Band						All
	<i>u</i>	<i>g</i>	<i>r</i>	<i>i</i>	<i>z</i>	<i>y</i>	
47_Tuc	-	1.27	1.25	1.11	-	1.33	1.22
ECDFS	1.40	1.14	1.08	1.00	1.00	1.07	1.08
EDFS_comcam	1.88	1.25	1.20	1.10	1.18	0.99	1.19
Fornax_dSph	-	1.16	0.82	0.93	-	-	0.85
Rubin_SV_095_-25	1.40	1.25	1.14	0.97	1.17	0.82	1.19
Rubin_SV_38_7	-	1.13	1.13	1.10	1.22	-	1.13
Seagull	1.50	1.34	1.19	-	1.19	-	1.25
All	1.48	1.17	1.12	1.03	1.11	1.01	1.13

asures in the seven LSSTComCam commissioning fields (§2.4). To aid legibility, we have separated the descriptions of the data products from the description of the data release processing pipeline (§4). Similarly, as the DP1 data products can be accessed via one or both of International Virtual Observatory Alliance (IVOA) Services (§6.2.1) or the Data Butler (§6.2.2), we describe them here in a manner that is agnostic to the means of access.

The data products that comprise DP1 provide an early preview of future LSST data releases and are strongly dependent on the type and quality of the data that was collected during the LSSTComCam on-sky campaign (§2.4). Consequently not all anticipated LSST data products, as described in the Data Product Definition Document (DPDD) (M. Jurić et al. 2023), were produced for the DP1 dataset.

Rubin Observatory has adopted the convention by which single-epoch detections are referred to as “Sources”, and the astrophysical object associated with a given detection is referred to as an “Object”⁸⁶. As such, a given Object will likely have multiple associated Sources, since it will be observed in multiple epochs.

At the highest level, the DP1 data products fall into one of five types:

- **Science Images**, including single-epoch images, deep and template coadded images, and difference images (§3.1);
- **Catalogs** of astrophysical Sources and Objects detected and measured in the aforementioned im-

⁸⁵ Searchable catalog schemas are also available to Data Rights Holders via the Rubin Science Platform at <https://data.lsst.cloud>.

⁸⁶ We caution that this nomenclature is not universal; for example, some surveys use “detections” for what we call “sources”, and “sources” for what we call “objects”.

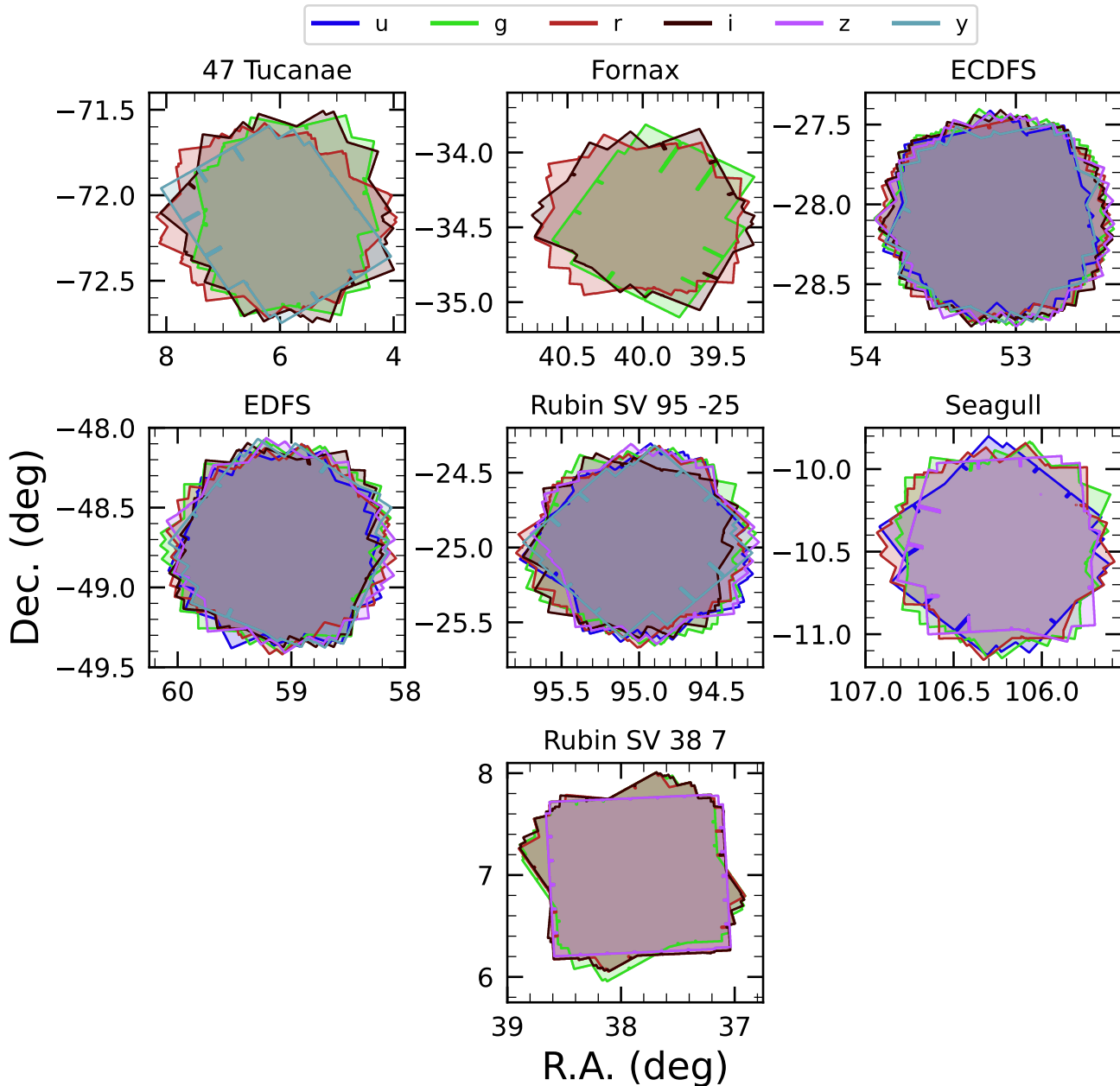


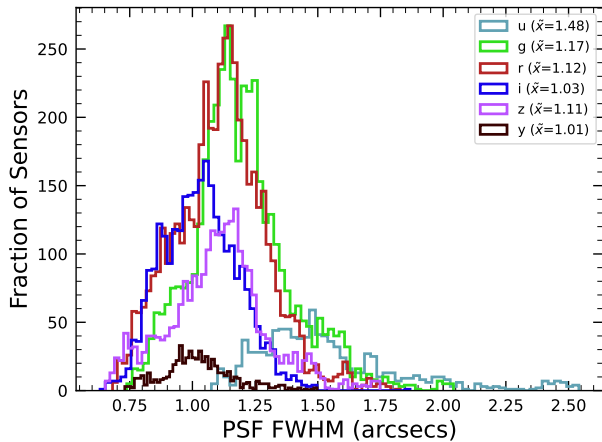
Figure 6. Sky coverage maps showing the distribution of visits in each field, color coded by band. The images clearly show the focal plane chip gaps and dithering pattern. Only the detectors for which single frame processing succeeded are included in the plots, which explains why the central region of 47_Tuc looks thinner than the other fields.

726 ages. We also provide the astrometric and photo- 734
 727 metric reference catalog generated from external 735
 728 sources that was used during processing to gener- 736
 729 ate the DP1 data products (§3.2); 737

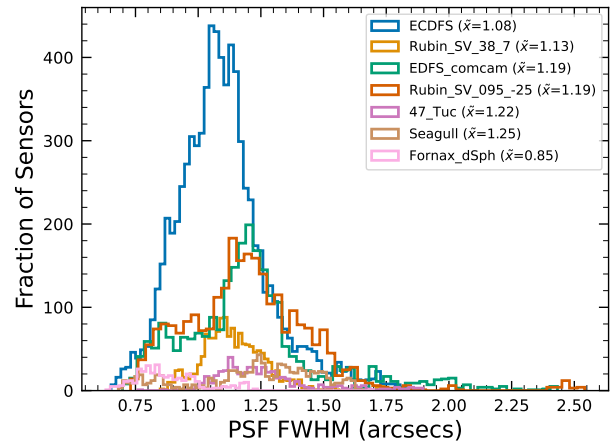
730 • **Maps**, which provide non-science-level visualiza- 738
 731 tions of the data within the release. They include, 739
 732 for example, zoomable multi-band images and cover- 740
 733 age maps (§3.4.1); 741

• **Ancillary data products**, including, for exam-
 ple, the parameters used to configure the data pro-
 cessing pipelines, log and processing performance
 files, and [calibration](#) data products (§3.6);

• **Metadata** in the form of tables containing infor-
 mation about each visit and processed image, such
 as pointing, exposure time, and a range of image
 quality summary statistics (§3.5).



(a) PSF FWHM (arcsecs) per passband across all DP1 target fields.



(b) PSF FWHM (arcsecs) per DP1 target field across all passbands

Figure 7. Histograms showing the distribution of delivered image quality for all 16071 single-epoch individual sensors in the DP1 dataset per passband (a) and per field (b). The median values are given in the legend.

While images and catalogs are expected to be the primary data products for scientific research, we also recognize the value of providing access to other data types to support investigations and ensure transparency.

To facilitate processing, Rubin DP1 uses a single skymap⁸⁷ that covers the entire sky area encompassing the seven DP1 fields. The DP1 skymap divides the entire celestial sphere into 18938 tracts, each covering approximately 2.8 deg^2 . The tracts are arranged in rings of declination, ordered from south to north, then with increasing right ascension within a ring. Each tract is further subdivided into 10×10 equally-sized patches. Both tracts and patches overlap with their neighboring regions. The amount of overlap between tracts changes with declination, with tracts nearest the poles having the greatest degree of overlap; the minimum overlap between tracts is $1/0$. By contrast, the amount of overlap between patches is constant, with each patch overlapping each of its neighbouring patches by 80% . Each patch covers 0.036 deg^2 which, due to the patch overlap, is slightly larger than the tract area divided by the number of patches in a tract. The aerial coverage of a patch is comparable to, but somewhat smaller than, the 0.058 deg^2 field-of-view of a single LSSTComCam or LSSTCam detector, meaning each detector image spans multiple patches. The size of a tract is larger than the LSSTComCam field of view. However, since each ob-

served field extends across more than one tract, each field covers multiple tracts.

The skymap is integral to the production of co-added images. To create a coadded image, the processing pipeline selects all calibrated science images in a given field that meet specific quality thresholds (§3.1 and §4.5.1) for a given patch, warps them onto a single consistent pixel grid for that patch, as defined by the skymap, then coadds them. Each individual coadd image therefore covers a single patch.

Throughout this section, the data product names are indicated using `monospace` font. Data products are accessed via either the IVOA Services (§6.2.1) or the Data Butler (§6.2.2).

3.1. Science Images

Science images are exposures of the night sky, as distinct from calibration images (§3.6.3). Although the release includes calibration images, thereby allowing users to reprocess the raw images if needed, this is expected to be necessary only in rare cases. Users are strongly encouraged to start from the `visit_image` provided. The data product names shown here are those used by the Data Butler, but the names used in the IVOA Services differ only slightly in that they are prepended by “`lsst.`”.

3.1.1. Raw Image

raw images (NSF-DOE Vera C. Rubin Observatory 2025b) are unprocessed data received directly from the camera. Each raw corresponds to a single CCD from a single LSSTComCam exposure of 30 s duration. Each LSSTComCam exposure typically produces up to nine raws, one per sensor in the focal plane. However, a

⁸⁷ A skymap is a tiling of the celestial sphere, organizing large-scale sky coverage into manageable sections for processing and analysis. While the skymap described here is specific to DP1, we do not anticipate major changes to the skymap in future data releases.

Table 4. Number of raw images per field and band. Each raw image corresponds to a single 30-second LSSTComCam exposure on one CCD. Most exposures produce nine raw images, one per sensor in the focal plane, however some yield fewer due to occasional hardware or readout issues.

Field Code	Band						Total
	<i>u</i>	<i>g</i>	<i>r</i>	<i>i</i>	<i>z</i>	<i>y</i>	
47_Tuc	54	90	288	171	0	45	648
ECDFS	387	2070	2133	1455	1377	270	7692
EDFS_comcam	180	549	783	378	378	180	2448
Fornax_dSph	0	45	225	108	0	0	378
Rubin_SV_095_-25	297	738	756	207	540	90	2628
Rubin_SV_38_7	0	396	360	495	180	0	1431
Seagull	90	333	387	0	90	0	900
Total	1008	4221	4932	2814	2565	585	16125

small number of exposures resulted in fewer than nine raw images due to temporary hardware issues or readout faults.

In total, DP1 includes 16125 raw images. Table 4 provides a summary by target and band. A raw contains 4608×4096 pixels, including prescan and overscan, and occupies around 18 MB of disk space.⁸⁸ The field of view of a single raw, excluding prescan and overscan regions, is roughly $0^\circ.23 \times 0^\circ.22 \approx 0.051 \text{ deg}^2$, corresponding to a plate scale of $0''.2$ per pixel.

3.1.2. Visit Image

visit_images (NSF-DOE Vera C. Rubin Observatory 2025c) are fully-calibrated processed images. They have undergone instrument signature removal (§4.2.1) and all the single frame processing steps described in §4.2 which are, in summary: PSF modeling, background subtraction, and astrometric and photometric calibration. As with raws, a visit_image contains processed data from a single CCD resulting from a single 30 s LSSTComCam exposure. As a consequence, a single LSSTComCam exposure typically results in nine visit_images. The handful of exposures with fewer than nine raw images also have fewer than nine visit_images, but there are an additional 153 raw images that failed processing and for which there is thus no corresponding visit_image. The majority of failures – 131 in total – were due to challenges with astrometric fits or PSF models

⁸⁸ Each amplifier image contains 3 and 64 columns of serial prescan and overscan pixels, respectively, and 48 rows of parallel overscan pixels, meaning a raw contains 4072×4000 exposed pixels.

in the 47_Tuc crowded field. The other failures were in the Rubin_SV_095_-25 (9 failures), ECDFS (8), Fornax_dSph (3), and EDFs_comcam (2) fields.

In total, there are 15972 visit_images in DP1. Each visit_image comprises three images: a calibrated science image, a variance image, and a pixel-level bit-mask that flags issues such as saturation, cosmic rays, or other artifacts. Each visit_image also contains a position-dependent PSF model, World Coordinate System (WCS) information, and various metadata providing information about the observation and processing. The science and variance images and the pixel mask each contain 4072×4000 pixels. In total, a single visit_image, including all extensions and metadata, occupies around 110 MB of disk space. A plot showing the normalized cumulative histogram of the 5σ depths of all the visit_images in DP1 is shown in Figure 8.

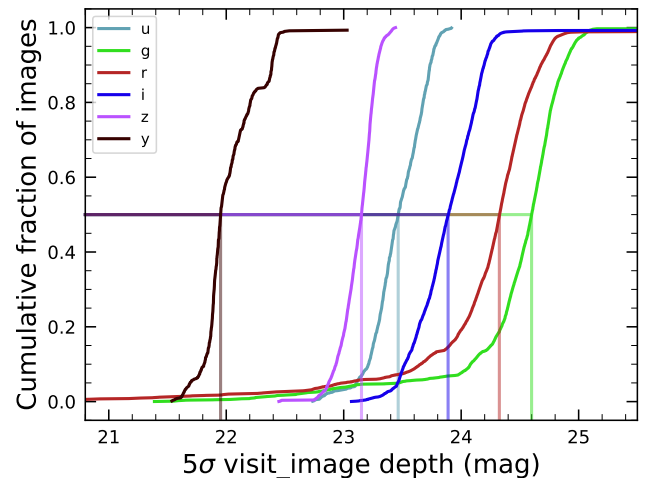


Figure 8. Normalized cumulative histograms of the 5σ depths of all visit_images in each band. The vertical lines indicate the 50th percentiles for each band (see legend).

3.1.3. Deep Coadd

deep_coadds are created on a per-band basis, meaning only data from exposures taken with a common filter are coadded. As such, there are up to six deep_coadds covering each patch – one for each of the six LSSTComCam bands. The process of producing deep_coadds is described in §4.5 but, to summarize, it involves the selection of suitable visit_images (both in terms of patch coverage, band, and image quality), the warping of those visit_images onto a common pixel grid, and the co-adding of the warped visit_images. To be included in a DP1 deep_coadd, a visit_image needed to have a PSF FWHM smaller than $1''.7$. Of the 15972 visit_

859 `images`, 15375 satisfied this criterion and were therefore
860 used to create `deep_coadds`.

861 There are a total of 2644 `deep_coadds` in DP1. As
862 mentioned above, a single `deep_coadd` covers one `patch`,
863 and includes a small amount of overlap with its neigh-
864 boring `patch`. The skymap used for DP1 defines a `patch`
865 as having an on-sky area of 0.028 deg² excluding overlap,
866 and 0.036 deg² including overlap. A single `deep_coadd`
867 – including overlap – contains 3400 × 3400 equal-sized
868 pixels, corresponding to a platescale of 0".2 per pixel.
869 Each `deep_coadd` contains the science image (i.e., the
870 coadd), a variance image, and a pixel mask; all three
871 contain the same number of pixels. Each `deep_coadd`
872 also contains a position-dependent PSF model (which
873 is the weighted sum of the PSF models of the input
874 `visit_images`), WCS information, plus various `meta-`
875 `data`.

876 The number of `visit_images` that contributed to a
877 given `deep_coadd` varies across the patch; the Survey
878 Property Maps can be consulted to gain insights into
879 the total exposure time at all locations covered by the
880 survey. Similarly, since coadds always cover an entire
881 `patch`, it is common for a `deep_coadd` to contain regions
882 that were not covered by any of the selected `visit_`
883 `images`, particularly if the `patch` is on the outskirts of
884 a field and was thus not fully observed. By the nature
885 of how coadds are produced, such regions may contain
886 seemingly valid `flux` values (i.e., not necessarily zeros or
887 NaNs), but will instead be flagged with the `NO_DATA` flag
888 in the pixel mask. It is therefore crucial that the pixel
889 mask be referred to when analyzing `deep_coadds`.

3.1.4. Template Coadd

890 `template_coadds` (NSF-DOE Vera C. Rubin Obser-
891 vatory 2025d) are those created to use as templates for
892 difference imaging, i.e., the process of subtracting a tem-
893 plate image from a `visit_image` to identify either vari-
894 able or `transient` objects. It should be noted, however,
895 that `template_coadds` are not themselves subtracted
896 from `visit_images` but are, instead, warped to match
897 the WCS of a `visit_image`. It is this warped template
898 that is subtracted from the `visit_image` to create a
899 difference image.⁸⁹ As with `deep_coadds`, `template_`
900 `coadds` are produced by warping and co-adding multiple
901 `visit_images` covering a given skymap-defined `patch`.
902 The process of building `template_coadds` is the same
903 as that for `deep_coadds`, but the selection criteria differ
904 between the two types of coadd. In the case of `tem-`
905

906 `plate_coadds`, one third of `visit_images` covering the
907 `patch` in question with the narrowest PSF FWHM are
908 selected. If one third corresponds to fewer than twelve
909 `visit_images` (i.e., there are fewer than 36 `visit_im-`
910 `ages` covering the `patch`), then the twelve `visit_images`
911 with the narrowest PSF FWHM are selected. Finally, if
912 there are fewer than twelve `visit_images` covering the
913 `patch`, then all `visit_images` are selected. Of the 15972
914 `visit_images`, 13113 were used to create `template_`
915 `coadds`. This selection strategy is designed to opti-
916 mize for `seeing` when a `patch` is well-covered by `visit_`
917 `images`, yet still enable the production of `template_`
918 `coadds` for poorly-covered patches. As with `deep_`
919 `coadds`, the number of `visit_images` that contributed
920 to a `template_coadd` varies across the patch.

921 DP1 contains a total of 2730 `template_coadds`.⁹⁰ As
922 with `deep_coadds`, a single `template_coadd` covers a
923 single `patch`. Since the same skymap is used when cre-
924 ating both `deep_coadd` and `template_coadds`, the on-
925 sky area and pixel count of `template_coadds` are the
926 same as that of a `deep_coadd` (see above). Similarly,
927 `template_coadds` contain the science image (i.e., the
928 coadd), a variance image, and a pixel mask; all three
929 contain the same number of pixels. Also included are
930 the PSF model, WCS information, and `metadata`. As
931 is the case for `deep_coadds`, those pixels within `tem-`
932 `plate_coadds` that are not covered by any of the se-
933 lected `visit_images` may still have seemingly valid val-
934 ues, but are indicated with the `NO_DATA` flag within the
935 pixel mask.

3.1.5. Difference Image

936 `difference_images` (NSF-DOE Vera C. Rubin Ob-
937 servatory 2025e) are generated by the subtraction of
938 the warped, scaled, and PSF-matched `template_coadd`
939 from the `visit_image` (see §4.6.1). In principle, only
940 those sources whose `flux` has changed relative to the
941 `template_coadd` should be apparent (at a significant
942 level) within a `difference_image`. In practice, how-
943 ever, there are numerous spurious sources present in
944 `difference_images` due to unavoidably imperfect tem-
945 plate matching.

946 In total, there are 15972 `difference_images` in DP1,
947 one for each `visit_image`.

948 Like `visit_images`, `difference_images` contain the
949 science (i.e., difference) image, a variance image, and a
950 pixel mask; all three contain the same number of pixels,
951 which is the same as that of the input `visit_image`.
952

⁸⁹ For storage space reasons, warped templates are not retained for DP1, as they can be readily and reliably recreated from the `template_coadds`.

⁹⁰ The difference in the number of `deep_coadds` and `template_coadds` is due to the difference in the `visit_image` selection criteria for each coadd.

Also included is the `PSF` model, `WCS` information, and `metadata`.

3.1.6. Background Images

Background images contain the model `background` that has been generated and removed from a science image. `visit_images`, `deep_coadds` and `template_coadds` all have associated `background` images.⁹¹ Background images contain the same number of pixels as their respective science image, and there is one `background` image for each `visit_image`, `deep_coadd`, and `template_coadd`. Difference imaging analysis also measures and subtracts a `background` model, but the `difference_background` data product is not written out by default and is not part of `DP1`.

Background images are not available via the `IVOA` Service; they can only be accessed via the `Butler` Data Service.

3.2. Catalogs

In this section we describe science-ready tables produced by the science pipelines. All catalogs contain data for detections in the images described in §3.1, except the `Calibration` catalog, which contains reference data obtained from previous surveys. Observatory-produced `metadata` tables are described in §3.5.

The catalogs contains measurements for either Sources detected in `visit_images` and `difference_images`, or Objects detected in `deep_coadds`. All catalogs store fluxes rather than magnitudes, with fluxes measured in nanojansky ($1 \text{ nJy} = 10^{-35} \text{ Wm}^{-2}\text{Hz}^{-1}$). Fluxes are preferred for multi-epoch observations, as they can be averaged across epochs, unlike magnitudes. Additionally, flux measurements on difference images (§3.1) are computed against a template, representing a flux difference. As a result, flux measurements on difference images can be negative, particularly for faint sources in the presence of noise.

The `Source`, `Object`, `ForcedSource`, `DiaSource`, `DiaObject`, and `ForcedSourceOnDiaObject` catalogs described below each vary in terms of their specific columns but generally contain: one or more unique identification numbers, positional information, multiple types of `flux` measurements (e.g., aperture fluxes, `PSF` fluxes, Gaussian fluxes, etc.), and a series of boolean flags indicating characteristics such as saturation or cosmic ray contamination for each source/object. The Solar System catalogs `SSObject` and `SSSource` deviate from

this general structure in that they instead contain orbital parameters for all known asteroids.

Where applicable, quantities are prefixed with the band in which they were measured, and all measured properties are reported with their associated 1σ uncertainties. For example, `g_ra` and `g_raErr` refer to right ascension and its uncertainty, measured in the g-band.

Fluxes for various apertures are provided together with an uncertainty and a flag, and named in the format `[band]_ap[size]Flux`, where `[size]` is the aperture diameter in pixels. For example, `g_ap03Flux`, `g_ap03FluxErr`, `g_ap03Flux_flag` provide the flux, uncertainty and flag measured within a 3.0-pixel aperture in the g-band. Similarly for flux measurements using difference algorithms, e.g. `g_psfFlux` provides the flux derived using the `PSF` model as a weight function, forced on g-band.

A complete list of columns with description and units for all tables in `DP1` is available at <https://sdm-schemas.lsst.io/dp1.html> Since `DP1` is a preview release, it does not include all the catalogs expected in a full `LSST Data Release`. Additionally, some catalogs may be missing columns, as not all quantities have been computed yet. These quantities will be included in future releases, and, where it is known to be the case, missing data are noted in the catalog descriptions that follow.

Catalog data are stored in the `Qserv` database (§6.5.1) and are accessible via `Table Access Protocol (IVOA standard) (IVOA)`, and an online `DP1` catalog schema is available at <https://sdm-schemas.lsst.io/dp1.html>. Catalog data are also accessible via the `Data Butler` (see §6.2.2).

3.2.1. Source Catalog

The `Source` catalog (`NSF-DOE Vera C. Rubin Observatory 2025f`) contains data on all sources which are, prior to deblending (§4.5.2), detected with a greater than 5σ significance in each individual visit. The detections reported in the `Source` catalog have undergone deblending; in the case of blended detections, only the deblended sources are included in the `Source` catalog. It is important to note that while the criterion for inclusion in a `Source` catalog is a $> 5\sigma$ detection in a `visit_image` prior to deblending, the positions and fluxes are reported post-deblending. Hence, it is possible for the `Source` catalog to contain sources whose `flux-to-error` ratios – potentially of all types (i.e., aperture `flux`, `PSF flux`, etc.) – are less than 5.

In addition to the general information mentioned above (i.e., IDs, positions, fluxes, flags), the `Source` catalog also includes basic `shape` and extendedness information.

⁹¹ In future data releases, `background` images may be included as part of their respective science image data product.

1050 The **Source** catalog contains data for 46 million
1051 **sources** in DP1.

1052 A cumulative histogram showing the PSF magnitudes
1053 of all **sources** contained within the **Source** catalogue is
1054 presented in the top panel of Figure 9

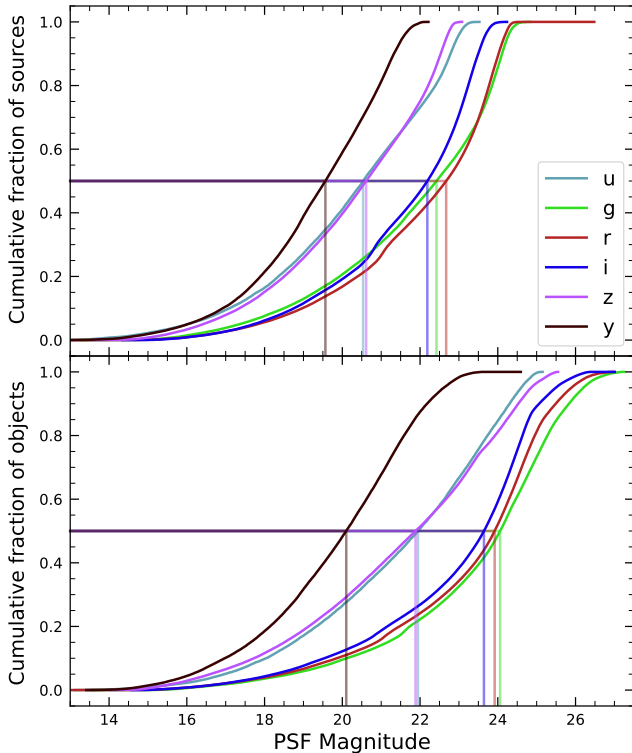


Figure 9. Normalized cumulative histograms of the PSF magnitudes of all $> 5\sigma$ -detected **sources** (top panel) and **objects** (bottom panel) contained in the **Source** and **Object** catalogs, respectively, separated according to band (see legend). The vertical lines indicate the 50th percentile for each band.

3.2.2. Object Catalog

1055
1056 The **Object** catalog (NSF-DOE Vera C. Rubin Ob-
1057 servatory 2025g) contains data on all objects detected
1058 with a greater than 5σ significance in the **deep_coadds**.
1059 With coadd images produced on a per-band basis, a
1060 $> 5\sigma$ detection in one or more of the bands will re-
1061 sult in an object being included in the **Object** catalog.
1062 For cases where an object is detected at $> 5\sigma$ in more
1063 than one band, a cross-matching has been performed
1064 between bands to associate an object in one band with
1065 its counterpart(s) in the other bands. As such, unlike
1066 the **Source** catalog, the **Object** catalog contains data
1067 from multiple bands. The objects reported in the **Ob-**
1068 **ject** catalog have also undergone deblending; in the case
1069 of blended detections, only the deblended child objects

1070 are included in the catalog. As with the **Source** cat-
1071 alog, the criterion for inclusion in the **Object** catalog
1072 is a $> 5\sigma$ detection in one of the **deep_coadds** prior to
1073 deblending, yet the positions and fluxes of objects are re-
1074 ported post-deblending. Hence, it is possible for **Object**
1075 catalog to contain **objects** whose **flux**-to-error ratios —
1076 potentially of all types and in all bands — are less than
1077 5.

1078 In addition to the general information mentioned
1079 above (i.e., IDs, positions, fluxes, flags), the **Object** cat-
1080 alog also includes basic **shape** and extendedness informa-
1081 tion. While they may be included in future data releases,
1082 no photometric redshifts, Petrosian magnitudes (V. Pet-
1083 rosian 1976), proper motions or periodicity information
1084 are included in the DP1 object catalogs.

1085 The **Object** catalog contains data for 2.3 million ob-
1086 jects in DP1.

3.2.3. ForcedSource Catalog

1087
1088 The **ForcedSource** catalog (NSF-DOE Vera C. Ru-
1089 bin Observatory 2025h) contains forced PSF photome-
1090 try measurements performed on both **difference_im-**
1091 **ages** (i.e., the **psfDiffFlux** column) and **visit_images**
1092 (i.e., the **psfFlux** column) at the positions of all the
1093 objects in the **Object** catalog, to allow assessment of
1094 the time variability of the fluxes. We recommend using
1095 the **psfDiffFlux** column when generating light curves
1096 because this quantity is less sensitive to **flux** from nei-
1097 ghoring sources than **psfFlux**. In addition to **forced pho-**
1098 **tometry PSF** fluxes, a number of boolean flags are also
1099 included in the **ForcedSource** catalog.

1100 The **ForcedSource** catalog contains a total of 269 mil-
1101 lion entries across 2.3 million unique objects.

3.2.4. DiaSource Catalog

1102
1103 The **DiaSource** catalogs (NSF-DOE Vera C. Rubin
1104 Observatory 2025i) contains data on all the sources de-
1105 tected at $> 5\sigma$ significance — including those associ-
1106 ated with known Solar System objects — in the **dif-**
1107 **ference_images**. Unlike sources detected in **visit_im-**
1108 **ages**, sources detected in difference images (hereafter,
1109 “**DiaSource**”) have gone through an association step in
1110 which an attempt has been made to associate them into
1111 underlying objects called “**DiaObject**”. The **DiaSource**
1112 catalog consolidates all this information across multiple
1113 visits and bands. The detections reported in the **Dia-**
1114 **Source** catalog have not undergone deblending.

1115 The **DiaSource** catalog contains data for 3.1 million
1116 **DiaSources** in DP1.

3.2.5. DiaObject Catalog

1117
1118 The **DiaObject** catalog (NSF-DOE Vera C. Rubin
1119 Observatory 2025j) contains the astrophysical objects

that `DiaSources` are associated with (i.e., the `DiaObjects`). The `DiaObject` catalog contains only non-Solar System Objects; Solar System Objects are, instead, recorded in the `SSObject` catalog. When a `DiaSource` is identified, the `DiaObject` and `SSObject` catalogs are searched for objects to associate it with. If no association is found, a new `DiaObject` is created and the `DiaSource` is associated to it. Along similar lines, an attempt has been made to associate `DiaObjects` across multiple bands, meaning the `DiaObject` catalog, like the `Object` catalog, contains data from multiple bands. Since `DiaObjects` are typically [transient](#) or variable (by the nature of their means of detection), the `DiaObject` catalog contains summary statistics of their fluxes, such as the mean and standard deviation over multiple epochs; users must refer to the `ForcedSourceOnDiaObject` catalog (see below) or the `DiaSource` catalog for single [epoch flux](#) measurements of `DiaObjects`.

The `DIAObject` catalog contains data for 1.1 million `DiaObjects` in [DP1](#).

3.2.6. *ForcedSourceOnDiaObject Catalog*

The `ForcedSourceOnDiaObject` catalog ([NSF-DOE Vera C. Rubin Observatory 2025k](#)) is equivalent to the `ForcedSource` catalog, but contains [forced photometry](#) measurements obtained at the positions of all the `DiaObjects` in the `DiaObject` catalog.

The `ForcedSourceOnDiaObject` catalog contains a total of 197 million entries across 1.1 million unique `DiaObjects`.

3.3. *SSObject Catalog*

The `SSObject` catalog ([NSF-DOE Vera C. Rubin Observatory 2025l](#)) and the [Minor Planet Center Orbit database \(MPCORB\)](#) carry information about solar system objects. The `MPCORB` table provides the [Minor Planet Center](#)-computed orbital elements for all known asteroids, including those that Rubin discovered. For [DP1](#), the `SSObject` catalog serves primarily to provide the mapping between the [International Astronomical Union \(IAU\)](#) designation of an object (listed in `MPCORB`), and the internal `ssObjectId` identifier, which is used as a key to find solar system object observations in the `DiaSource` and `SSSource` tables. The `SSObject` catalog contains data for 431 `SSObjects` in [DP1](#).

3.3.1. *SSSource Catalog*

The `SSSource` catalog ([NSF-DOE Vera C. Rubin Observatory 2025m](#)) contains data on all `DiaSources` that are either associated with previously-known Solar System Objects, or have been confirmed as newly-discovered Solar System Objects by confirmation of their

orbital properties. As entries in the `SSSource` catalog stem from the `DiaSource` catalog, they have all been detected at $> 5\sigma$ significance in at least one band. The `SSSource` catalog contains data for 5988 Solar System Sources.

3.3.2. *CcdVisit Catalog*

The `CcdVisit` catalog ([NSF-DOE Vera C. Rubin Observatory 2025n](#)) contains data for each individual processed `visit_image`. In addition to technical information, such as the on-sky coordinates of the central pixel and measured pixel scale, the `CcdVisit` catalog contains a range of data quality measurements, such as whole-image summary statistics for the [PSF](#) size, zeropoint, sky [background](#), sky noise, and quality of astrometric solution. It provides an efficient method to access `visit_image` properties without needing to access the image data. When combined with the data contained in the `Visit` table described in [§3.5](#), it provides a full picture of the telescope pointing and sky conditions at the time of observation.

The `CcdVisit` catalog contains entries summarizing data for all 16071 `visit_images`.

3.3.3. *Calibration Catalog*

The `Calibration` catalog is the reference catalog that was used to perform astrometric and photometric [calibration](#). It is a whole-sky catalog built specifically for [LSST](#), as no single prior reference catalog had both the depth and coverage needed to calibrate [LSST](#) data. It combines data from multiple previous reference catalogs and contains only stellar sources. Full details on how the `Calibration` catalog was built are provided in [P. S. Ferguson et al. \(2025\)](#)⁹². We provide a brief summary here.

For the *grizy* bands, the input catalogs were (in order of decreasing priority): [Dark Energy Survey \(DES\) Y6 Calibration Stars \(E. S. Rykoff et al. 2023\)](#); [Gaia-B or R Photometry \(Gaia\) \(XP\) Synthetic Magnitudes \(Gaia Collaboration et al. 2023a\)](#); the [Panoramic Survey Telescope and Rapid Response System \(Pan-STARRS\)1 3PI Survey \(K. C. Chambers et al. 2016\)](#); [Data Release 2 of the SkyMapper survey \(C. A. Onken et al. 2019\)](#); and [Data Release 4 of the VLT Survey Telescope \(VST\) Asteroid Terrestrial-impact Last Alert System \(ATLAS\) survey \(T. Shanks et al. 2015\)](#). For the *u*-band, the input catalogs were (in order of decreasing priority): [Standard Stars from Sloan Digital Sky Survey \(SDSS\) Data Release 16 \(R. Ahumada et al. 2020\)](#); [Gaia-XP Synthetic](#)

⁹² In [P. S. Ferguson et al. \(2025\)](#), the calibration reference catalog is referred to as “The Monster”. This terminology is also carried over to the [DP1 Butler](#).

Magnitudes (Gaia Collaboration et al. 2023a); and synthetic magnitudes generated using *Single Lens Reflex (SLR)*, which estimates the u -band flux from the g -band flux and $g-r$ colors. This SLR estimates were used to boost the number of u -band reference sources, as otherwise the source density from the u -band input catalogs is too low to be useful for the LSST.

Only stellar sources were selected from each input catalog. Throughout, the *Calibration* catalog uses the DES bandpasses for the *grizy* bands and the SDSS bandpass for the u -band; color transformations derived from high quality sources were used to convert fluxes from the various input catalogs (some of which did not use the DES/SDSS bandpasses) to the respective bandpasses. All sources from the input catalogs are matched to *Gaia-Data Release 3 (DR3)* sources for robust astrometric information, selecting only isolated sources (i.e., no neighbors within $1''$).

After collating the input catalogs and transforming the fluxes to the standard DES/SDSS bandpasses, the catalog was used to identify sources within a specific region of the sky. This process generated a set of standard columns containing positional and flux information, along with their associated uncertainties.

3.3.4. Source and Object Designations

To refer to individual sources or objects from the DP1 catalogs, one should follow the LSST DP1 naming convention that has been registered with the International Astronomical Union. Because the *Source*, *Object*, *DiaSource*, *DiaObject*, and *SSObject* tables each have their own unique IDs, their designations should differ. In general, source and object designations should begin with the string “LSST-DP1” (denoting the Legacy Survey of Space and Time, Data Preview 1), followed by a string specifying the table from which the source was obtained. These strings should be “O” (for the *Object* table), “S” (*Source*), “DO” (*DiaObject*), “DS” (*DiaSource*), or “SSO” (*SSObject*). Following the table identifier, the designation should contain the full unique numeric identifier from the specified table (i.e., the *objectId*, *sourceId*, *diaObjectId*, *diaSourceId*, or *ssObjectId*). Each component of the identifier should be separated by dashes, resulting in a designation such as “LSST-DP1-TAB-123456789012345678”. In summary, source designations should adhere to the formats listed below:

- Object: LSST-DP1-O-609788942606161356 (for *objectId* 609788942606161356)
- Source: LSST-DP1-S-600408134082103129 (for *sourceId* 600408134082103129)

- *DiaObject*: LSST-DP1-DO-609788942606140532 (for *diaObjectId* 609788942606140532)
- *DiaSource*: LSST-DP1-DS-600359758253260853 (for *diaSourceId* 600359758253260853)
- *SSObject*: LSST-DP1-SSO-21163611375481943 (for *ssObjectId* 21163611375481943)

Tables that were not explicitly mentioned in the description above do not have their own unique IDs, but are instead linked to one of the five tables listed above via a unique ID. For example, the *ForcedSource* table uses *objectId*, *ForcedSourceOnDiaObject* uses *diaObjectId*, *SSSource* uses *diaSourceId* and *ssObjectId*, and *MPCORB* uses *ssObjectId*.

3.4. Maps

Maps are two-dimensional visualizations of survey data. In DP1, these fall into two categories: Survey Property Maps and Hierarchical Progressive Survey (HiPS) Maps (P. Fernique et al. 2015).

3.4.1. Survey Property Maps

Survey Property Maps (NSF-DOE Vera C. Rubin Observatory 2025o) summarize how properties such as observing conditions or exposure time vary across the observed sky. Each map provides the spatial distribution of a specific quantity at a defined sky position for each band by aggregating information from the images used to make the *deep_coadd*. Maps are initially created per *tract* and then combined to produce a final consolidated map. At each sky location, represented by a spatial pixel in the Hierarchical Equal-Area iso-Latitude Pixelisation (HEALPix)(K. M. Górski et al. 2005) grid, values are derived using statistical operations, such as minimum, maximum, mean, weighted mean, or sum, depending on the property.

DP1 contains 14 survey property maps. The available maps describe total exposure times, observation epochs (one each for the earliest, mean, and latest observation epoch), PSF size and shape (one for each of the e^1 and e^2 shape parameters; see §5.2), PSF magnitude limits, sky background and noise levels, as well as astrometric shifts (one each for right ascension and declination) and PSF distortions (one for each of the e^1 and e^2 shape parameters) due to wavelength-dependent atmospheric Differential Chromatic Refraction (DCR) effects. They all use the dataset type format *deep_coadd_<PROPERTY>_consolidated_map_<STATISTIC>*. For example, *deep_coadd_exposure_time_consolidated_map_sum* provides a spatial map of the total exposure time accumulated per sky position in

units of seconds. All maps are stored in `HealSparse`⁹³ format. Survey property maps are only available via the `Data Butler` (§6.2.2).

Figure 10 presents three survey property maps for exposure time, PSF magnitude limit, and sky noise, computed for representative tracts and bands. Because full consolidated maps cover widely separated tracts, we use clipped per-tract views here to make the spatial patterns more discernible.

3.4.2. HiPS Maps

HiPS Maps (P. Fernique et al. 2015), offer an interactive way to explore seamless, multi-band tiles of the sky regions covered by DP1, allowing for smooth panning and zooming. DP1 provides multi-band HiPS images created by combining data from individual bands of `deep_coadd` and `template_coadd` images, using an improved version (Lust et al. in prep) of the algorithm presented in R. Lupton et al. (2004). These images are false-color representations generated using various filter combinations for the red, green, and blue channels.

The available filter combinations include `gri`, `izy`, `riz`, and `ugr` for both `deep_coadd` and `template_coadd`. Additionally, for `deep_coadd` only, we provide color blends such as `uug` and `grz`. Post-DP1, we plan to also provide single-band HiPS images for all `ugrizy` bands in both `Portable Network Graphics` (PNG) and `FITS` formats.

HiPS maps are only accessible through the HiPS viewer in the `Rubin Science Platform` (RSP) Portal (§6.3) and cannot be accessed via the `Data Butler` (§6.2.2). All multi-band HiPS images are provided in PNG format.

3.5. Metadata

DP1 also includes `metadata` about the observations, which are stored in the `Visit` table. We distinguish it from a catalog as the data it contains was produced by the observatory directly, rather than the science pipelines. The `Visit` table contains technical data for each visit, such as telescope pointing, camera rotation, `airmass`, exposure start and end time, and total exposure time. Some of the information contained within the `Visit` table is also contained in the `CCDVisit` catalogue described in §3.2 (e.g., exposure time), although the latter also includes information produced by the processing pipelines at a per-detector level, such as the PSF size and limiting magnitudes of a given `visit_image`.

⁹³ A sparse `HEALPix` representation that efficiently encodes data values on the celestial sphere. <https://healsparse.readthedocs.io>

3.6. Ancillary Data Products

DP1 also includes several ancillary data products. While we do not expect most users to need these, we describe them here for completeness. All the Data Products described in this section can only be accessed via the `Data Butler` (§6.2.2).

3.6.1. Standard Bandpasses

Figure 3 shows the full-system throughput of the six `LSSTComCam` filters. The corresponding transmission curves are provided as a DP1 data product. These datasets tabulate the full-system transmission of the six `LSSTComCam` filters as a function of wavelength and were used as a reference for the `LSSTComCam` DP1 photometry. The `standard_passband` dataset is keyed by band and is stored in `Astropy Table` format.

3.6.2. Task configuration, log, and metadata

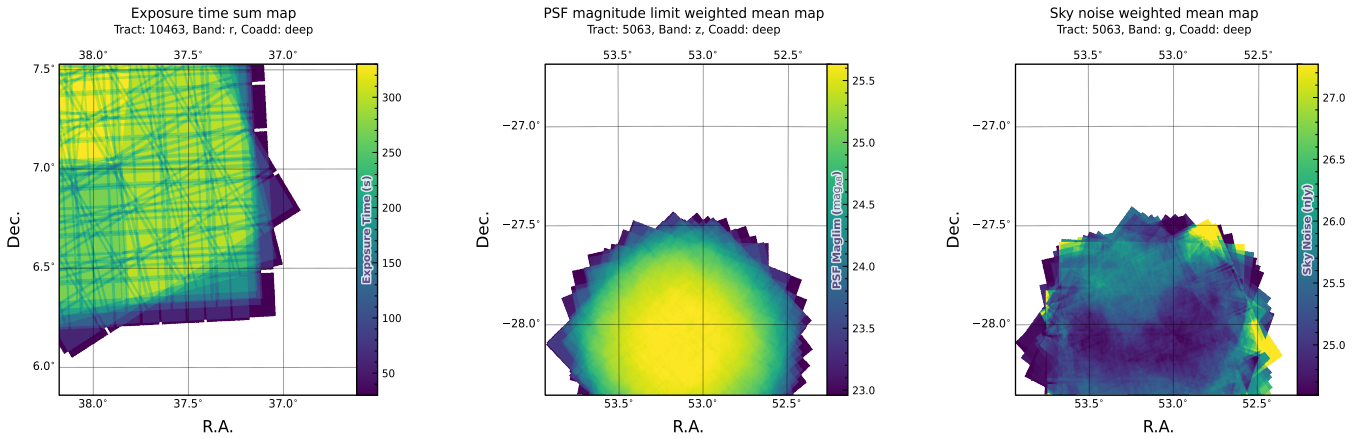
DP1 includes `provenance`-related data products such as task logs, `configuration` files, and task metadata. Configuration files record the parameters used in each processing task, while logs and `metadata` contain information output during processing. These products help users understand the processing setup and investigate potential processing failures.

3.6.3. Calibration Data Products

Calibration data products include a variety of images and models that are used to characterize and correct the performance of the camera and other system components. These include bias, dark, and flat-field images, `Photon Transfer Curve` (PTC) gains, brighter-fatter kernels (P. Antilogus et al. 2014), charge transfer inefficiency (CTI) models, linearizers, and illumination corrections. For flat-field corrections, DP1 processing used combined flats, which are averaged from multiple individual flat-field exposures to provide a stable `calibration`. These `calibration` products are essential inputs to `Instrument Signal Removal` (ISR) (§4.2.1). While these products are included in DP1 for transparency and completeness, users should not need to rerun ISR for their science and are advised to start with the processed `visit_image`.

4. DATA RELEASE PROCESSING

`Data Release Processing` (DRP) is the systematic processing of all Rubin Observatory data collected up to a certain date to produce the calibrated images, catalogs of detections, and derived data products described in Section 3. DP1 was processed entirely at the `United`



(a) Exposure time sum map for `deep_coadd tract 10463`, `r`-band in field `Rubin_SV_38_7` (b) 5σ PSF magnitude limit weighted mean map for `deep_coadd tract 5063`, `z`-band in field `ECDFS` (c) Sky noise weighted mean map for `deep_coadd tract 5063`, `g`-band in field `ECDFS`

Figure 10. Examples of survey property maps from Rubin DP1 across different bands, clipped to the boundary of a single tract for visual clarity.

1407 States Data Facility (USDF) at SLAC using 17,024 CPU 1432
 1408 hours.⁹⁴ 1433

1409 This section describes the pipeline algorithms used to 1434
 1410 produce DP1 and how they differ from those planned for 1435
 1411 full-scale LSST data releases. Data Release Production 1436
 1412 consists of four major stages: (1) single-frame processing, 1437
 1413 (2) calibration, (3) coaddition, and (4) difference 1438
 1414 image analysis (DIA). 1439

1415 4.1. LSST Science Pipelines Software

1416 The LSST Science Pipelines software (Rubin Observa- 1442
 1417 tory Science Pipelines Developers 2025; J. D. Swinbank 1443
 1418 et al. 2020) will be used to generate all Rubin Observa- 1444
 1419 tory and LSST data products. It provides both the algo- 1445
 1420 rithms and middleware frameworks necessary to process 1446
 1421 raw data into science-ready products, enabling analysis 1447
 1422 by the Rubin scientific community. Version v29.1 of the 1448
 1423 pipelines was used to produce DP1⁹⁵. 1449

1424 4.2. Single Frame Processing

1425 4.2.1. Instrument Signature Removal

1426 The first step in processing LSSTComCam images is 1453
 1427 to correct for the effects introduced by the telescope and 1454
 1428 detector. Each sensor and its readout amplifiers can 1455
 1429 vary slightly in performance, causing images of even a 1456
 1430 uniformly illuminated focal plane to exhibit discontinu- 1457
 1431 ities and shifts due to detector effects. The ISR pipeline 1458

1432 aims to recover the original astrophysical signal as best 1433
 1434 as possible and produce science-ready single-epoch im- 1435
 1436 ages for source detection and measurement. A detailed 1437
 1438 description of the ISR procedures can be found in P. Fa- 1439
 1440 greglius & E. S. Rykoff (2025) and A. A. Plazas Malagón 1440
 1441 et al. (2025). Figure 11 illustrates the model of detector 1441
 1442 components and readout electronics and their impact 1442
 1443 on the signal, tracing the process from photons incident 1443
 1444 on the detector surface to the final quantized values⁹⁶ 1444
 1445 recorded in the image files. The ISR pipeline essentially 1445
 1446 “works backward” through the signal chain, correct- 1446
 1447 ing the integer analog-to-digital units (ADU) raw 1447
 1448 camera output back to a floating-point number of pho- 1448
 1449 toelectrons created in the silicon. The physical detec- 1449
 1450 tor, represented on the left in Figure 11, is the source 1450
 1451 of effects that arise from the silicon itself, such as the 1451
 1452 dark current and the brighter-fatter effect (A. A. Plazas 1452
 1453 et al. 2018; A. Broughton et al. 2024). After the inte- 1453
 1454 gration time has elapsed, the charge is shifted to the 1454
 1455 serial register and read out, which can introduce charge 1455
 1456 transfer inefficiencies and a clock-injected offset level. 1456
 1457 The signals for all amplifiers are transferred via cables 1457
 1458 to the Readout Electronics Board (REB), during which 1458
 1459 crosstalk between the amplifiers may occur. The Ana- 1459
 1460 log Signal Processing Integrated Circuit (ASPIC) on the 1460
 1461 REB converts the analog signal from the detector into a 1461
 1462 digital signal, adding both quantization and a bias level 1462
 1463 to the image. Although the signal chain is designed to 1463
 1464 be stable and linear, the presence of numerous sources 1464
 1465 of non-linearity indicates otherwise. 1465

⁹⁴ For future Data Releases, data processing will be distributed across the USDF, the French (FrDF) and UK (UKDF) data facilities.

⁹⁵ Documentation for this version is available at: https://pipelines.lsst.io/v/v29_1_1

⁹⁶ The images written to disk by the camera have values that are integers that come from the ADC converting an analog voltage.

The *ISR* processing pipeline for *DP1* performs, in the following order: **Analogue-to-Digital Unit (ADU)** dithering to reduce quantization effects, serial overscan subtraction, saturation masking, gain normalization, crosstalk correction, parallel overscan subtraction, linearity correction, serial **CTI** correction, image assembly, bias subtraction, dark subtraction, brighter-fatter correction, defect masking and interpolation, variance plane construction, flat fielding, and amplifier offset (amp-offset) correction⁹⁷. Flat fielding for *DP1* was performed using combined flats produced from twilight flats acquired with sufficient rotational dithering to mitigate artifacts from print-through stars, as described in §2.3.

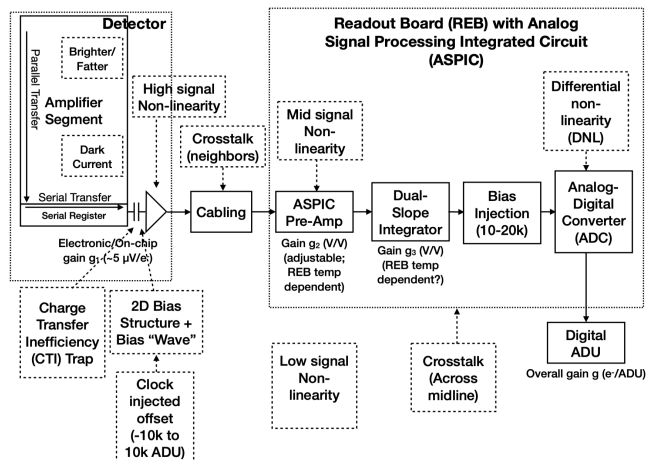


Figure 11. The model of the detector and REB components, labeled with the effects that they impart on signal.

4.2.2. Background Subtraction

The background subtraction algorithms in the LSST Science Pipelines estimate and remove large-scale background signals from science imaging. Such signals may include sky brightness from airglow, moonlight, scattered light instrumental effects, zodiacal light, and diffuse astrophysical emission. In so doing, true astrophysical sources are isolated to allow for accurate detection and measurement.

To generate a **background** model, each post-*ISR* image is divided into superpixels of 128×128 pixels. Pixels with a mask flag set that indicates that they contain no useful science data or that they contain **flux** from a preliminary source detection are masked. The iterative

⁹⁷ Amp-offset corrections are designed to address systematic discontinuities in background sky levels across amplifier boundaries. The implementation in the LSST Science Pipelines is based on the **Pan-STARRS** Pattern Continuity algorithm (C. Z. Waters et al. 2020).

3σ clipped mean of the remaining pixels is calculated for each superpixel, constructing a **background** statistics image. A sixth-order Chebyshev polynomial is fit to these values on the scale of a single detector to allow for an extrapolation back to the native pixel resolution of the post-*ISR* image.

4.3. Calibration

Stars are detected in each post-*ISR* image using a 5σ threshold. Detections of the same star across multiple images are then associated to identify a consistent set of isolated stars with repeated observations suitable for use in PSF modeling, photometric **calibration**, and astrometric **calibration**.

Initial astrometric and photometric solutions are derived using only the calibration reference catalogs (see §3.2), and an initial PSF model is fit using PSFEx (E. Bertin 2011). These preliminary solutions provide approximate source positions, fluxes, and PSF shapes that serve as essential inputs to the **calibration** process, enabling reliable source matching, selection of high-quality stars, and iterative refinement of the final astrometric, photometric, and PSF models. These preliminary solutions are subsequently replaced by more accurate fits, as described in the following sections.

4.3.1. PSF Modeling

PSF modeling in *DP1* uses the Piff (M. Jarvis et al. 2021) package. Our configuration of Piff utilizes its **PixelGrid** model with a fourth-order polynomial interpolation per **CCD**, except in the *u*-band, where star counts are insufficient to support a fourth-order fit. In this case, a second-order polynomial is used instead. Details on the choice of polynomial order, overall PSF modeling performance, and known issues are discussed in §5.2.

4.3.2. Astrometric Calibration

Starting from the astrometric solution calculated in single frame processing (§4.2), the final astrometric solution is computed using the ensemble of visits in a given band that overlap a given **tract**. This allows the astrometric solution to be further refined by using all of the isolated point sources of sufficient signal-to-noise ratio in an image, rather than only those that appear in the reference catalog, as is done in single frame processing. Using multiple whole visits rather than a single detector also allows us to account for effects that impact the full focal plane, and for the proper motion and parallax of the sources.

In order to perform the fit of the astrometric solution, isolated point sources are associated between overlapping visits and with the **Gaia DR3** (Gaia Collaboration et al. 2023b) reference catalog where possible. The

1539 model used for DP1 consists of a static map from pixel
 1540 space to an intermediate frame (the per-detector model),
 1541 followed by a per-visit map from the intermediate frame
 1542 to the plane tangent to the telescope boresight (the per-
 1543 visit model), then finally a deterministic mapping from
 1544 the tangent plane to the sky. The fit is done using the
 1545 `gbdes` package (G. M. Bernstein et al. 2017), and a full
 1546 description is given in C. Saunders (2024).

1547 The per-detector model is intended to capture quasi-
 1548 static characteristics of the telescope and camera. Dur-
 1549 ing *Rubin Operations*, the astrometric solution will al-
 1550 low for separate epochs with different per-detector mod-
 1551 els, to account for changes in the camera due to warm-
 1552 ing and cooling and other discrete events. However, for
 1553 DP1, LSSTComCam was assumed to be stable enough
 1554 that all visits use the same per-detector model. The
 1555 model itself is a separate two-dimensional polynomial for
 1556 each detector. For DP1, a degree 4 polynomial was used;
 1557 the degree of the polynomial mapping is tuned for each
 1558 instrument and may be different for LSSTCam. Fur-
 1559 ther improvements may be made by including a pixel-
 1560 based astrometric offset mapping, which would be fit
 1561 from the ensemble of astrometric residuals, but this is
 1562 not included in the DP1 processing.

1563 The per-visit model attempts to account for the path
 1564 of a photon from both atmospheric sources and those
 1565 dependent on the telescope orientation. This model is
 1566 also a polynomial mapping, in this case a degree 6 two-
 1567 dimensional polynomial. Correction for DCR (§5.4) was
 1568 not done for DP1, but will be included in LSSTCam pro-
 1569 cessing during *Rubin Operations*. Future processing will
 1570 also likely include a Gaussian Process fit to better ac-
 1571 count for atmospheric turbulence, as was demonstrated
 1572 by W. F. Fortino et al. (2021) and P. F. Léget et al.
 1573 (2021).

1574 The final component of the astrometric calibration
 1575 involves the positions of the isolated point sources in-
 1576 cluded in the fit, which are described by five parameters:
 1577 sky coordinates, proper motion, and parallax. While
 1578 proper motions and parallaxes are not released for DP1,
 1579 they are fitted for these sources in the astrometric solu-
 1580 tion to improve the astrometric calibration.

1581 4.3.3. Photometric Calibration

1582 Photometric calibration of the DP1 dataset is based
 1583 on the *Forward Global Calibration Method (FGCM)*
 1584 (D. L. Burke et al. 2018), adapted for the LSST Sci-
 1585 ence Pipelines (H. Aihara et al. 2022; P. Fagrelius &
 1586 E. S. Rykoff 2025). We used the FGCM to calibrate
 1587 the full DP1 dataset with a forward model that uses a
 1588 parameterized model of the atmosphere as a function of
 1589 airmass along with a model of the instrument through-

1590 put as a function of wavelength. The FGCM process
 1591 typically begins with measurements of the instrumental
 1592 throughput, including the mirrors, filters, and detectors.
 1593 However, because full scans of the LSSTComCam as-
 1594 built filters and individual detectors were not available,
 1595 we instead used the nominal reference throughputs for
 1596 the Simonyi Survey Telescope and LSSTCam.⁹⁸ These
 1597 nominal throughputs were sufficient for the DP1 cali-
 1598 bration, given the small and homogeneous focal plane
 1599 consisting of only nine ITL detectors. The FGCM atmo-
 1600 sphere model, provided by MODTRAN (A. Berk et al.
 1601 1999), was used to generate a look-up table for atmo-
 1602 spheric throughput as a function of zenith distance at
 1603 Cerro Pachón. This model accounts for absorption and
 1604 scattering by molecular constituents of the atmosphere,
 1605 including O_2 and O_3 ; absorption by water vapor; and
 1606 Mie scattering by airborne aerosol particulates. Nightly
 1607 variations in the atmosphere are modeled by minimiz-
 1608 ing the variance in repeated observations of stars with
 1609 a *Signal to Noise Ratio (SNR)* greater than 10, mea-
 1610 sured using “compensated aperture fluxes”. These fluxes
 1611 include a local background subtraction (see §4.2.2) to
 1612 mitigate the impact of background offsets. The model
 1613 fitting process incorporates all six bands (*ugrizy*) but
 1614 does not include any gray (achromatic) terms, except
 1615 for a linear assumption of mirror reflectance degrada-
 1616 tion, which is minimal over the short duration of the
 1617 DP1 observation campaign. As an additional constraint
 1618 on the fit, we use a subset of stars from the reference
 1619 catalog (P. S. Ferguson et al. 2025), primarily to con-
 1620 strain the system’s overall throughput and establish the
 1621 “absolute” calibration.

1622 Photometric transformation relations between LSST-
 1623 Cam and LSSTComCam systems and other photomet-
 1624 ric systems are under development and are provided in
 1625 (M. N. Porter et al. 2025)

1626 4.4. Visit Images and Source Catalogs

1627 With the final PSF models, WCS solutions, and pho-
 1628 tometric calibrations in place, we reprocess each single-
 1629 epoch image to produce a final set of calibrated visit
 1630 images and source catalogs. Source detection is per-
 1631 formed down to a 5σ threshold using the updated PSF
 1632 models, followed by measurement of PSF and aperture
 1633 fluxes. These catalogs represent the best single-epoch
 1634 source characterization, but they are not intended for
 1635 constructing light curves. For time-domain analysis,
 1636 we recommend using the *forced photometry* tables de-
 1637 scribed in §4.6.2.

⁹⁸ Available at: <https://github.com/lstt/throughputs/tree/1.9>

4.5. Coaddition Processing

4.5.1. Coaddition

Only exposures with a *seeing* better than 1.7 arcseconds FWHM are included in the deep coadded images. For the template coadds, typically only the top third of visits with the best *seeing* are used (although see §3.1 for more details), resulting in an even tighter image quality cutoff for the template coadds. Exposures with poor PSF model quality, identified using internal diagnostics, are excluded to prevent contamination of the coadds with unreliable PSF estimates. The remaining exposures are combined using an inverse-variance weighted mean stacking algorithm.

To mitigate transient artifacts before coaddition, we apply the artifact rejection procedure described in Y. Al-Sayyad (2018) that identifies and masks features such as satellite trails, optical ghosts, and cosmic rays. It operates on a time series of PSF-matched images resampled onto a common pixel grid (“warps”) and leverages their temporal behavior to distinguish persistent astrophysical sources from transient artifacts.

Artifact rejection uses both direct (where no PSF-matching is performed) and PSF-matched warps, homogenized to a standard PSF of 1.8 arcseconds FWHM, broadly consistent with the 1.7 arcsecond FWHM *seeing* threshold used in data screening. A sigma-clipped mean of the PSF-matched warps serves as a static sky model, against which individual warps are differenced to identify significant positive and negative residuals. Candidate artifact regions are classified as *transient* if they appear in less than a small percentage of the total number of exposures, with the threshold based on the number of visits, N , as follows:

- $N = 1$ or 2 : threshold = 0 (no clipping).
- $N = 3$ or 4 : threshold = 1.
- $N = 5$: threshold = 2.
- $N > 5$: threshold = $2 + 0.03N$.

Identified *transient* regions are masked before coaddition, improving image quality and reducing contamination in derived catalogs.

4.5.2. Detection, Deblending and Measurement

After constructing coadded images, sources are detected in each band, merged across bands, deblended, and measured to generate the final object catalogs (§3.2). For each coadd in all six bands, we perform source detection at a 5σ detection threshold and then adjust the background with a per-patch constant (coadds are built from background-subtracted images,

but the deeper detection on coadds redefines what is considered source versus background). Detections across bands are merged in a fixed priority order, *irzygu*, to form a union detection catalog, which serves as input to deblending.

Deblending is performed using the Scarlet Lite algorithm, which implements the same model as Scarlet (P. Melchior et al. 2018), but operates on a single pixel grid. This allows the use of analytic gradients, resulting in greater computational speed and memory efficiency.

Object measurement is then performed on the deblended detection footprints in each band. Measurements are conducted in three modes: independent per-band measurements, forced measurements in each band, and multiband measurements.

Most measurement algorithms operate through a single-band plugin system, largely as originally described in J. Bosch et al. (2018). The same plugins are run separately for each object on a deblended image, which uses the Scarlet model as a template to re-weight the original noisy coadded pixel values. This effectively preserves the original image in regions where objects are not blended, while dampening the noise elsewhere.

A reference band is chosen for each object based on detection significance and measurement quality using the same priority order as detection merging (*irzygu*) and a second round of measurements is performed in forced mode using the shape and position from the reference band to ensure consistent colors (J. Bosch et al. 2018).

Measurement algorithm outputs include object fluxes, centroids, and higher-order moments thereof like sizes and shapes. A variety of *flux* measurements are provided, from aperture fluxes and forward modeling algorithms.

Composite model (CModel) magnitudes (K. Abazajian et al. 2004; J. Bosch et al. 2018) are used to calculate the extendedness parameter, which functions as a star-galaxy classifier. Extendedness is a binary classifier that is set to 1 if the PSF model flux is less than 98.5% of the (free, not forced) CModel flux in a given band. Additionally, the extendedness in the reference band is provided as a separate column for convenience as a multiband star-galaxy classification, and is recommended generally but also specifically for objects with low signal-to-noise ratio in some bands.

Gaussian-Aperture-and-PSF (Gaussian Aperture and PSF (GAaP) K. Kuijken 2008; A. Kannawadi 2025) fluxes are provided to ensure consistent galaxy colors across bands. Sérsic model (J. L. Sérsic 1963; J. L. Sérsic 1968) fits are run on all available bands simultaneously (MultiProFit, D. S. Taranu 2025). The resulting Sérsic model fluxes are provided as an alternative to CModel

and are intended to represent total galaxy fluxes. Like CModel, the Sérsic model is a Gaussian mixture approximation to a true Sérsic profile, convolved with a Gaussian mixture approximation to the PSF. Sérsic model fits also include a free centroid, with all other structural parameters shared across all bands. That is, the intrinsic model has no color gradients, but the convolved model may have color gradients if the PSF parameters vary significantly between bands.

CModel measurements use a double “shapelet” (A. Refregier 2003) PSF model with a single shared shape. The Sérsic fits are intended to use a double Gaussian with independent shape parameters for each component. Due to a pipeline misconfiguration, the Sérsic fits actually used the shapelet PSF parameters, with the higher-order terms ignored (since MultiProFit does not support shapelet PSFs). This bug is not expected to impact the galaxy fluxes significantly, since the higher-order shapelet PSF parameters tend to be small, and the fix will be applied in future campaigns. Either way, the double Gaussian PSF parameters are included for each object.

Further details on the performance of these algorithms are found in §5.7.

4.6. Variability Measurement

4.6.1. Difference Imaging Analysis

Difference Image Analysis (DIA) uses the decorrelated Alard & Lupton image differencing algorithm (D. J. Reiss & R. H. Lupton 2016). We detected both positive and negative DIASources at 5σ in the difference image. Sources with footprints containing both positive and negative peaks due to offsets from the template position or blending were fit with a dipole centroid code, which simultaneously fits offset positive and negative PSFs. We filter the resulting DIASource catalog to remove detections with pixel flags indicative of artifacts, non-astrophysical trail lengths, or unphysically negative direct fluxes. Finally, we perform a simple spatial association of DIASources into DIAObjects using a one-arcsecond matching radius.

The Machine Learning reliability model applied to DP1 was developed with the aim to meet the latency requirements for Rubin Alert Production when executed on CPUs. Accordingly we developed a relatively simple model: a Convolutional Neural Network with three convolutional layers, and two fully connected layers. The convolutional layers have a 5×5 kernel size, with 16, 32, and 64 filters, respectively. A max-pooling layer of size 2 is applied at the end of each convolutional layer, followed by a dropout layer of 0.4 to reduce overfitting. The last fully connected layers have sizes of 32 and 1. The ReLU

activation function is used for the convolutional layers and the first fully connected layer, while a sigmoid function is used for the output layer to provide a probabilistic interpretation. The cutouts are generated by extracting postage stamps of 51×51 pixels centered on the detected sources. The input data of the model consist of the template, science, and difference image stacked to have an array of shape (3, 51, 51). The model is implemented using PyTorch (J. Ansel et al. 2024). The Binary Cross Entropy loss function was used, along with the Adaptive Moment Estimation (Adam) optimizer with a fixed learning rate of 1×10^{-4} , weight decay of 3.6×10^{-2} , and a batch size of 128. The final model uses the weights that achieved the best precision/purity for the test set. Training was done on the SLAC Shared Scientific Data Facility (S3DF) with an NVIDIA model L40S GPU.

The model was initially trained using simulated data from the second DESC Data Challenge (DC2; (LSST Dark Energy Science Collaboration (LSST DESC) et al. 2021)) plus randomly located injections of PSFs to increase the number of real sources, for a total of 89,066 real sources. The same number of bogus sources were selected at random from non-injected DIASources. Once the LSSTComCam data were available, the model was fine-tuned on a subset of the data containing 183,046 sources with PSF injections. On the LSSTComCam test set, the model achieved an accuracy of 98.06%, purity of 97.87%, and completeness of 98.27%. As discussed in §5.8, the injections used to train this model version do not capture all types of astrophysical variability, so performance on the test set will not be representative for variable stars, comets, and other types of variable objects. The machine-learning reliability score, reported in the reliability column of the DIASource catalog, is a scalar value between 0 and 1 that quantifies the model’s confidence that a given detection is astrophysical.

4.6.2. Light Curves

To produce light curves, we perform multi-epoch forced photometry on both the direct visit images and the difference images. For light curves we recommend the forced photometry on the difference images (psDiffFlux on the ForcedSource Table), as it isolates the variable component of the flux and avoids contamination from static sources. In contrast, forced photometry on direct images includes flux from nearby or blended static objects, and this contamination can vary with seeing. Centroids used in the multi-epoch forced photometry stage are taken either from object positions measured on the coadds or from the DIAObjects (the associated DIASources detected on difference images).

4.6.3. Solar System Processing

Solar system processing in DP1 consists of two key components: the association of observations (sources) with known solar system objects, and the discovery of previously unknown objects by linking sets of *tracklets*⁹⁹.

The association component begins by generating expected positions for all objects in the Minor Planet Center orbit catalog, using ephemerides computed with the *Sorcha* survey simulation toolkit (Merritt et al., in press)¹⁰⁰. To enable fast lookup of objects potentially present in an observed visit, we use the *mpsky* package (M. Juric 2025). In each image, the closest *DiaSource* within 1 arcsecond of a known solar system object’s predicted position is associated to that object. In DP1 we used a simple positional association to tag *DiaSources* that are likely observations of known asteroids. The 1 arcsecond radius is intentionally generous; we did not see evidence of mismatches at DP1 depth and volume. This radius will be tuned for future processing campaigns.

The discovery component of Solar System processing uses the *heliolinx* package¹⁰¹, which provides tools for asteroid identification and linking (A. Heinze et al. 2023). The repository contains code for the following tasks:

- Tracklet creation with `make_tracklets`
- Multi-night *tracklet* linking with an algorithm
- Linkage post processing (orbit fitting, outlier rejection, and de-duplication) with `link_purify`

The inputs to the discovery processing comprised all sources detected in difference images, regardless of whether they were tagged in the association step. These inputs were produced by an early processing of *LSST-ComCam* commissioning data, some of which were later rejected during DP1 processing and therefore do not appear in the final DP1 data products.

About 10% of all commissioning visits targeted the near-ecliptic field *Rubin_SV_38_7*, chosen to facilitate asteroid discovery. *Rubin_SV_38_7* produced the vast majority of asteroid discoveries in DP1, as expected, but a few were found in off-ecliptic fields as well.

Tracklet creation with `make_tracklets` used an upper limit angular velocity of 1.5 *deg/day*, faster than any main belt asteroid and in the range of many *Near-*

Earth Object (NEO) discoveries. While no formal minimum angular velocity was imposed, in practice it would be unlikely to detect objects moving slower than about 0.01 *deg day*⁻¹. To minimize false *tracklets* from fields observed multiple times per night, the minimum *tracklet* length was set to three detections, and a minimum on-sky motion of five arcseconds was required for a valid *tracklet*. To claim a discovery candidate, we required *tracklets* to be linked across at least three nights.

Multi-night *tracklet* linking is the heart of Solar system discovery, which connects (“links”) *tracklets* belonging to the same object over a series of nights. It employs the *HelioLinC3D* algorithm (S. Eggl et al. 2020; A. Heinze et al. 2022), a refinement of the original *HelioLinC* algorithm of M. J. Holman et al. (2018). Each processing run tested each *tracklet* with 324 different hypotheses spanning heliocentric distances from 1.5 to 9.8 *astronomical unit (au)* and radial velocities spanning the full range of possible bound orbits (eccentricity 0.0 to nearly 1.0). The upper limit of 10 *au* was chosen because searches targeting more distant populations require different parameter choices. This range of distance encompasses all main belt asteroids and Jupiter Trojans, as well as many comets and Mars-crossers and some *NEOs*. A dedicated search for objects at heliocentric distances out to 50 *au* was also conducted; no distant objects were detected, consistent with expectations for the size of the DP1 data set. Smaller heliocentric distances were not attempted here because nearby objects move rapidly across the sky and hence were not likely to remain long enough in an *LSSTComCam* field to be discovered.

Candidate linkages, defined as groups of *tracklets* whose propagated orbits cluster within a radius of 1.33×10^3 *au* at 1 *au*, are identified, then post-processed via `link_purify` to yield a final, non-overlapping set of high-confidence asteroid candidates, ranked by orbit-fit residuals and related metrics. While *heliolinx* can produce false-positive or redundant raw linkages by design, these are filtered during post-processing by `link_purify`, which applies a Rubin-specific, more stringent version of the MPC validation rules¹⁰². This step both rejects spurious linkages and deduplicates multiple hypotheses for the same object, ensuring that only the highest-quality, non-redundant linkages are carried forward for orbit determination and for distinguishing new discoveries from rediscoveries of known objects.

⁹⁹ A *tracklet* is defined as two or more detections of a moving object candidate taken in close succession in a single night.

¹⁰⁰ Available at <https://github.com/dirac-institute/sorcha>

¹⁰¹ <https://github.com/heliolinx/heliolinx>

¹⁰² <https://minorplanetcenter.net/mpcops/documentation/identifications/additional/>

5. PERFORMANCE CHARACTERIZATION AND KNOWN ISSUES

In this section, we provide an assessment of the DP1 data quality and known issues.

5.1. Sensor Anomalies and ISR

In addition to the known detector features identified before LSSTComCam commissioning, most of which are handled by the ISR processing (see §4.2.1), we discovered a number of new types of anomalies in the DP1 data. Since no corrections are currently available for these anomalies, they are masked and excluded from downstream data products.

5.1.1. Vampire Pixels

“Vampire” pixels are visible on the images as a bright defect surrounded by a region of depressed flux, as though the defect is stealing charge from its neighboring pixels. Figure 12 shows an example of a vampire pixel near the center of R22_S11 on an *r*-band flat.

From studies on evenly illuminated images, vampires appear to conserve charge. Unfortunately, no unique optimum way exists to redistribute this stolen flux so, following visual inspection, a defect mask was created to exclude them from processing. We have found some similar features on the ITL detectors on LSSTCam, and will use the same approach to exclude them.

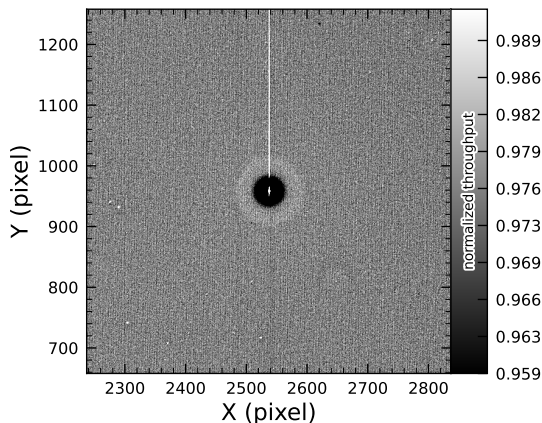


Figure 12. A large vampire pixel near the center of R22_S11, as seen on the *r*-band flat. This clearly shows the central hot “vampire” pixels, surrounded by a region of depressed signal, with a brighter ring surrounding that caused by the local electric field effects. The charge contained in the central pixels is incompletely shifted as the image is read, and that charge leaks out into subsequent rows as they are shifted through the remnant charge. The columns that contain the hot pixels are masked as defects in all processing, as this feature cannot be otherwise corrected.

5.1.2. Phosphorescence

Some regions of the LSSTComCam CCD raft were seen to contain large numbers of bright defects. An example is shown in Figure 13 in a *g*-band flat. On further investigation, it appears that on some detectors a layer of photoresist wax was incompletely removed from the detector surface during production. As this wax is now trapped below the surface coatings, there is no way to physically clean these surfaces. If this wax responded to all wavelengths equally, then it would likely result in quantum efficiency dips, which might be removable during flat correction. However, it appears that this wax is slightly phosphorescent, with a decay time on the order of minutes, resulting in the brightness of these defects being dependent on the illumination of prior exposures. The worst of these regions were excluded with manual masks.

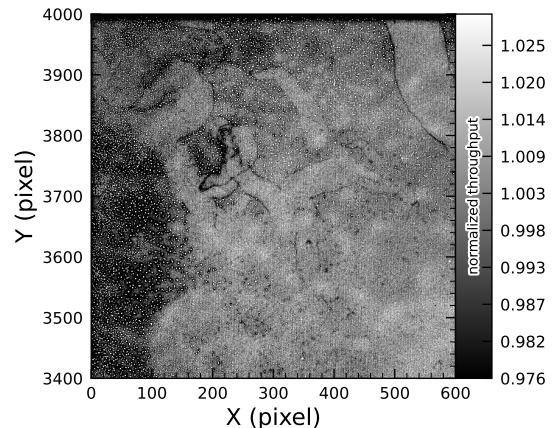


Figure 13. The top left corner of R22_S01 in the *g*-band flat, showing the many small defect features that are caused by the remnant photoresist wax. A single large defect box masks this region from further analysis to prevent these features from contaminating measurements.

5.1.3. Crosstalk

Crosstalk refers to unwanted signal interference between adjacent pixels or amplifiers. We use an average inter-amp crosstalk correction based on laboratory measurements with LSSTCam. These average corrections proved satisfactory, and so have been used as-is for DP1 processing. There are, however, some residual crosstalk features present post-correction, with a tendency towards over-subtraction. Figure 14 shows an example of a bright star with over-subtracted crosstalk residuals visible on neighboring amplifiers to both sides on exposure 2024120600239, detector R22_S02.

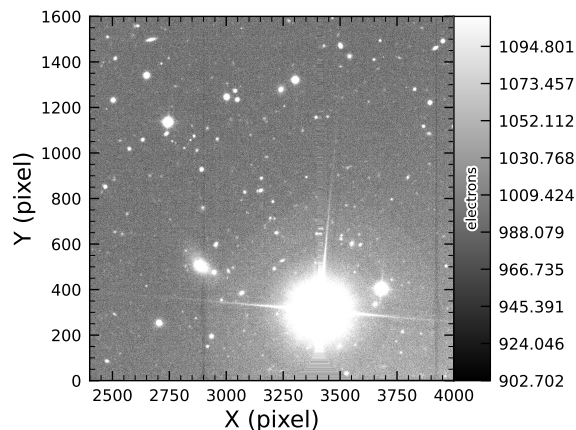


Figure 14. An example of a bright star with over-subtracted crosstalk residuals visible on neighboring amplifiers to both sides (exposure 2024120600239, detector R22_S02). The horizontal banding pattern from the center of the star shows the interpolation stretching covering the saturated core and the ITL edge bleed near the serial register.

5.1.4. Bleed Trails

Bleed trails are produced when charge from saturated pixels spills into adjacent pixels. Bleed trails were anticipated on [LSSTComCam](#) sensors, but they appear in more dramatic forms than had been expected. As a bleed trail nears the serial register, it fans out into a “trumpet” shaped feature. Although bright, these features do not have consistently saturated pixels. In [DP1](#) these “edge bleeds” were identified and masked.

Saturated sources can create a second type of bleed, where the central bleed drops below the background level. The depressed columns along these trails extend across the entire readout column of the detector, crossing the detector mid-line. We developed a model for these to identify which sources are sufficiently saturated to result in such a trail, which is then masked. As this kind of trail appears only on the ITL detectors, we’ve named these features “ITL dips”. [Figure 15](#) shows an example of a bright star exhibiting the “ITL dip” phenomenon on exposure: 2024121000503, detector: R22_S21.

5.2. PSF Models

To characterize PSF performance, we use adaptive second moments ([G. M. Bernstein & M. Jarvis 2002](#)) measured on PSF stars and on the PSF model using the [HSM](#) implementation ([C. Hirata & U. Seljak 2003](#); [R. Mandelbaum et al. 2005](#)). All measurements are expressed in the pixel coordinate frame of each detector. We characterize the performance of the PSF using the classical trace of the second moment matrix T , along

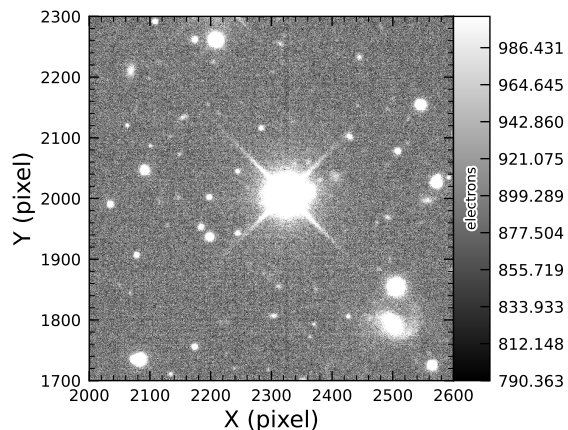


Figure 15. A bright star showing the “ITL dip” phenomenon, in which a dark trail extends out from the star to the top and bottom edges of the detector (exposure: 2024121000503, detector: R22_S21).

with the ellipticity parameters e^1 and e^2 . Measurements on the observed PSF stars are denoted as T_{PSF} , e_{PSF}^1 , e_{PSF}^2 , while those from PSF models are denoted as T_{model} , e_{model}^1 , e_{model}^2 . We compare two PSF modeling approaches:

- Piff with second-order polynomial interpolation (Piff O2), the pipeline’s default, and
- Piff with fourth-order polynomial interpolation (Piff O4), which serves as the final [DP1](#) PSF model.

[Table 5](#) summarizes each model’s ability to reconstruct the mean T , e^1 , and e^2 on [LSSTComCam](#). Both models exhibit a negative residual bias in the reconstructed PSF size, with Piff O4 providing improved performance over Piff O2.

An alternative approach to evaluating the performance of the PSF model is to examine the average $\delta T/T$, where δT is $T_{\text{PSF}} - T_{\text{model}}$, across visits, projected onto focal-plane coordinates, as shown in [Figure 16](#). Piff reveals strong spatial correlations in the residuals, including a systematic offset consistent with the results presented in [Table 5](#). The presence of these spatial structures motivated the adoption of fourth-order polynomial interpolation in all bands except u -band. Although not shown in [Figure 16](#), residual patterns persist even with third-order interpolation, indicating that it is insufficient to capture the complexity of the PSF variation. Increasing the interpolation order to five would nominally reduce the residuals further, but the limited number of stars available on some CCDs would not provide adequate constraints for such a model, while the resulting improvement would likely be minimal. Preliminary

Table 5. Observed mean values and comparison of model residuals, across all visits and filters

Quantity	Observed	Piff O2	Piff O4
		$\times 10^{-4}$	$\times 10^{-4}$
$\langle T \rangle$ (pixel ²)	11.366 ± 0.003		
$\langle e^1 \rangle$	$(-6.07 \pm 0.05) \times 10^{-3}$		
$\langle e^2 \rangle$	$(-4.57 \pm 0.05) \times 10^{-3}$		
$\langle e \rangle$	$(8.794 \pm 0.004) \times 10^{-2}$		
$\langle \delta T/T \rangle$		-4.0 ± 0.2	-5.0 ± 0.2
$\langle \delta e^1 \rangle$		0.6 ± 0.1	0.5 ± 0.1
$\langle \delta e^2 \rangle$		0.0 ± 0.1	0.0 ± 0.1

analysis of LSSTCam data in the laboratory at SLAC National Accelerator Laboratory (SLAC) shows that the ITL sensors exhibit the same pattern as ITL sensors on LSSTComCam.

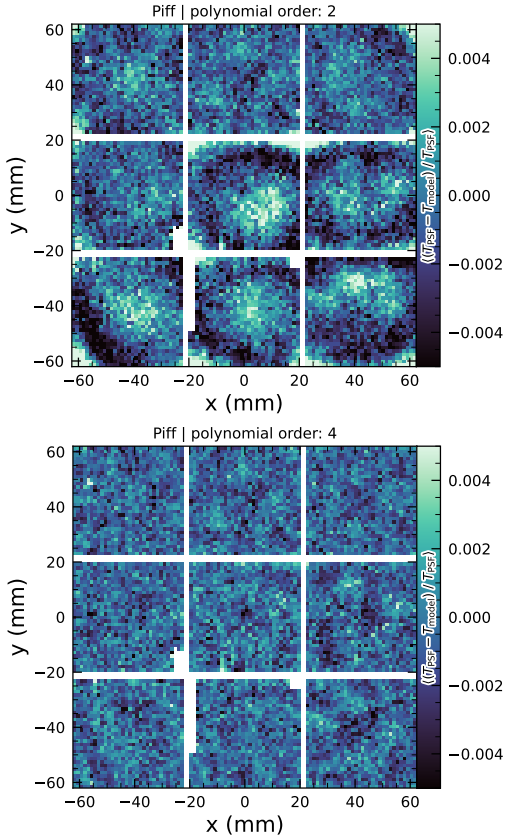


Figure 16. Average across all visits of $\delta T/T$ for Piff O2 and Piff O4 modeling on LSSTComCam. Averages are computed using a 120×120 binning.

Another way to look at the PSF modeling quality is via whisker plots of the PSF second and fourth moments

and their modeling residuals projected on a part of the sky. In addition to the second moment, the spin-2 fourth moments, $e^{(4)}$, are defined as:

$$e_1^{(4)} = M_{40} - M_{04}$$

$$e_2^{(4)} = 2(M_{31} - M_{13}),$$

where M_{pq} are the standardized higher moments as defined in T. Zhang et al. (2023) measured on stars and PSF models. Figure 17 shows the whisker plots of e , $e^{(4)}$ (top rows), and δe , $\delta e^{(4)}$ in the ECDFS field. The direction of a whisker represents the orientation of the shape, while the length represents the amplitude $|e|$ or $|e^{(4)}|$. We observe coherent patterns in both the PSF moments and the residuals, the latter of which warrants further investigation if it persists in future data releases.

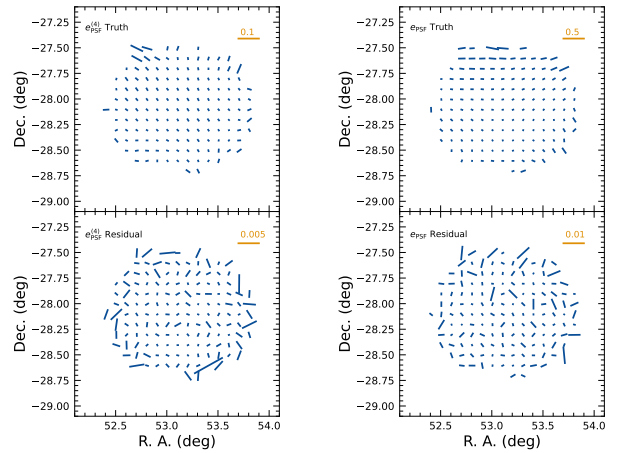


Figure 17. Whisker plots for the ECDFS field for e , $e^{(4)}$ and δe , $\delta e^{(4)}$.

Figure 18 shows a plot of $\delta T/T$ versus stellar magnitude, which can reveal any dependencies between PSF size and flux. We also repeat this analysis in color bins

to probe chromatic effects. Binning by color uncovers a clear color dependence, as was also seen in DES (M. Jarvis et al. 2021). The residual is consistent with Table 5 and its cause is unknown. DP1 does not include the color correction implemented in the DES Year 6 analysis, T. Schutt et al. (2025). This will be included in processing of future data releases.

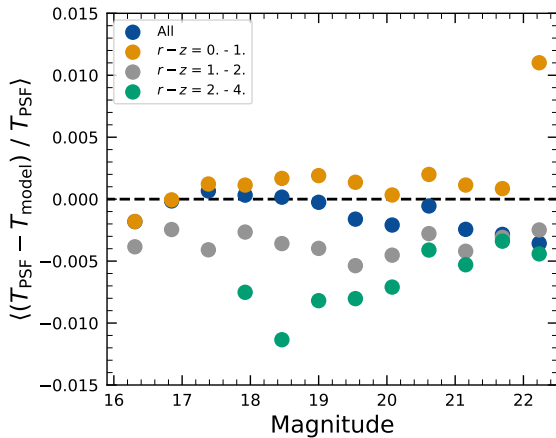


Figure 18. Binned $\delta T/T$ as a function of magnitude across all visits and filters and in bins of stellar colors.

As noted in Rubin Observatory Science Pipelines Developers (2025), two key Piff features were not used in the DP1 processing. PSF color dependence was not implemented, and, while Rubin software allows Piff to work with sky coordinates (including WCS transformations), it does not yet correct for sensor-induced astrometric distortions such as tree rings (H. Y. Park et al. 2017). Both features are planned for upcoming releases.

5.3. Astrometry

To characterize astrometric performance, we evaluate both internal consistency and agreement with an external reference. The primary measure of internal consistency is the repeatability of position measurements for the same object, defined as the RMS of the astrometric distance distribution for stellar pairs having a specified separation in arcminutes. We associate isolated point sources across visits and compute the rms of their fitted positions, rejecting any stars with another star within $2''$. Figure 19 shows the mean per-tract rms astrometric error in RA for all isolated point sources, both after the initial calibration and after the final calibration, which includes proper motion corrections. The results indicate that the astrometric solution is already very good after the initial calibration. Global calibration yields only modest improvement, likely due to the short time span

of DP1 and the minimal distortions in the LSSTCom-Cam. In the main survey, the longer time baseline and greater distortions near the LSSTCam field edges will make global calibration more impactful. An additional

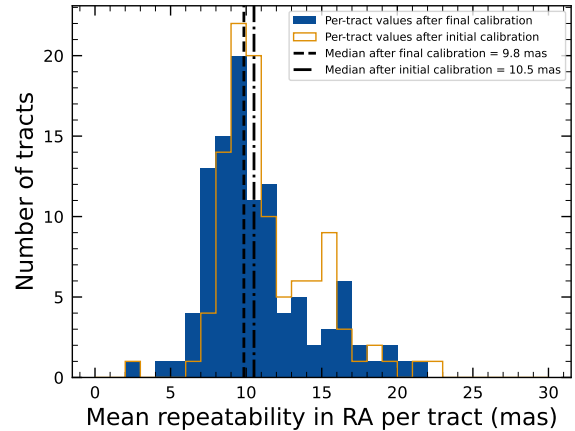


Figure 19. Mean per-tract astrometric repeatability of measurements of isolated point sources in RA in visits across all bands.

measure of internal consistency is the repeatability of separations between objects at a given distance. To compute this, we identify pairs of objects that are separated by a specified distance and measure their precise separation during each visit in which both objects are observed. The scatter in these separation measurements provides an indication of the internal consistency of the astrometric model. Figure 20 shows the median separation for pairs of objects separated by approximately 5 arcminutes (referred to as “AM1”), computed per tract after the final calibration. These values are already approaching the design requirement of 10 mas.

To assess external consistency, we consider the median separation between sources not included in the astrometric fit and associated objects from a reference catalog (§3.3.3). For this, we use the Gaia DR3 catalog, with the object positions shifted to the observation epoch using the Gaia proper motion parameters. Figure 21 shows the median separation for each visit in the r -band in tract 4849 in the ECDFS fields. The calculated values are almost all within 5 mas, well below the design requirement of 50 mas for the main survey. By examining the astrometric residuals, we can assess whether there are distortions not accounted for by the astrometric model. In some cases, residuals from a single visit exhibit behavior consistent with atmospheric turbulence, as shown in Figure 22, which is characterized by a curl-free gradient field in the two-point correlation function of the residuals (E-mode), P. F. Léget et al. (2021) and W. F. Fortino

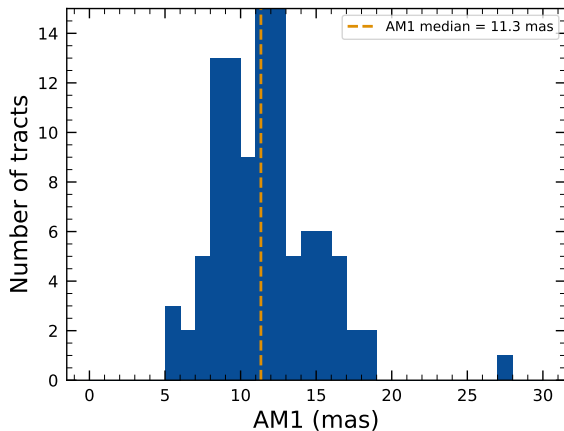


Figure 20. Median per-tract repeatability in separations between isolated point sources 5 arcmin apart (AM1) in visits across all bands.

et al. (2021). However, as seen in Figure 23, the residuals in many visits also have correlation functions with a non-negligible divergence-free B-mode, indicating that some of the remaining residuals are due to unmodeled instrumental effects, such as rotations between visits.

We can see unmodeled camera distortions by stacking the astrometric residuals over many visits as a function of the focal plane position. Figure 24 shows the median residuals in x and y directions for 1792 visits. Spatial structures are evident at the CCD level, as well as at the mid-line break, the discontinuity between the two rows of amplifiers, in the y -direction residuals. Further stacking all the detectors makes certain effects particularly clear. Figure 25 shows distortions very similar to those measured for an LSSTCam ITL sensor in a laboratory setting in J. H. Esteves et al. (2023).

5.4. Differential Chromatic Refraction

DCR occurs when light passes through Earth’s atmosphere, refracting more for shorter wavelengths, which causes blue light to appear shifted closer to the zenith. This wavelength-dependent effect results in the smearing of point sources along the zenith direction, specifically parallel to the parallactic angle. The DCR effect is observable in LSSTComCam data, particularly in the angular offset versus $g - i$ band magnitude difference plots, as shown in Figure 26. These plots include 228 visits selected to maximize the range of observed airmass, which spans 1.01–1.30 with a mean value of 1.13. When looking at data perpendicular to the parallactic angle, sources exhibit no discernible DCR effect, which is expected, and form a clear vertical distribution on the two-dimensional density plots in Figure 26.

In contrast, sources aligned with the parallactic angle exhibit a tilted, linear distribution, clearly demonstrating that the relationship between angular offset and the $g - i$ band magnitude difference, thereby providing a visual indication of the DCR effect. The DCR effect will be addressed in future releases.

5.5. Stellar Photometry

The photometric repeatability for isolated bright unresolved sources following the FGCM fits was excellent. For the 10% of unresolved sources withheld from the fit and having signal-to-noise ratios greater than 100, the photometric repeatability after applying chromatic correction was 7.1, 5.4, 5.4, 5.1, 5.9, and 6.5 mmag in the $ugrizy$ bands respectively, across all fields. After accounting for photometric noise, the intrinsic photometric repeatability was approximately 4.8, 2.7, 1.7, 1.0, 2.0, and 1.1 mmag in $ugrizy$. The DP1 processing does not yet include chromatic corrections in the final photometry. In this case the delivered photometric repeatability was 3–8 mmag for $grizy$.

In Figure 27, we show the stellar loci for $ugriz$ for unresolved sources in the DP1 Object table (§3.2). These unresolved sources were selected using the extendedness parameter (§3.2) in the Object catalog. This parameter is assigned a value of 0 (unresolved) or 1 (resolved) in each band based on the difference between the PSF and CModel magnitudes. The extendedness is set to 1 when this magnitude difference exceeds 0.016 mag, as the PSF flux for extended sources is biased low relative to the CModel flux. This method has been previously employed by the SDSS pipelines, and its statistical properties, including the optimal combination of information from different bands and repeated measurements, are discussed in C. T. Slater et al. (2020).

Figure 28 illustrates the behavior of the extendedness parameter. Its behavior in the g and r bands is similar, with unresolved sources scattered around the vertical line centered on zero. The width of the distribution increases towards fainter magnitudes. Resolved sources are found to the right and the dashed lines in the top panels show the adopted “star-galaxy” separation boundary. The morphology of the two color-magnitude diagrams in the bottom panels suggest that the unresolved sample suffers from increasing contamination by galaxies for $r > 24$. This behavior is consistent with simulation-based predictions from C. T. Slater et al. (2020).

5.6. Detection Completeness on Coadds

We characterize completeness by injecting synthetic sources into coadded images, and by comparing source

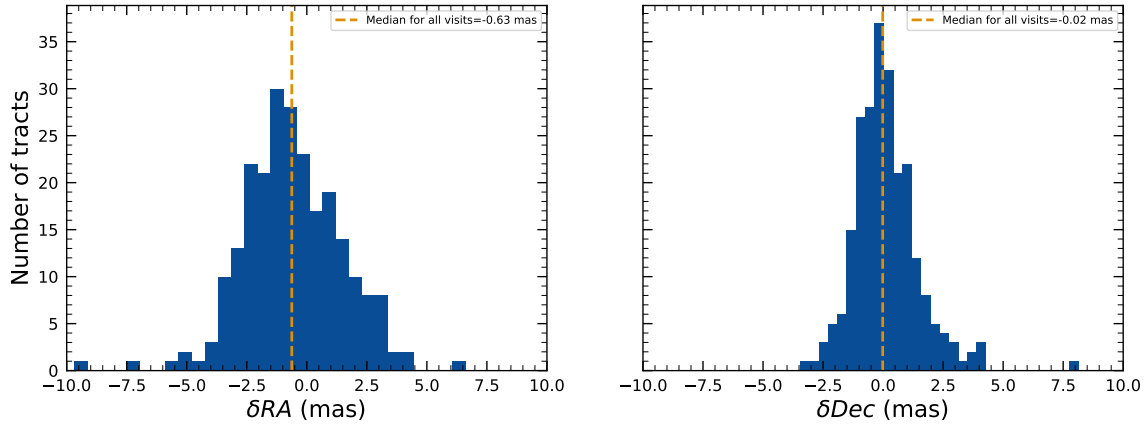


Figure 21. Median absolute offset for all visits in r -band in [tract 4849](#) in the ECDFS field. The offset is the difference between the positions of isolated point sources that were reserved from the astrometric fit and matched objects from the Gaia DR3 catalog.

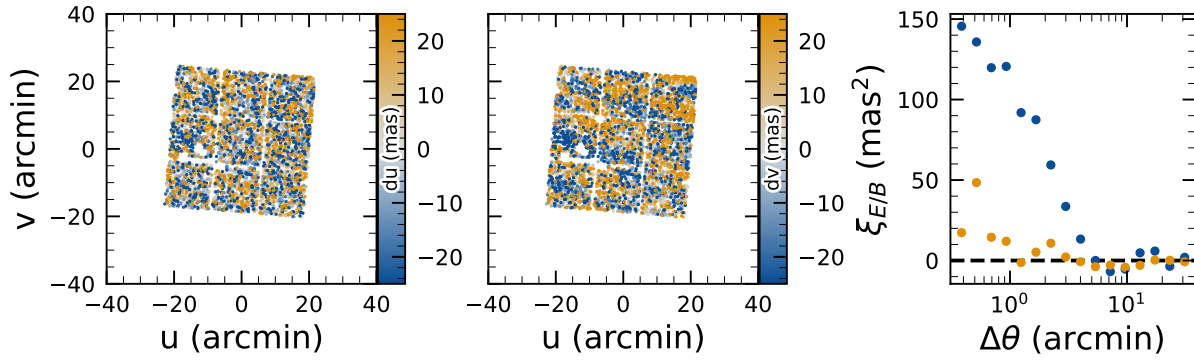


Figure 22. Astrometric residuals in u (left panel) and v (center panel) directions with the E (blue) and B (orange) modes of the two-point correlation function (right panel) seen in visit 2024120200359 in [tract 2393](#) in u band. The residuals show a wave-like pattern characteristic of atmospheric turbulence, and there is significant E-mode and negligible B-mode in the correlation function.

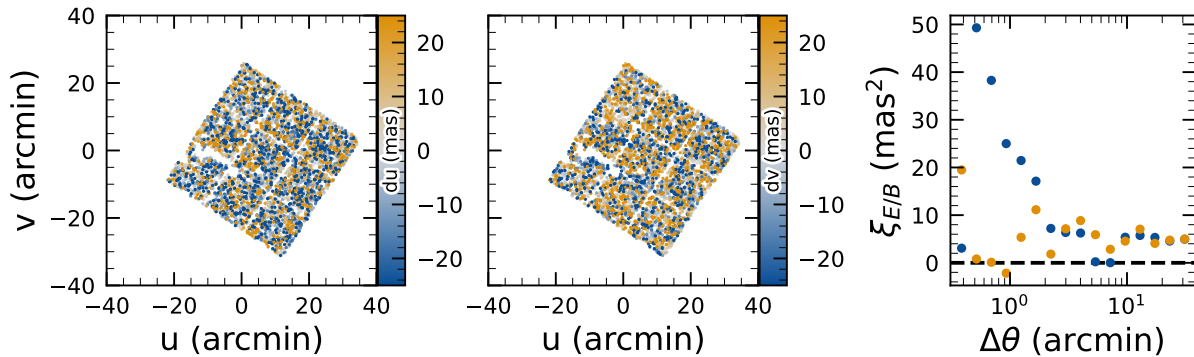


Figure 23. Astrometric residuals in u (left panel) and v (center panel) directions, with the E (blue) and B (orange) modes of the two-point correlation function (right panel) seen in visit 2024120700527 in [tract 2393](#) in u band. There are coherent residuals, but without the wave-like pattern seen in [Figure 22](#), and the correlation function has significant values for both E and B-modes.

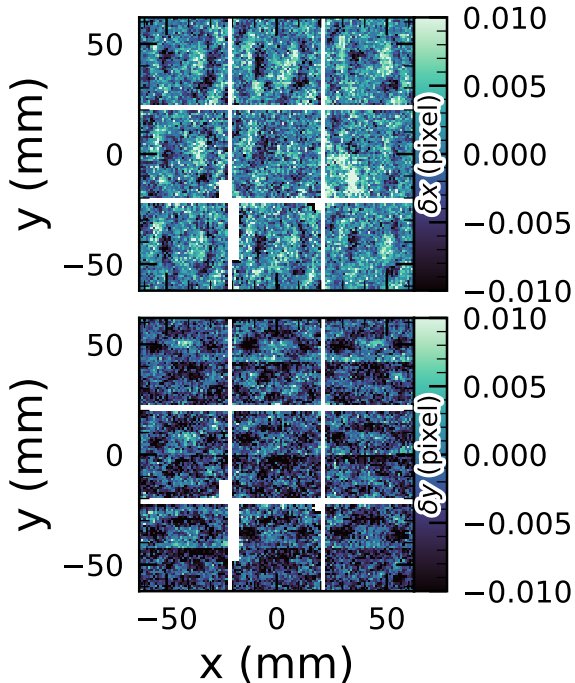


Figure 24. Median astrometric residuals as a function of focal plane position, shown in the left panel for the x direction and in the right panel for the y direction, for all nine LSSTComCam CCDs independently. The range of the color scale is ± 0.01 pixels, corresponding to 2 mas, showing that the effect is small.

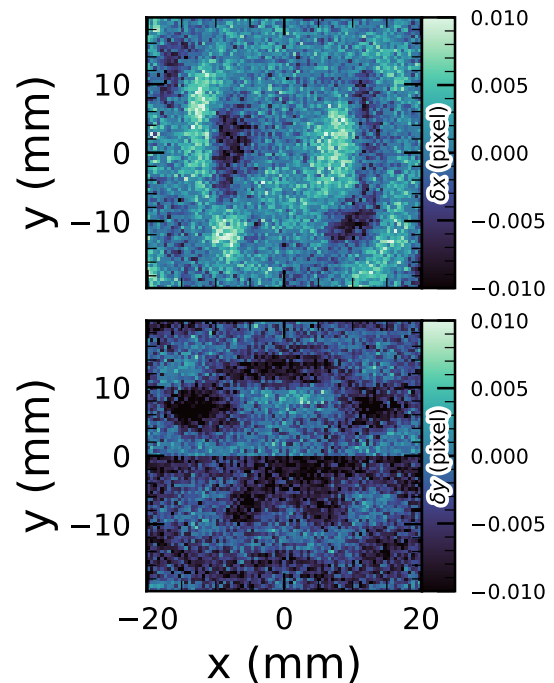


Figure 25. Median residuals as a function of pixel position, shown in the left panel for the x direction and in the right panel for the y direction. These residuals are aggregated across all nine CCDs that comprise the central LSSTComCam raft. The range of the color scale is ± 0.01 pixels, corresponding to 2 mas, showing that the effect is small.

2240 reference objects, in order of descending brightness, to
 2241 the most likely target within a $0''.5$ radius.

2242 We inject sources in 12 of the patches of the ECDFS
 2243 region with the deepest coverage. The input catalog con-
 2244 tains stars and galaxies from part of the Data Challenge
 2245 2 (DC2) simulations (LSST Dark Energy Science Col-
 2246 laboration (LSST DESC) et al. 2021), where the galaxies
 2247 consist of an exponential disk and de Vaucouleurs (G.
 2248 de Vaucouleurs 1948, 1953) bulge. To avoid deblender
 2249 failures from excessive increases in object density, stars
 2250 with a total flux (i.e., summed across all six bands)
 2251 brighter than 17.5 mag are excluded, as are galaxies
 2252 whose total flux is brighter than 15 mag or fainter than
 2253 26.5 mag. Half of the remaining objects are selected for
 2254 injection. Afterwards, individual bulge and disk com-
 2255 ponents fainter than 29 mag are also excluded, both
 2256 for computational expediency and because their struc-
 2257 tural properties are less likely to be representative of
 2258 real galaxies.

2260 Figure 29 shows completeness as a function of mag-
 2261 nitude for these injected objects in the ECDFS field.
 2262 These completeness estimates are comparable to results
 2263 from matching external catalogs. Matching to the Hub-

2264 ble Legacy Field catalog (G. Illingworth et al. 2016;
 2265 K. E. Whitaker et al. 2019) reaches 50% completeness
 2266 at $F775W = 26.13$, or about $i = 25.83$ from differences
 2267 in matched object magnitudes. Similarly, completeness
 2268 drops below 90% at $VIS = 23.80$ from matching to
 2269 Euclid Q1 (Euclid Collaboration et al. 2025) objects,
 2270 equivalent to roughly $i = 23.5$. The Euclid imaging is of
 2271 comparable or shallower depth, so magnitude limits at
 2272 lower completeness percentages than 90% are unreliable,
 2273 whereas the HST images cover too small and irregular of
 2274 an area to accurately characterize 80-90% completeness
 2275 limits.

2276 At the 80% completeness limit, nearly 20% of objects,
 2277 primarily injected galaxies, are incorrectly classified as
 2278 stars based on their reference band extendedness. Simi-
 2279 larly, the fraction of correctly classified injected stars
 2280 drops to about 50% at $i = 23.8$ (corresponding to 90%
 2281 completeness).

2282 This analysis has several caveats. The selection of
 2283 objects for matching in any catalog is not trivial. Some
 2284 fraction of the detections are spurious, particularly close
 2285 to bright stars and their diffraction spikes. Additionally,
 2286 some objects lie in masked regions of one survey but not

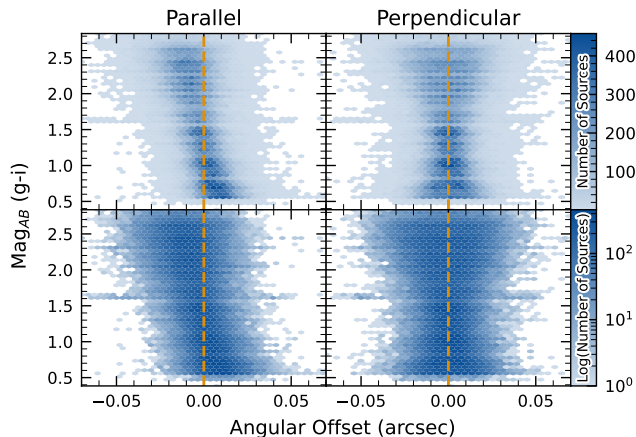


Figure 26. Visualization of [Differential Chromatic Refraction \(DCR\)](#) observed in the [LSSTComCam](#) commissioning campaign. The $g - i$ color is computed for every source in the reference catalog (§3.3.3) that is matched to a direct source in the science image, and the binned density for the full survey is plotted against the angular offset between the reference and detected positions. The angular offset is projected along coordinates parallel and perpendicular to the parallactic angle of the observation, and shows a characteristic correlation along the parallel axis with no correlation along the perpendicular axis. The orange vertical dashed line indicates the expected $g - i$ magnitude distribution at zero angular offset.

2287 another, which has not been accounted for. For injected
 2288 source matching, the reference catalog (§3.3.3) does not
 2289 include real on-sky objects. Based on prior analyses of
 2290 the [DC2](#) simulations, purity is generally greater than
 2291 completeness at any given magnitude. Similarly, for
 2292 bright ($i < 23$) objects classified as stars by reference
 2293 band extendedness, $< 5\%$ are either unmatched to a Eu-
 2294 clid or HST object, or misclassified - that is, selecting on
 2295 extendedness alone yields a fairly pure but incomplete
 2296 sample of stars. We expect to remedy some of these
 2297 shortcomings in future releases.

2298 5.7. Model Flux and Shape Measurement

2299 [Figure 30](#) shows i -band magnitude residuals for
 2300 CModel and Sérsic measurements using the matched in-
 2301 jected galaxies described in §5.6. Similar behavior is
 2302 seen in other bands. Sérsic fluxes show reduced scatter
 2303 for galaxies with $i < 22.5$, though CModel fluxes are
 2304 less biased, with median residuals closer to zero and less
 2305 magnitude-dependent. For fainter objects, Sérsic fluxes
 2306 are more biased and less accurate. The magnitude of
 2307 this bias is considerably larger than previously seen in
 2308 simulated data. Subsequent testing indicates that this
 2309 bias can be (roughly) halved by fitting an exponential
 2310 model first, and then using those parameters to initialize

2311 a free Sérsic fit. This approach will be adopted in future
 2312 releases. Aperture fluxes - including Kron and [GAaP](#) -
 2313 are not shown as they are not corrected to yield total
 2314 fluxes. The correction for Kron fluxes can be derived
 2315 from the Sérsic index ([A. W. Graham & S. P. Driver](#)
 2316 [2005](#)), but this correction is not provided in object ta-
 2317 bles.

2318 [Figure 31](#) shows $g - i$ color residuals versus r -band
 2319 magnitude for the same sample of galaxies as [Figure 30](#).
 2320 For this and most other colors, [GAaP](#) (with a $1''$ aper-
 2321 ture) and Sérsic colors both yield lower scatter; however,
 2322 the CModel colors have the smallest bias. Curiously,
 2323 the [GAaP](#) bias appears to be magnitude-dependent,
 2324 whereas the Sérsic bias remains stable from $19 < r < 26$.
 2325 Any of these color measurements are suitable for use
 2326 for deriving quantities like photometric redshifts, stellar
 2327 population parameters, etc.

2328 In addition to photometry, some algorithms include
 2329 measurements of structural parameters like size, ellip-
 2330 ticity, and Sérsic index. One particular known issue is
 2331 that many (truly) faint objects have significantly overes-
 2332 timated sizes and fluxes. This was also seen in the Dark
 2333 Energy Survey ([K. Bechtol et al. 2025](#)), who dubbed
 2334 such objects “super-spreaders”. These super-spreaders
 2335 contribute significantly to overestimated fluxes at the
 2336 faint end (see e.g. [Figure 30](#)), and are particularly prob-
 2337 lematic for the Kron algorithm ([R. G. Kron 1980](#)), which
 2338 should only be used with caution.

2339 As mentioned in §4.5, the Sérsic fits include a free
 2340 centroid, which is initialized from the fiducial centroid
 2341 of the object. Preliminary analyses of matched injected
 2342 objects suggest that the Sérsic model galaxy [astrom-](#)
 2343 [etry](#) residuals are somewhat smaller than for the stan-
 2344 dard centroids used in other measurements, and so users
 2345 of the Sérsic photometry should also use these centroid
 2346 values. One caveat is that for faint objects and/or in
 2347 crowded regions with unreliable deblending, free cen-
 2348 troids can drift significantly and potentially towards
 2349 other objects, so objects with large differences between
 2350 the fiducial and Sérsic [astrometry](#) should be discarded
 2351 or used with caution.

2352 Sérsic model parameter uncertainties are estimated
 2353 by computing and inverting the Hessian matrix with
 2354 the best-fit parameter values, after replacing the pixel
 2355 data (but not uncertainties) by the best-fit model values.
 2356 Currently, only the on-diagonal dispersion term (square
 2357 root of the variance) is provided as an error estimate for
 2358 each parameter. Future releases may provide more off-
 2359 diagonal terms of the covariance matrix - particularly
 2360 for the structural parameters, which are known to be
 2361 correlated.

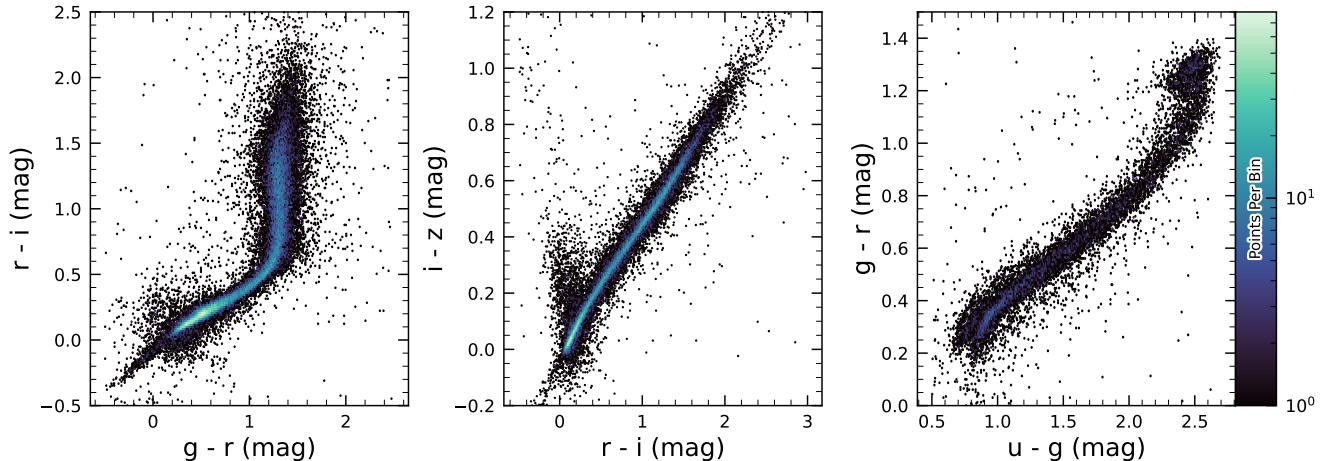


Figure 27. Examples of stellar loci for unresolved sources from the DP1 dataset. From left to right: *gri* stellar locus containing 63,236 stars with signal-to-noise ratio > 200 in the *i* band; *riz* stellar locus containing 46,760 stars with signal-to-noise ratio > 200 in the *i* band; *ugr* stellar locus containing 12,779 stars with signal-to-noise ratio > 50 in the *u* band.

2362 A major outstanding issue is that many parameter
 2363 uncertainties - including but not limited to those for
 2364 fluxes - are underestimated. This is at least partly (but
 2365 not wholly) due to the fact that coaddition introduces
 2366 covariance between pixels, which is not captured in per-
 2367 pixel variances.

2368 The degree to which uncertainties are underestimated
 2369 can depend on the parameter in question and on the
 2370 brightness of the object. In plots of uncertainty-scaled
 2371 residuals, the ideal behavior is for the median (i.e. the
 2372 bias) to lie close to zero, and for the $\pm 1\sigma$ lines to lie at
 2373 ± 1 , without any dependence on magnitude. Figure 32
 2374 shows that flux and color uncertainties for PSF model
 2375 magnitudes of injected stars are both underestimated,
 2376 but by a factor of approximately 1.7–2 that is not very
 2377 sensitive to SNR. This holds for astrometric/centroid
 2378 parameters as well.

2379 In turn, Figure 33 shows that CModel color uncertain-
 2380 ties of galaxies are underestimated by a similar factor at
 2381 the faint end, but with appreciable scaling with mag-
 2382 nitude (and thereby SNR). Flux error underestimation
 2383 is both larger than for colors and scales more strongly
 2384 with SNR. This indicates that systematic effects domi-
 2385 nate the errors in fluxes, particularly for bright galaxies.
 2386 This is also at least partly but not wholly due to so-
 2387 called model inadequacy - that is, the fact that galaxy
 2388 models, parameteric or otherwise, are insufficiently com-
 2389 plex to capture the structure of real galaxies.

2390 Figure 34 shows that Sérsic model fluxes and colors
 2391 have similar behavior as CModel, but with a greater
 2392 degree of overestimation. This may be partly due to the
 2393 fact that Sérsic parameter uncertainties are estimated
 2394 along with the free centroid and structural (shape and

2395 Sérsic index) parameters, whereas the forced CModel
 2396 fluxes and errors are derived from linear flux fits with a
 2397 fixed shape and centroid.

2398 Efforts are underway to investigate and quantify the
 2399 origin of uncertainty underestimates and future releases
 2400 will, at the least, provide recommendations for mitiga-
 2401 tions.

2402 5.8. Difference Imaging

2403 We assessed the performance of image differencing us-
 2404 ing both human vetting (§5.8.1) and source injection
 2405 (§5.8.2).

2406 5.8.1. Difference Imaging Purity

2407 Members of the DP1 team labeled more than 11,000
 2408 DIASource image triplets, each consisting of cutouts
 2409 from the science, template, and difference images. An
 2410 internal labeling service (*tasso*) was deployed within
 2411 the USDF environment. A random subset of approx-
 2412 imately 16,000 DIASources was selected and uploaded
 2413 to the service, which remained active for roughly three
 2414 months and labeled by members of the DP1 team. Users
 2415 labeled DIASource PNG images triplets, each consist-
 2416 ing of cutouts from the science, template, and differ-
 2417 ence images. Each stamp had dimensions of 51×51 pix-
 2418 els, matching the input size required by the machine-
 2419 learning model. Access to the labeling service was
 2420 granted to all individuals with commissioning data ac-
 2421 cess. Each DIASource was classified exactly once, with
 2422 a total of 35 volunteers contributing labels. Figure 35
 2423 show an example of one of the image triplets consist-
 2424 ing of cutouts from the science, template, and difference
 2425 images that volunteers were asked to label.

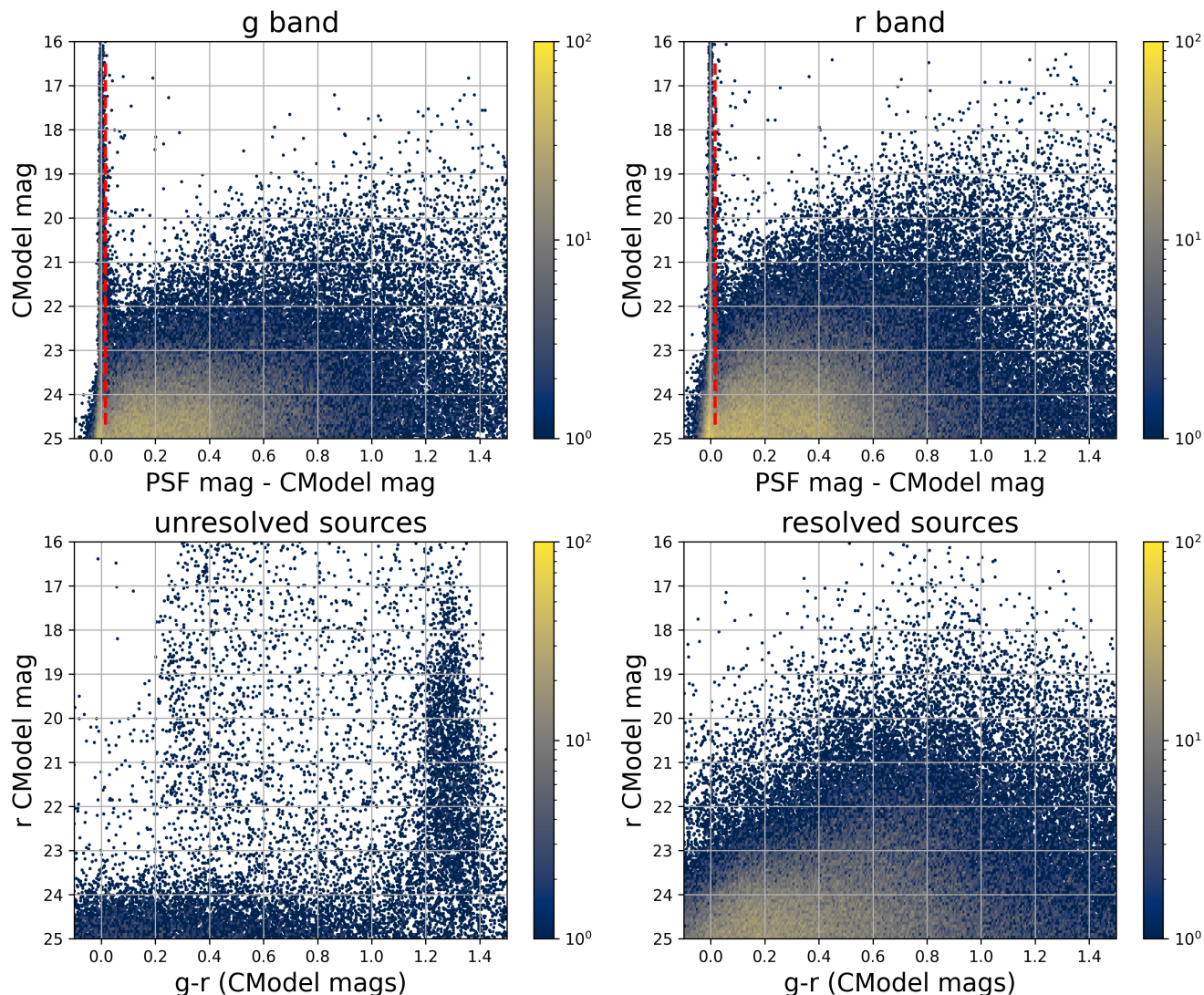


Figure 28. The top two panels shows the difference between the PSF and CModel magnitudes as a function of CModel magnitude in the g and r bands for 178,547 sources with $CModel_r < 25$ from the ECDFS field. The vertical dashed line in each panel marks the minimum value (0.016 mag) for setting the extendedness parameter to 1. The bottom two panels show the r vs. $g - r$ color-magnitude diagrams for 14,701 unresolved (left) and 163,666 resolved (right) sources. Note the unresolved sample suffers from increasing contamination by galaxies for $r > 24$.

2427 The labeled sources were classified into multiple categories representing real astrophysical events and artifacts. Prior to any filtering, the raw artifact-to-real ratio was approximately 9:1. Bright stars were identified as the dominant source of artifacts, while correlated noise, particularly in the u and g bands, also produced spurious detections near the flux threshold. We expect to be able to mitigate these effects in future LSSTCam data.

2435 Applying a reliability threshold based on the Machine Learning reliability model described in §4.6.1 improved the purity of transient detections but had limited impact on variable stars. This limitation arises from technical constraints at the time of model training, which

2440 prevented the injection of variable stars into the synthetic training set. Future reliability models for LSST-Cam data, described in §4.6.1, will be trained using a broader and more representative range of input data.

2444 The performance of the reliability model on the test data (§4.6.1) is shown in Figure 36. The rate of true positives and false negatives obtained by thresholding the reliability score at 0.5 is reported for transients (99 stamps), and variable stars (316 stamps) vetted in `tasso` in Table 6.

2448 Additionally we crossmatched stamps with Solar System Objects with known orbits retrieving 5,988 Solar System Objects stamps.

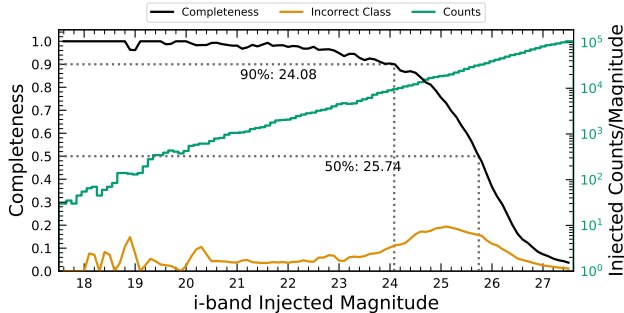


Figure 29. Completeness and incorrect classification fraction as a function of i -band CModel magnitude (Reference Magnitude) for DC2-based injected objects into a portion of the ECDFS field. The “Incorrect Class” line shows the proportion of objects that are matched but classified incorrectly by their reference-band extendedness, i.e. stars with extendedness of 1 or galaxies with extendedness of 0 in the reference band.

Table 6. The rate of true positives (TP) and false negatives (FN) obtained by thresholding the reliability score at 0.5 for Solar system objects, transients and variable stars.

Object Type	Number	TP Rate	FN Rate
Solar System	5,988	93.5%	6.5%
Transients	99	73.7%	26.3%
Variables	316	3.5%	96.5%

5.8.2. Difference Imaging Detection Completeness

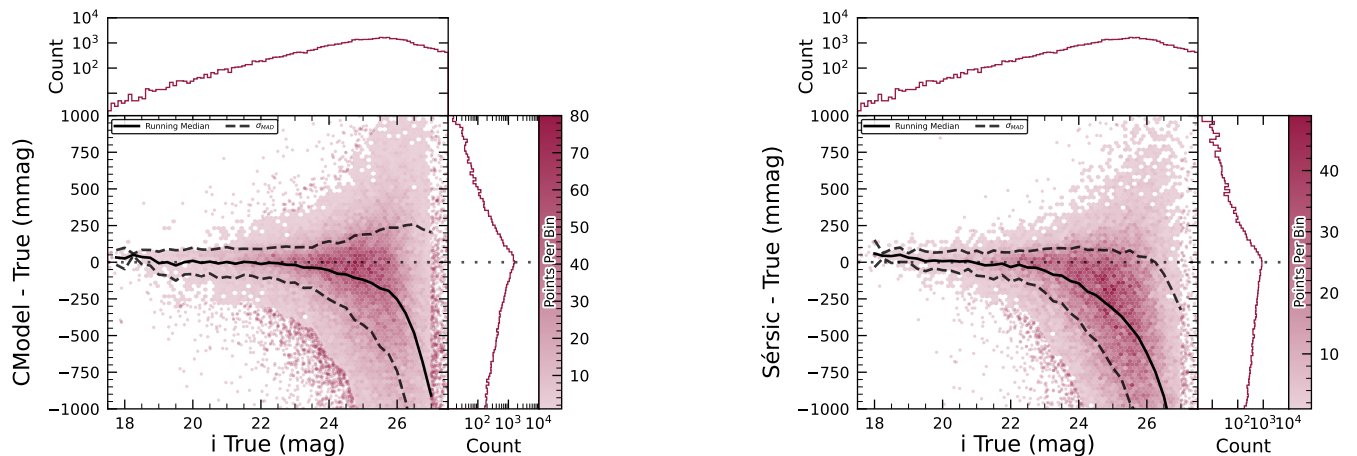
We assess the performance of our difference imaging pipeline using synthetic source injection on the science images prior to differencing. We construct a catalog of injected sources by joining two different samples of point sources, a set of hosted sources to emulate transients in galaxies and second set of hostless sources. The hosts are selected from the pipeline source catalog that is produced upstream by imposing a cut on their extendedness measurement and selecting $N_{\text{src}} = \min(100, N \times 0.05)$ of the N available sources per detector. For each host we pick a random position angle and radius using its light profile shape to decide where to place the source, and also a random value of brightness for the injected source, with magnitudes higher than the host source.

The hostless sources instead have random positions in the CCD focal plane, and magnitudes chosen from a random uniform distribution with $20 \geq m \geq m_{\text{lim}} + 1$, where m_{lim} is the limiting magnitude of the image. We

used the LSST `source_injection` package¹⁰³ to include these sources in our test images. We performed a coordinate cross-match task, with a threshold of $0''.5$ to find which of these sources were detected and which were lost, enabling the calculation of a set of performance metrics.

In Figure 37 we show the detection completeness as a function of the SNR, for sources in the ECDFS field, for filters *griz*. We observe a completeness $> 95\%$ for sources with $\text{SNR} > 6$, with mean completeness $\simeq 99\%$ and standard deviation of $\simeq 0.7\%$. In Figure 38 we show the distribution of the residuals of the recovered sky coordinates for the detected synthetic sources. The marginal distributions are both centered at zero, and for sources of $\text{SNR} > 20$ the residuals are compatible with normal distributions $\mathcal{N}(\mu = 0, \sigma^2 = (0''.02)^2)$. In Figure 39 we show photometry results for our detected synthetic sources in the i filter, using PSF photometry on the difference images. We include both the magnitude residuals as well as the flux pulls, defined as $(f_{\text{PSF}} - f_{\text{True}})/\sigma_{f_{\text{PSF}}}$, where f_{True} is the true flux, f_{PSF} is the PSF flux and $\sigma_{f_{\text{PSF}}}$ is its uncertainty, as a function of the true magnitude of the synthetic sources, including the running median and median absolute deviation (MAD) for the whole brightness range. We also include the true magnitude distribution as well as the detection completeness on the top panel, and for reference the 90% and 50% completeness magnitude values in vertical lines. On the right panels we include the marginal distribution for sources brighter than 22.5 mag, splitting the data into hosted and hostless, as well as the robust mean and standard deviation. From this figure we can see that our flux measurements are accurate within a wide range of magnitudes, for both hosted and hostless synthetic sources. We find that the median offset is below 0.002 mag for true magnitudes below 21, and with a maximum σ_{MAD} scatter of about 0.02 mag in this range. For true $m_i < 22.5$, the robust running median PSF magnitudes residuals are < 0.02 mag, and when splitting into hosted and hostless both robust median are well below 0.01, and robust σ , i.e. σ_{MAD} are also well below 0.05. For all sources with $m_i < 21.5$ the running median is always $|\langle \delta \rangle| < 0.1$, and $\text{MAD } \sigma_\delta < 1$. Extending to sources with $m_i < 22.5$ then hostless sources have a robust mean pull below 0.02, with a robust standard deviation < 1.15 , while these parameters increase to 0.2 and 1.2 for hosted sources, suggesting that we might

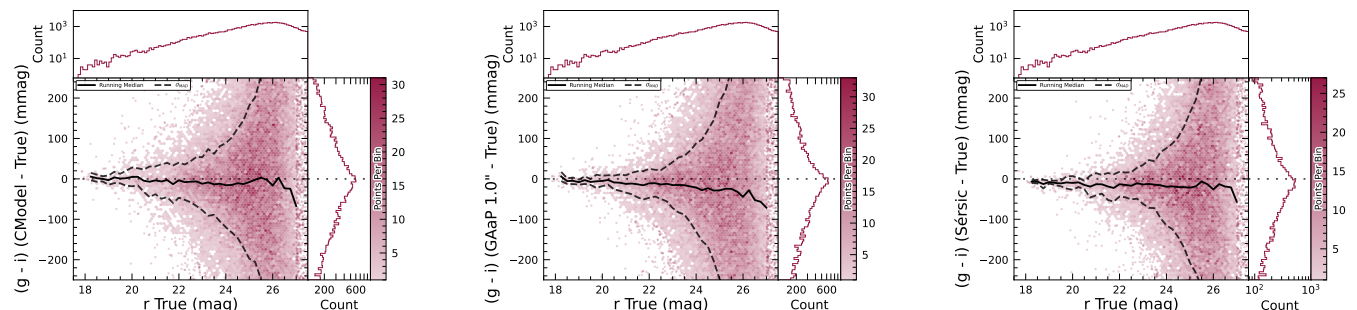
¹⁰³ <https://pipelines.lsst.io/modules/lstt.source.injection/index.html>



(a) i -band magnitude residuals for CModel measurements of injected galaxies.

(b) i -band magnitude residuals for Sérsic model measurements of injected galaxies.

Figure 30. i -band magnitude residuals for matched injected DC2 galaxies with the CModel and Sérsic algorithms in a portion of the ECDFS region, including the median and scatter thereof. The black line is the median.



(a) $g-i$ color residuals for CModel measurements of injected galaxies.

(b) $g-i$ color residuals for GAaP measurements of injected galaxies.

(c) $g-i$ color residuals for Sérsic model measurements of injected galaxies.

Figure 31. $g-i$ color residuals versus true r -band magnitude for matched injected DC2 galaxies with the CModel, GAaP and Sérsic algorithms in a portion of the ECDFS region.

2522 have contamination from host background sources po- 2540
 2528 tentially biasing our fluxes. 2541

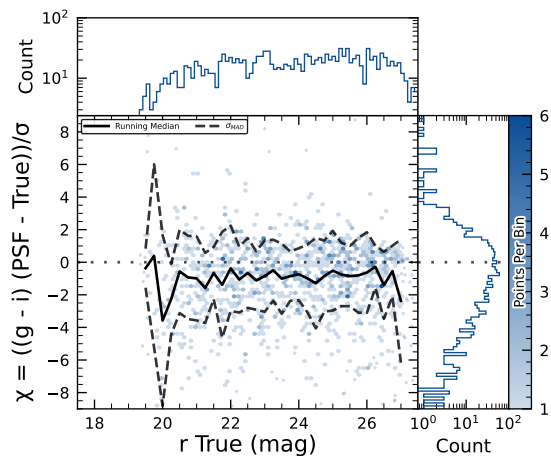
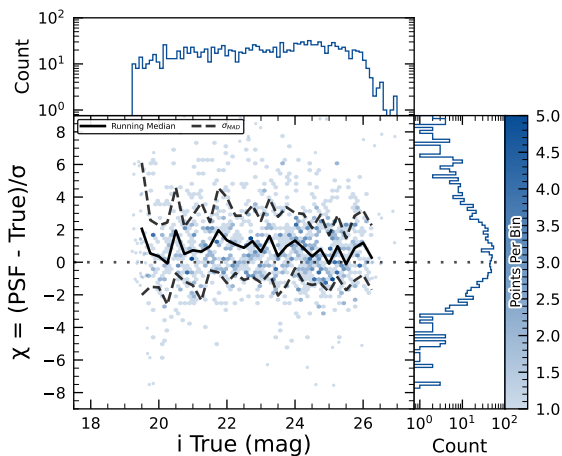
2525 5.9. Solar System

2526 5.9.1. Asteroid Linking Performance

2527 The evaluation of asteroid linking performance in DP1
 2528 focused on demonstrating discovery capability. The solar
 2529 system discovery pipeline produced 269,581 track-
 2530 lets, 5,691 linkages, and 281 post-processed candidates.

2531 As described in §4.6.3, post-processing of the heli-
 2532 olinc output with link_purify produced a final set of
 2533 281 candidate linkages, ranked with the most promising
 2534 first. We then used find_orb (B. Gray 2025) to derive
 2535 orbit fits for each candidate, sorting the resulting list by
 2536 χ^2_{dof} , a measure of fit quality. A conservative manual
 2537 investigation of these candidates yielded a curated
 2538 list of 93 probable new asteroid discoveries. Manual
 2539 inspection of the linkages indicated that those ranked

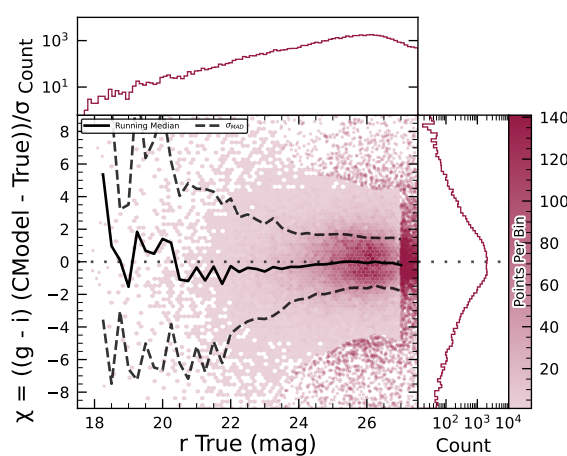
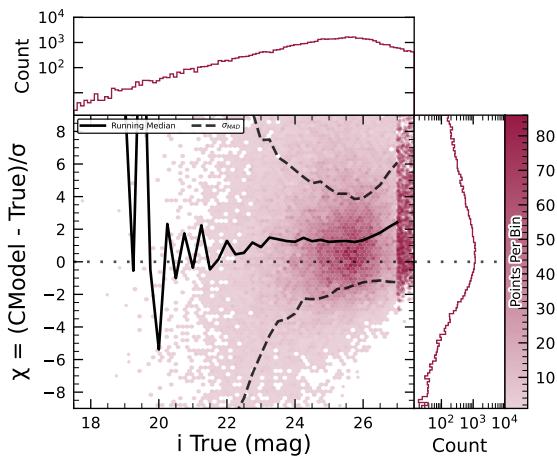
2540 0–137 corresponded to unique real asteroids; ranks 138–
 2541 200 contained additional real objects intermixed with
 2542 some spurious linkages; and ranks higher than 200 were
 2543 essentially all spurious. This analysis indicates that it
 2544 will be possible to identify cuts on quality metrics such
 2545 as χ^2 to define discovery candidate samples with high
 2546 purity; determining the exact quantitative cut values re-
 2547 quires more data with LSSTCam. We next removed all
 2548 observations matched to known asteroids (using Minor
 2549 Planet Center (MPC)’s MPCChecker service), reducing
 2550 the number of candidates to 97. Of these, four had
 2551 strong astrometric and/or photometric outliers, likely
 2552 due to self-subtraction in difference images due to the
 2553 unavoidable limitations of template generation from the
 2554 limited quantity of data available from LSSTComCam.
 2555 We suspect these four linkages do correspond to real ob-
 2556 jects, but have chosen to discard them out of an abun-
 2557 dance of caution. The remaining 93 were submitted to



(a) *i*-band flux uncertainty-scaled residuals for PSF model measurements of injected stars.

(b) *g* - *i* color uncertainty-scaled residuals for PSF model measurements of injected stars.

Figure 32. Color and flux uncertainty-scaled residuals for matched injected DC2 stars' PSF model measurements in a portion of the ECDFS region.



(a) *i*-band flux uncertainty-scaled residuals for CModel measurements of injected galaxies.

(b) *g* - *i* color uncertainty-scaled residuals for CModel measurements of injected galaxies.

Figure 33. Color and flux uncertainty-scaled residuals for matched injected DC2 galaxies' CModel measurements in a portion of the ECDFS region.

2558 the Minor Planet Center and accepted as discoveries,
 2559 demonstrating the LSST pipelines are able to success-
 2560 fully discover new solar system objects.

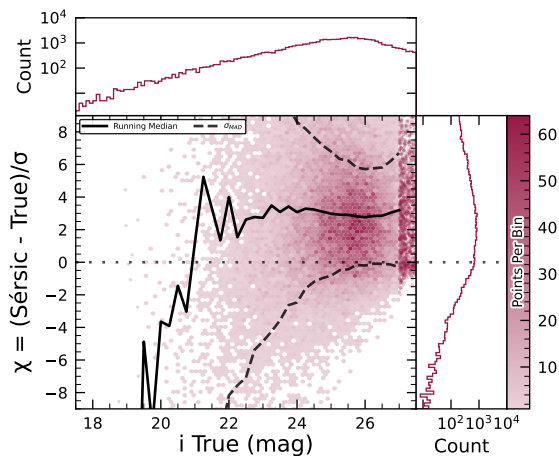
2561 **5.9.2. Asteroid Association Performance**

2562 During the Solar System association step, 5988 Di-
 2563 aSources were linked to 431 unique Solar System ob-
 2564 jects, These include 3,934 DiaSources with 338 pre-
 2565 viously known objects cataloged by the MPC, and 2,054
 2566 DiaSources with the 93 newly-discovered objects, all of
 2567 which are main belt asteroids. An additional 143 de-
 2568 tectations of these newly discovered objects were also re-
 2569 covered. These detections were not initially identified
 2570 by the discovery pipelines, as they did not meet the

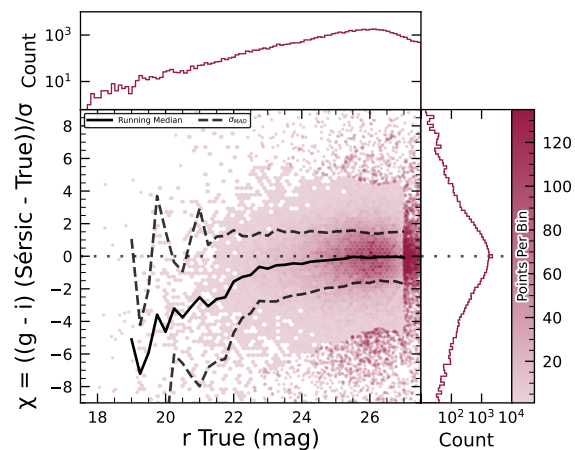
2571 required criteria for tracklet formation, specifically the
 2572 minimum number of detections and/or the maximum
 2573 allowed time span between observations.

2574 The astrometric residuals of known asteroid associa-
 2575 tions are shown in Figure 40. The astrometric precision
 2576 for solar system sources is excellent, with the majority of
 2577 objects detected within 0".1 of their expected positions.

2578 By analyzing the signed median residuals to search for
 2579 biases, we find that previously-known objects have mean
 2580 residuals of 0".001 and -0".016 in the RA and Dec di-
 2581 rections respectively, whereas newly-discovered objects
 2582 have mean residuals of -0".035 and -0".010 in the RA
 2583 and Dec directions, respectively. These mean residuals
 2584 are small enough to eliminate the possibility of a tim-



(a) i -band flux uncertainty-scaled residuals for Sérsic model measurements of injected galaxies.



(b) $g-i$ color uncertainty-scaled residuals for Sérsic model measurements of injected galaxies.

Figure 34. Color and flux uncertainty-scaled residuals for matched injected DC2 galaxies’ Sérsic measurements in a portion of the ECDFS region.

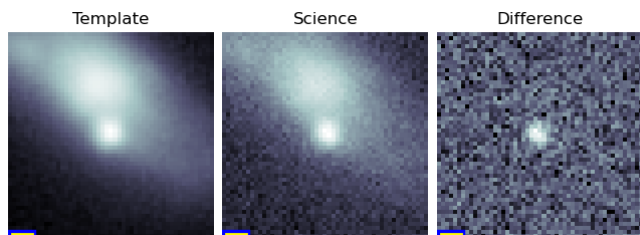


Figure 35. An example an image triplet consisting of cutouts showing, from left to right, the template, science, and difference images that volunteers were asked to label.

2585 ing offset greater than the second-scale shutter motion,
 2586 which is consistent with the timing studies presented in
 2587 §2.2.2.

2588 The wider scatter in the RA residuals is due to ob-
 2589 jects whose measured orbital elements are less well con-
 2590 strained, translating to larger along-track positional er-
 2591 rors in the predicted positions. Observations of objects
 2592 with large residuals are the most valuable ones from the
 2593 point of view of improving the orbit, which is why we
 2594 kept a generous matching radius. However, in future re-
 2595 leases we are likely to couple this with either orbit fit-
 2596 ting to verify the “singleton” match, or require two near-in-
 2597 time observations (a tracklet) that match the expected
 2598 motion vector as well.

2599 Optimal moving source attribution is an area of ac-
 2600 tive work that we expect to fully converge in time of
 2601 Data Release 1 (DR1). In the meantime, for DP1 we’ve
 2602 opted to start with simple, more easily understandable,
 2603 criteria.

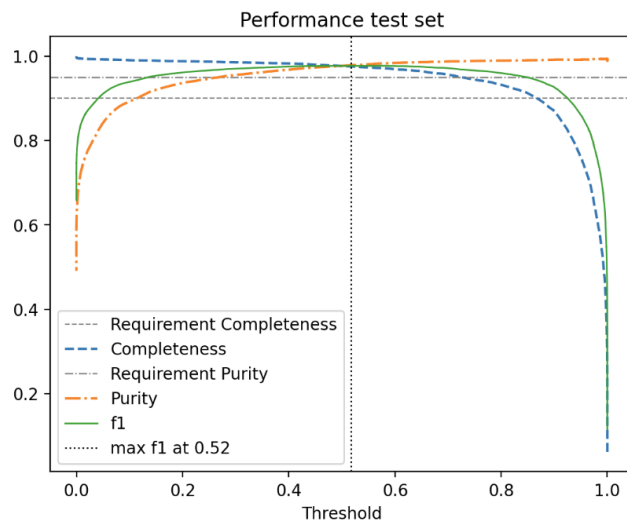


Figure 36. The purity and completeness of the reliability score is shown as a function of reliability threshold based on the testing data. A vertical line marks the threshold where the highest F1-score is obtained. The F1 score is the harmonic mean of completeness and purity. See §4.6.1 for details on the model and model training.

5.10. Crowded Fields

2604
 2605 Among the seven Rubin DP1 target fields, two stand
 2606 out for their severe stellar crowding: the globular cluster
 2607 47 Tucanae (47_Tuc) and the Fornax dwarf spheroidal
 2608 galaxy (Fornax dSph). These fields were selected in part
 2609 to stress-test the LSST Science Pipelines under high-
 2610 density conditions. While both exhibit high stellar den-
 2611 sities, the nature and spatial extent of the crowding dif-
 2612 fer significantly.

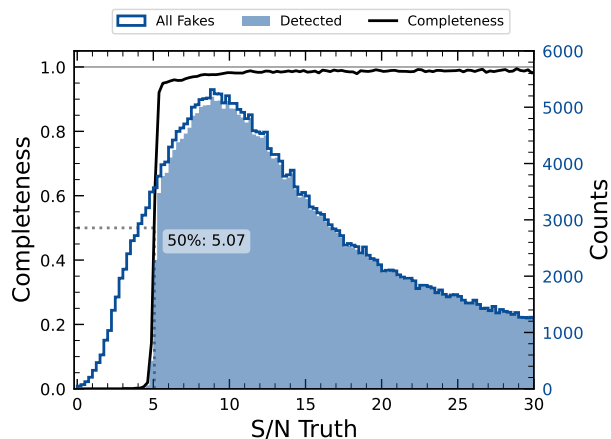


Figure 37. The difference image detection completeness for injected sources in the ECDFS field, for filters *griz*, as a function of the estimated signal to noise ratio SNR. This completeness is the ratio between the found fake sources (shaded histogram) and all the sources (solid line). The horizontal dashed line represents where the 50% completeness level is reached, at approximately $\text{SNR} \simeq 5.07$.

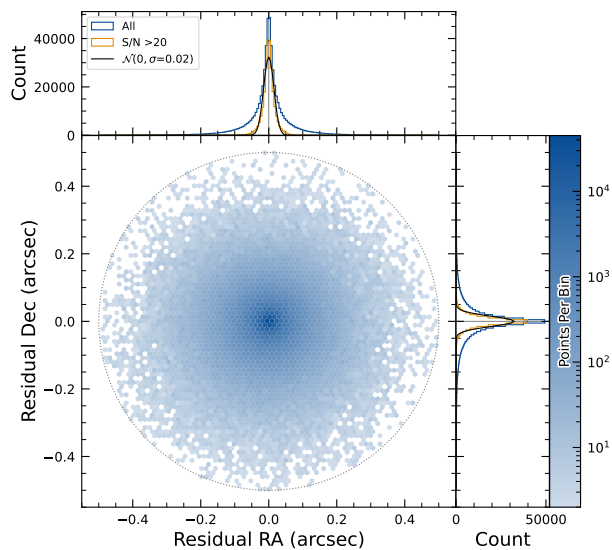


Figure 38. Coordinate residuals for detected synthetic sources in difference images, between recovered and true position of the sources in the ECDFS field. In the top and right panels we include the distribution of these offsets, for all sources as well as for sources with $\text{SNR} > 20$. These high SNR sources show gaussian coordinate residual distributions with $\sigma = 0''.02$ (black solid lines). The circle reflects the matching radius of $0''.5$.

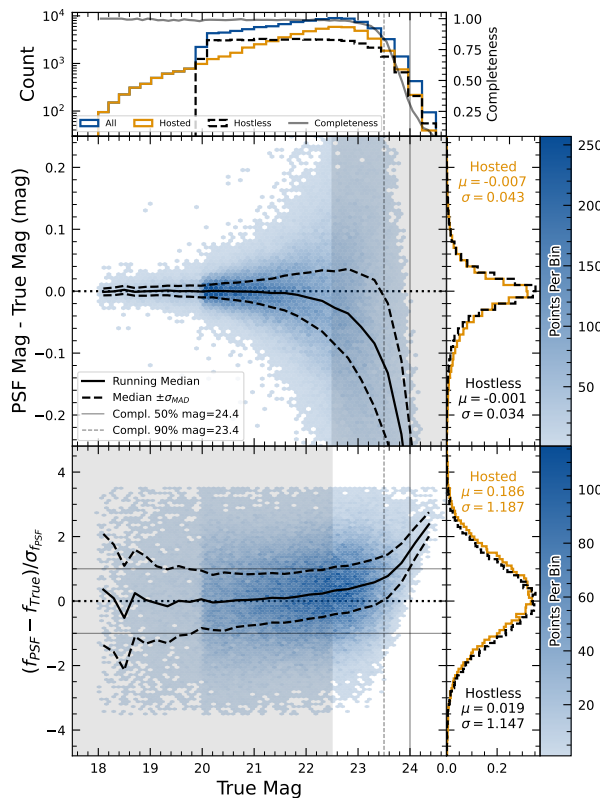


Figure 39. Magnitude residuals and flux pulls for *i*-band PSF photometry on difference images for ECDFS field in *i* for detected injected sources. Top panel: Distribution of true magnitudes for injected sources (blue), and split into hostless (black dash) and hosted (orange) sources, with detection completeness as a function of true magnitude (gray line). Vertical dashed lines indicate the 90% and 50% completeness magnitude limits. Center left panel: 2D hexbin plot of PSF magnitude residuals (measured minus true) versus true magnitude for detected sources, with running median (solid black) and σ_{MAD} (dashed black) overlaid. Center right panel: Marginalized distributions of PSF magnitude residuals for hostless (blue) and hosted (orange) sources with true magnitude $m_i < 22.5$, annotated with robust mean and standard deviation. Bottom left panel: 2D hexbin plot of PSF flux pulls versus true magnitude for detected sources, with running median (solid black) and σ_{MAD} (dashed black) overlaid. Bottom right panel: Marginalized distributions of PSF flux pulls for hostless (blue) and hosted (orange) sources with true magnitude $m_i < 22.5$, annotated with robust mean and standard deviation.

2613 47 Tuc presents extreme crowding across much of the
 2614 field, encompassing its dense core and the eastern re-

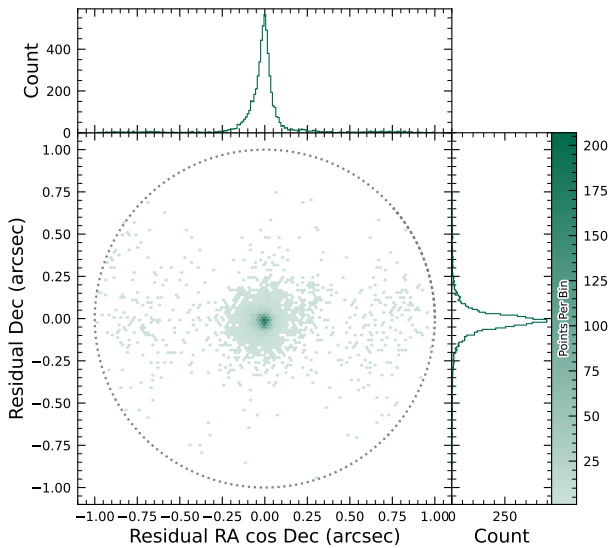


Figure 40. Astrometric residuals between expected and observed positions of Solar System Objects in DP1. The median residuals are $0''.001$ and $-0''.016$ in R.A./Dec direction, with standard deviations of $0''.19$ and $0''.10$, respectively. No detectable systematic offset from zero indicates there are no major errors in either timing or astrometry delivered by the Rubin system. The wider scatter in the RA direction is due to objects whose measured orbital elements are less well constrained, translating to larger along-track positional errors in the predicted positions.

gions influenced by the Small Magellanic Cloud (SMC). This pervasive crowding leads to persistent challenges for deblending and reliable source detection, exposing field-wide limitations in the current pipeline performance (Y. Choi et al. 2025). In contrast, Fornax dSph shows significant crowding only in its central region, with outer areas remaining well resolved and easier to process.

In both 47 Tuc and Fornax, extreme crowding led to the deblending step being skipped frequently when memory or runtime limits were exceeded, typically due to an excessive number of peaks, or large parent footprints. However, the impact of these limitations differed: in 47 Tuc, deblending was often skipped across the entire field, resulting in large gaps and substantially reduced completeness. In Fornax, these issues were largely confined to the central region, with much better recovery in the outskirts. This contrast highlights how the pipeline’s limitations depend on the spatial extent of high-density regions: 47 Tuc exposed systematic, field-wide challenges, whereas Fornax revealed more localized, density-driven limits.

T. M. Wainer et al. (2025) explored the Rubin DP1 DiaObject catalog (§3.2) in the 47 Tuc field, which contains sources detected in difference images. Because forced photometry is performed at these positions across all single-epoch images, this dataset bypasses the coadd-based detection and deblending stages that often fail in crowded regions. By computing the median of the forced photometry for each DiaObject across available visits, they recovered approximately three times more candidate cluster members than found in the standard Object table (Y. Choi et al. 2025). This result underscores the value of difference-imaging-based catalogs for probing dense stellar regions inaccessible to standard coadd processing in DP1.

Although the DP1 pipeline was not optimized for crowded-field photometry, these early studies of 47 Tuc and Fornax provide critical benchmarks. They highlight both the limitations and opportunities for science with Rubin data in crowded environments, and they inform future pipeline development aimed at robust source recovery in complex stellar fields.

6. RUBIN SCIENCE PLATFORM

The RSP (M. Jurić et al. 2019) is a powerful, cloud-based environment for scientific research and analysis of petascale-scale astronomical survey data. It serves as the primary interface for scientists to access, visualize, and conduct next-to-the-data analysis of Rubin and LSST data. The RSP is designed around a “bring the compute to the data” principle, eliminating the need for users to download massive datasets. Although DP1 is much smaller in size (3.5 TB) than many current survey datasets, future LSST datasets will be far larger and more complex, making it crucial to co-locate data and analysis for effective scientific discovery.

The RSP provides users with access to data and services through three distinct user-facing Aspects: a Portal, which facilitates interactive exploration of the data; a JupyterLab-based Notebook environment for data analysis using Python; and an extensive set of Application Programming Interfaces (APIs) that enable programmatic access to both data and services. The three Aspects are designed to be fully integrated, enabling seamless workflows across the RSP. The data products described in §3 are accessible via all three Aspects, and the system facilitates operations such as starting a query in one Aspect and retrieving its results in another. Figure 41 shows the Rubin Science Platform landing page in the Google cloud.

The RSP is supported by a number of back-end services, including databases, files, and batch comput-

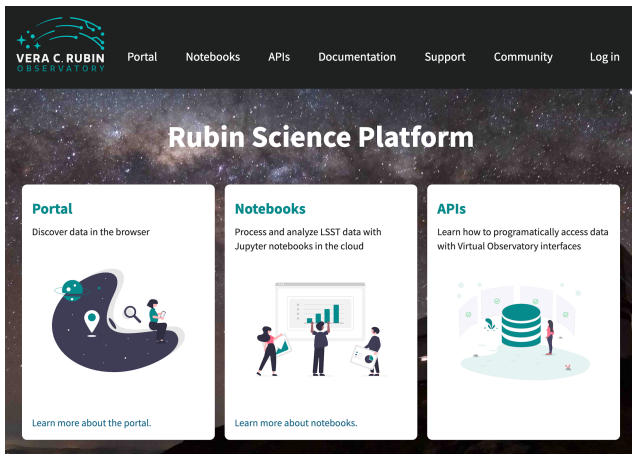


Figure 41. The Rubin Science Platform landing page at <https://data.lsst.cloud/> showing the three user-facing Aspects as well as links to documentation and support information.

ing. Support for collaborative work through shared workspaces is also included in the RSP.

A preview of the RSP was launched on Google Cloud in 2022, operating under a shared-risk model to support Data Preview 0 (W. O’Mullane et al. 2024a). This allowed the community to test the platform, begin preparations for science, and provide valuable feedback to inform ongoing development. It was the first time an astronomical research environment was hosted in a cloud environment. The DP1 release brings major updates to RSP services, enhancing scientific analysis capabilities. The RSP remains under active development, with incremental improvements being rolled out as they mature. During the Rubin Early Science Phase, the RSP will continue to operate under a shared-risk model. This section outlines the RSP functionality available at the time of the DP1 release and provides an overview of planned future capabilities.

6.1. Rubin Data Access Center

The Rubin US Data Access Center (US DAC) utilizes a novel hybrid on-premises-cloud architecture, which combines on-premises infrastructure at the USDF at SLAC with flexible and scalable resources in the Google cloud. This architecture has been deployed and tested using the larger simulated data set of DP0.2 (W. O’Mullane et al. 2024b).

In this hybrid model, user-facing services are deployed in the cloud to support dynamic scaling in response to user demand and to simplify the provisioning and management of large numbers of science user accounts. The majority of the static data products described in §3 are stored on-premises at the USDF to benefit from cost-effective mass storage and close integration with Ru-

bin data processing infrastructure, also located at the USDF. For imaging data, the Data Butler (§6.2.2) provides the interface between the cloud-based users and data services, and the on-premises data. For catalog data, a cloud-based TAP client (§6.2.1) submits queries to the on-premises Qserv database cluster (§6.5) and retrieves the results. In the initial DP1 deployment, catalog data is hosted at the USDF while image data is stored in the cloud. The full hybrid model will be rolled out and further tested following the release of DP1. The RSP features a single-sign-on authentication and authorization system to provide secure access for Rubin data rights holders (R. Blum & the Rubin Operations Team 2020).

6.2. API Aspect

The API Aspect provides a comprehensive set of user-facing interfaces for programmatic access to the DP1 data products, through both IVOA-compliant services and the Rubin Data Butler. IVOA services enable standard queries and integration with existing tools, while the Butler facilitates advanced data processing within the LSST Science Pipelines.

At the time of the DP1 release, some IVOA services are unavailable, and certain data products are only accessible via the Butler. This section provides an overview of the available IVOA services and Butler access.

6.2.1. IVOA Services

Rubin has adopted a Virtual Observatory (VO)-first design philosophy, prioritizing compliance with IVOA standard interfaces to foster interoperability, standardization, and collaboration. In cases where standardized protocols have yet to be established, additional services have been introduced to complement these efforts. This approach ensures that the RSP can be seamlessly integrated with community-standard tools such as Tool for Operations on Catalogues And Tables (TOPCAT) (M. Taylor 2011) and Aladin (F. Bonnarel et al. 2000; T. Boch & P. Fernique 2014; M. Baumann et al. 2022), as well as libraries such as PyVO (M. Graham et al. 2014).

The user-facing APIs are also used internally within the RSP, creating a unified design that ensures consistent and reproducible workflows across all three Aspects. This reduces code duplication, simplifies maintenance, and ensures all users, both internal and external, access data in the same way. For example, an Astronomical Data Query Language (IVOA standard) (ADQL) query on the Object catalog via TAP yields identical results whether run from the Portal, Notebook, or an external client.

The following [IVOA](#) services are available at the time of the [DP1](#) release:

- **Table Access Protocol (TAP) Service:** A TAP service ([P. Dowler et al. 2019](#)) enables queries of catalog data via the IVOA-standard [ADQL](#), a dialect of SQL92 with spherical geometry extensions. The main TAP service for [DP1](#) runs on the Rubin-developed [Qserv](#) database (§ 6.5), which hosts the core science tables described in §3.2, as well as the Visit database. It also provides image metadata in the IVOA [ObsCore](#) format via the standard `ivoa.ObsCore` table, making it an “ObsTAP” service (ObsTAP; [M. Louys et al. 2017](#)). The TAP service is based on the [Canadian Astronomy Data Centre \(CADC\)](#)’s open-source Java TAP implementation¹⁰⁴, modified for the exact query language accepted by Qserv. It currently supports a large subset of ADQL, with limitations documented in the data release materials (see §7.1) and exposed via the TAP **capabilities** endpoint where possible.

The TAP service provides metadata annotations consistent with the standard, including table and column descriptions, indications of foreign-key relationships between tables, and column metadata such as units and [IVOA Unified Content Descriptors \(UCDs\)](#).

- **Image Access Services:** Rubin image access services are compliant with [IVOA SIAv2](#) (Simple Image Access Protocol, version 2; [T. Jenness et al. 2024](#); [P. Dowler et al. 2015](#)) for discovering and accessing astronomical images based on [metadata](#). SIAv2 is a [REpresentational State Transfer \(REST\)](#)-based protocol designed for the discovery and retrieval of image data. It allows, for instance, querying all images in a given band over a defined sky region and time period.

Users identify an image or observation of interest and query the service. The result set includes [metadata](#) about the image, such as the sky position, time, or band, and a data access URL, which includes an IVOA Identifier uniquely identifying the dataset ([T. Jenness & G. P. Dubois-Felsmann 2025](#)), allowing the dataset to be retrieved or a cutout requested via [Server-side Operations for Data Access \(IVOA standard\) \(SODA\)](#).

- **Image Cutout Service:** The Rubin Cutout Service ([R. Allbery 2023, 2024](#)) is based on the IVOA [SODA](#) standard ([F. Bonnarel et al. 2017](#)). Users submit requests specifying sky coordinates and the cutout size as the radius from the coordinates, and the service performs the operation on the full image and returns a result set. For [DP1](#), the cutout service is a single cutout service only where N cutout requests will require N independent synchronous calls. We expect some form of bulk cutout service by mid 2026.

- **HiPS Data Service:** An authenticated [HiPS](#) ([P. Fernique et al. 2017](#)) data service for seamless pan-and-zoom access to large-scale co-adds. It supports fast interactive progressive image exploration at a range of resolutions.

- **WebDAV:** A [Web Distributed Authoring and Versioning \(WebDav\)](#) service is provided to enable users to remotely manage, edit, and organize files and directories on the [RSP](#) as if they were local files on their own computer. This is especially useful for local development.

6.2.2. Data Butler

The Rubin Data Butler ([T. Jenness et al. 2022](#); [N. B. Lust et al. 2023](#)), is a high-level interface designed to facilitate seamless access to data for both users and software systems. This includes managing storage formats, physical locations, data staging, and database mappings. A [Butler](#) repository contains two components:

- the *Data Store*: A physical storage system for datasets, e.g., a [Portable Operating System Interface \(POSIX\)](#) file system or S3 object store; and
- the *Registry*: An [Structured Query Language \(SQL\)](#)-compatible database that stores metadata about the datasets in the data store.

For [DP1](#), the Butler repository is hosted in the Google Cloud, using an ([Amazon](#)) [Simple Storage Service \(S3\)](#)-compatible store for datasets and AlloyDB, a PostgreSQL-compatible database, for the registry.

In the context of the [Butler](#), a *dataset* refers to a unique data product, such as an image, catalog or map, generated by the observatory or processing pipelines. Datasets belong to one of the various types of data products, described in §3. The [Butler](#) ensures that each dataset is uniquely identifiable by a combination of three pieces of information: a data coordinate, a dataset type, and a run collection. For example,

¹⁰⁴ <https://github.com/opencadc/tap>

Table 7. Tract coverage of each DP1 field. The size of a tract is larger than the LSSTComCam field of view; however, since each observed field extends across more than one tract, each field covers multiple tracts.

Field Code	Tract ID
47_Tuc	453, 454
ECDFS	4848, 4849, 5062, 5063, 5064
EDFS_comcam	2234, 2235, 2393, 2394
Fornax_dSph	4016, 4017, 4217, 4218
Rubin_SV_095_-25	5305, 5306, 5525, 5526
Rubin_SV_38_7	10221, 10222, 10463, 10464, 10704, 10705
Seagull	7610, 7611, 7849, 7850

a dataset that represents a single raw image in the *i* band taken on the night starting 2024-11-11 with exposure ID 2024111100074 would be represented as `dataId='exposure':2024111100074, 'band':'i', 'instrument':'LSSTComCam'` and is associated with the `raw` DatasetType. For a deep coadd on a patch of sky in the Seagull field, there would be no exposure dimensions and instead the tract, patch and band would be specified as `dataId='tract':7850, 'patch':6, 'band':'g', 'instrument':'LSSTComCam', skymap='lsst_cells_v1'` and is associated with the `deep_coadd` DatasetType. The tract identification numbers and corresponding target names for these tracts are listed in Table 7.

The data coordinate is used to locate a dataset in multi-dimensional space, where dimensions are defined in terms of scientifically meaningful concepts, such as instrument, visit, detector or band. For example, a calibrated single-visit image (§3.1) has dimensions including band, instrument, and detector. In contrast, the visit table (§3.2), a catalog of all calibrated single-epoch visits in DP1, has only the instrument dimension. The main dimensions used in DP1 are listed, together with a brief description, in Table 8. To determine which dimensions are relevant for a specific dataset, the Butler defines dataset types, which associate each dataset with its specific set of relevant dimensions, as well as the associated Python type representing the dataset. The dataset type defines the kind of data a dataset represents, such as a raw image (`raw`), a processed catalog (`object_forced_source`), or a sky map (`skyMap`). Table 9 lists all the dataset types available via the Butler in DP1, together with the dimensions needed to uniquely identify a specific dataset and the number of unique datasets of each type.

It is important to highlight a key difference between accessing catalog data via the TAP service versus the Butler. While the TAP service contains entire catalogs, many of the same catalogs in the Butler are split into multiple separate catalogs. This is partly due to how these catalogs are generated, but also because of the way data is stored within and retrieved from the Butler repository – it is inefficient to retrieve the entire Source catalog, for example, from the file system. Instead, because the Source catalog contains data for sources detected in the `visit_images`, there is one Source catalog in the Butler for each `visit_image`. Similarly, there is one Object catalog for each `deep_coadd`. All the catalogs described in §3.2, aside from the `CcdVisit`, `SSObject`, `SSSource`, and `Calibration` catalogs, are split within the Butler.

A dataset is associated with one or more *Collections*; logical groupings of datasets within the Butler system that were created or processed together by the same batch operation. Collections allow multiple datasets with the same data coordinate to coexist without conflict. Collections support flexible, parallel processing by enabling repeated analyses of the same input data using different configurations. The DP1 Butler is read-only; a writable Butler is expected by mid-2026.

6.2.3. Remote Programmatic Access

The Rubin RSP API can be accessed from a local system by data rights holders outside of the RSP, by creating a user security token. This token can then be used as a bearer token for API calls to the RSP TAP service. This capability is especially useful for remote data analysis using tools such as TOPCAT, as well as enabling third-party systems, e.g., Community Alert Brokers, to access Rubin data. Additionally, it supports remote development, allowing for more flexible workflows and integration with external systems.

6.3. Portal Aspect

The Portal Aspect provides an interactive web-based environment for exploratory data discovery, filtering, querying, and visualization of both image and catalog data, without requiring programming expertise. It enables users to access and analyze large datasets via tools for catalog queries, image browsing, time-series inspection, and cross-matching.

The Portal is built on Firefly (X. Wu et al. 2019), a web application framework developed by the Infrared Processing and Analysis Center (IPAC). Firefly provides interactive capabilities such as customizable table views, image overlays, multi-panel visualizations, and synchronized displays linking catalog and image data.

Table 8. Descriptions of and valid values for the key data dimensions in DP1. YYYYMMDD signifies date and # signifies a single 0–9 digit.

Dimension	Format/Valid values	Description
day_obs	YYYYMMDD	A day and night of observations that rolls over during daylight hours.
visit	YYYYMMDD#####	A sequence of observations processed together; synonymous with “exposure” in DP1.
exposure	YYYYMMDD#####	A single exposure of all nine ComCam detectors.
instrument	LSSTComCam	The instrument name.
detector	0–8	A ComCam detector.
skymap	lsst_cells_v1	A set of tracts and patches that subdivide the sky into rectangular regions with simple projections and intentional overlaps.
tract	See Table 7	A large rectangular region of the sky.
patch	0–99	A rectangular region within a tract.
physical_filter	u_02, g_01, i_06, r_03, z_03, y_04	A physical filter.
band	u, g, r, i, z, y	An conceptual astronomical passband.

Table 9. The name and number of each type of data product in the Butler and the dimensions required to identify a specific dataset.

Data Product	Name in Butler	Required Dimensions	Number in DP1
Image Data Products			
raw	raw	instrument, detector, exposure	16125
visit_image	visit_image	instrument, detector, visit	15972
deep_coadd	deep_coadd	band, skymap, tract, patch	2644
template_coadd	template_coadd	band, skymap, tract, patch	2730
difference_image	difference_image	instrument, detector, visit	15972
Catalog Data Products			
Source	source	instrument, visit	1786
Object	object	skymap, tract	29
ForcedSource	object_forced_source	skymap, tract, patch	636
DiaSource	dia_source	skymap, tract	25
DiaObject	dia_object	skymap, tract	25
ForcedSourceOnDiaObject	dia_object_forced_source	skymap, tract, patch	597
SSSource	ss_source	–	1
SSObject	ss_object	–	1
Visit	visit_table	instrument	1
CCDVisit	visit_detector_table	instrument	1

2951 Designed to support both exploratory data access and
 2952 detailed scientific investigation, the Portal delivers an
 2953 intuitive user experience, allowing users to visually ana-
 2954 lyze data while retaining access to underlying metadata
 2955 and query controls.

2956 6.4. Notebook Aspect

2957 The Notebook Aspect provides an interactive, web-
 2958 based environment built on Jupyter Notebooks, en-
 2959 abling users to write and execute Python code directly
 2960 on Rubin and LSST data without downloading it locally.
 2961 It offers programmatic access to Rubin and LSST data
 2962 products, allowing users to query and retrieve datasets,
 2963 manipulate and display images, compute derived prop-

erties, plot results, and reprocess data using the LSST Science Pipelines (§4.1). The environment comes pre-installed with the pipelines and a broad set of widely used astronomical *software* tools, supporting immediate and flexible data analysis.

6.5. Databases

The user-facing Aspects of the RSP are supported by several backend databases that store catalog data products, image metadata, and other derived datasets. The *schema* for DP1 and other Rubin databases are available online at <https://sdm-schemas.lsst.io>.

6.5.1. Qserv

The final 10-year LSST catalog is expected to reach 15 PB and contain measurements for billions of stars and galaxies across trillions of detections. To support efficient storage, querying, and analysis of this dataset, Rubin Observatory developed Qserv (D. L. Wang et al. 2011; F. Mueller et al. 2023) – a scalable, parallel, distributed SQL database system. Qserv partitions data over approximately equal-area regions of the celestial sphere, replicates data to ensure resilience and high availability, and uses shared scanning to reduce overall I/O load. It also supports a package of scientific user-defined functions (SciSQL: <https://smonkewitz.github.io/scisql/>) simplifying complex queries involving spherical geometry, statistics, and photometry. Qserv is built on robust production-quality components, including MariaDB (<https://www.mariadb.org/>) and XRootD (<https://xrootd.org/>). Qserv runs at the USDF and user access to catalog data is via the TAP service (§6.2.1). This enables catalog-based analysis through both the RSP Portal and Notebook Aspects.

Although the small DP1 dataset does not require Qserv’s full capabilities, we nevertheless chose to use it for DP1 to accurately reflect the future data access environment and to gain experience with scientifically-motivated queries ahead of full-scale deployment. Qserv is open-source and available on GitHub: <https://github.com/lsst/qserv>.

7. SUPPORT FOR COMMUNITY SCIENCE

The Rubin Observatory has a science community that encompasses thousands of individuals worldwide, with a broad range of experience and expertise in astronomy in general, and in the analysis of optical imaging data specifically.

Rubin’s model to support this diverse community to access and analyze DP1 emphasizes self-help via documentation and tutorials, and employs an open platform for asynchronous issue reporting that enables crowd-

sourced solutions. These two aspects of community support are augmented by virtual engagement activities. In addition, Rubin supports its Users Committee to advocate on behalf of the science community, and supports the eight LSST Science Collaborations (§7.6).

All of the resources for scientists that are discussed in this section are discoverable by browsing the *For Scientists* pages of the Rubin Observatory website¹⁰⁵.

7.1. Documentation

The data release documentation for DP1¹⁰⁶ provides an overview of the LSSTComCam observations, detailed descriptions of the data products, and a high-level summary of the processing pipelines. Although much of its content overlaps significantly with this paper, the documentation is presented as a searchable, web-based resource built using Sphinx¹⁰⁷, with a focus on enabling scientific use of the data products.

7.2. Tutorials

A suite of tutorials (NSF-DOE Vera C. Rubin Observatory 2021) that demonstrate how to access and analyze DP1 using the RSP accompanies the DP1 release¹⁰⁸. Jupyter Notebook tutorials are available via the “Tutorials” drop-down menu within the Notebook aspect of the RSP. Tutorials for the Portal and API aspects of the RSP can be found in the data release documentation.

These tutorials are designed to be inclusive, accessible, clear, focused, and consistent. Their format and contents follow a set of guidelines (M. L. Graham et al. 2026) that are informed by modern standards in technical writing.

7.3. Community Forum

The venue for all user support is the Rubin Community Forum¹⁰⁹. Questions about any and all aspects of the Rubin data products, pipelines, and services, including DP1, should be posted as new topics in the Support category. This includes beginner-level and “how-to” questions, advanced scientific analysis questions, technical bug reports, account and data access issues, and everything in between. The Support category of the Forum is monitored by Rubin staff, who follow an established internal workflow for following-up and resolving all reported issues.

¹⁰⁵ <https://rubinobservatory.org/for-scientists>

¹⁰⁶ <https://dp1.lsst.io>

¹⁰⁷ <https://www.sphinx-doc.org/>

¹⁰⁸ <https://dp1.lsst.io/tutorials>

¹⁰⁹ <https://community.lsst.org/>

The Rubin Community Forum is built on the open-source Discourse platform. It was chosen because, for a worldwide community of ten thousand Rubin users, a traditional (i.e., closed) help desk represents a risk to Rubin science (e.g., many users with the same question having to wait for responses). The open nature of the Forum enables self-help by letting users search for similar issues, and enables crowd-sourced problem solving (and avoids knowledge bottlenecks) by letting users help users.

The Rubin Community Forum, and the internal staff workflows for user support, were set up, tested, and refined with DP0 so that it was ready for use with DP1.

7.4. Engagement Activities

A variety of live virtual and in-person workshops and seminars offer learning opportunities to scientists and students working with the Rubin data products, services, and tools.

- Rubin Science Assemblies (weekly, virtual, 1 hour): alternates between hands-on tutorials based on the most recent data release and open drop-in “office hours” with Rubin staff.
- Rubin Data Academy (annual, virtual, 3-4 days): an intense set of hands-on tutorials based on the most recent data release, along with co-working and networking sessions.
- Rubin Community Workshop (annual, virtual, 5 days), a science-focused conference of contributed posters, talks, and sessions led by members of the Rubin science community and Rubin staff.

Following the release of DP1, all of these engagement activities focused on use of DP1 by the science community. In particular, the 2025 Rubin Data Academy was run the week of the DP1 release, in order to immediately facilitate community access. The 2025 Rubin Community Workshop had several sessions to introduce people to the DP1 dataset and demonstrate how to access and analyze it with the RSP.

For schedules, connection information, zoom recordings, and associated materials, visit the *For Scientists* pages of the Rubin Observatory website¹¹⁰. Requests for custom tutorials and presentations for research groups are also accommodated.

7.5. Users Committee

This committee is charged with soliciting feedback from the science community, advocating on their behalf,

and recommending science-driven improvements to the LSST data products and the Rubin Science Platform tools and services. Community members are encouraged to attend their virtual meetings and raise issues to their attention, so they can be included in the committee’s twice-yearly reports to the Rubin Observatory Director.

Like the Forum, the Users Committee was established and began its work with DP0, and that feedback was implemented for DP1. The community’s response to DP1 will be especially valuable input to DP2 and DR1, and the Users Committee encourages all users to interact with them. For a list of members and contact information, visit the *For Scientists* pages of the Rubin Observatory website.

7.6. Science Collaborations

The eight LSST Science Collaborations are independent, worldwide communities of scientists, self-organized into collaborations based on their research interests and expertise. Members work together to apply for funding, build software infrastructure and analysis algorithms, and incorporate external data sets into their LSST-based research.

The Science Collaborations also provide valuable advice to Rubin Observatory on the operational strategies and data products to accomplish specific science goals, and Rubin Observatory supports the collaborations via staff liaisons and regular virtual meetings with Rubin operations leadership.

The Science Collaborations have been functioning for many years, and their engagement and feedback on DP0 was implemented into the community science model for DP1, as it will for future data releases.

8. SUMMARY AND FUTURE RELEASES

Rubin Data Preview 1 offers an initial look at the first on-sky data products and access services from the Vera C. Rubin Observatory. DP1 forms part of Rubin’s Early Science Program, and provides the scientific community with an early opportunity to familiarize themselves with the data formats and access infrastructure for the forthcoming Legacy Survey of Space and Time. This early release has a proprietary period of two years, during which time it is available to Rubin data rights holders only via the cloud-based RSP.

In this paper we have described the completion status of the observatory at the time of data acquisition, the commissioning campaign that forms the basis of DP1, and the processing pipelines used to produce early versions of data products. We provide details on the data products, their characteristics and known issues, and

¹¹⁰ <https://rubinobservatory.org/for-scientists/events-deadlines>

3152 describe the Rubin Science Platform for access to and
3153 analysis of DP1.

3154 The data products described in this paper derive from
3155 observations obtained by LSSTComCam. LSSTCom-
3156 Cam contains only around 5% the number of CCDs as
3157 the full LSST Science Camera (LSSTCam), yet the DP1
3158 dataset that it has produced will already enable a very
3159 broad range of science. At 3.5 TB in size, DP1 covers
3160 a total area of ~ 15 deg² and contains 1792 single-epoch
3161 images, 2644 deep coadded images and 2.3 million dis-
3162 tinct astrophysical objects, including 93 new asteroid
3163 discoveries.

3164 While some data products anticipated from the LSST
3165 are not yet available, e.g., cell-based coadds, DP1 in-
3166 cludes several products that will not be provided in fu-
3167 ture releases. Notably, difference images are included in
3168 DP1 as pre-generated products; in future releases, these
3169 will instead be generated on demand via dedicated ser-
3170 vices. The inclusion of pre-generated difference images
3171 in DP1 is feasible due to the relatively small size of the
3172 dataset, an approach that will not scale to the signifi-
3173 cantly larger data volumes expected in subsequent re-
3174 leases.

3175 The RSP is continually under development, and new
3176 functionality will continue to be deployed incrementally
3177 as it becomes available, and independent of the future
3178 data release schedule. User query history capabilities,
3179 context-aware documentation and a bulk cutout services
3180 are just a few of the services currently under develop-
3181 ment.

3182 Coincident with the release of DP1, Rubin Obser-
3183 vatory begins its Science Validation Surveys with the
3184 LSST Science Camera (i.e., LSSTCam). This final com-
3185 missioning phase will produce a dataset that will form
3186 the foundation for the second Rubin Data Preview, DP2.
3187 Full operations, marking the start of the LSST, are ex-
3188 pected to commence in 2026.

ACKNOWLEDGMENTS

3189 . This material is based upon work supported in part by
3190 the National Science Foundation through Cooperative
3191 Agreements AST-1258333 and AST-2241526 and Co-
3192 operative Support Agreements AST-1202910 and AST-
3193 2211468 managed by the Association of Universities for
3194 Research in Astronomy (AURA), and the Department of
3195 Energy under Contract No. DE-AC02-76SF00515 with
3196 the SLAC National Accelerator Laboratory managed
3197 by Stanford University. Additional Rubin Observatory
3198 funding comes from private donations, grants to univer-
3199 sities, and in-kind support from LSST-DA Institutional
3200 Members.
3201

3202 This work has been supported by the French Na-
3203 tional Institute of Nuclear and Particle Physics (IN2P3)
3204 through dedicated funding provided by the National
3205 Center for Scientific Research (CNRS).

3206 This work has been supported by STFC fund-
3207 ing for UK participation in LSST, through grant
3208 ST/Y00292X/1.

3209 *Facilities:* Rubin:Simonyi (LSSTComCam), Ru-
3210 bin:USDAC

3211 *Software:* Rubin Data Butler (T. Jenness et al.
3212 2022), LSST Science Pipelines (Rubin Observatory Sci-
3213 ence Pipelines Developers 2025), LSST Feature Based
3214 Scheduler v3.0 (P. Yoachim et al. 2024; E. Naghib et al.
3215 2019) Astropy (Astropy Collaboration et al. 2013, 2018,
3216 2022) PIFF (M. Jarvis et al. 2021), GBDES (G. M.
3217 Bernstein 2022), Qserv (D. L. Wang et al. 2011; F.
3218 Mueller et al. 2023), Slurm, HTCondor, CVMFS, FTS3,
3219 ESNNet

APPENDIX

REFERENCES

- 3221 Abazajian, K., Adelman-McCarthy, J. K., Agüeros, M. A.,
3222 et al. 2004, AJ, 128, 502, doi: [10.1086/421365](https://doi.org/10.1086/421365)
- 3223 Ahumada, R., Allende Prieto, C., Almeida, A., et al. 2020,
3224 ApJS, 249, 3, doi: [10.3847/1538-4365/ab929e](https://doi.org/10.3847/1538-4365/ab929e)
- 3225 Aihara, H., AlSayyad, Y., Ando, M., et al. 2022, PASJ, 74,
3226 247, doi: [10.1093/pasj/psab122](https://doi.org/10.1093/pasj/psab122)
- 3227 Allbery, R. 2023, IVOA SODA implementation experience,
3228 SQuARE Technical Note SQR-063, NSF-DOE Vera C.
3229 Rubin Observatory. <https://sqr-063.lsst.io/>
- 3230 Allbery, R. 2024, Draft IVOA SODA web service
3231 specification, SQuARE Technical Note SQR-093,
3232 NSF-DOE Vera C. Rubin Observatory.
3233 <https://sqr-093.lsst.io/>

- 3234 AlSayyad, Y. 2018, Coaddition Artifact Rejection and
3235 CompareWarp, Data Management Technical Note
3236 DMTN-080, NSF-DOE Vera C. Rubin Observatory,
3237 doi: [10.71929/rubin/2583441](https://doi.org/10.71929/rubin/2583441)
- 3238 Ansel, J., Yang, E., He, H., et al. 2024, in 29th ACM
3239 International Conference on Architectural Support for
3240 Programming Languages and Operating Systems, Volume
3241 2 (ASPLOS '24) (ACM), doi: [10.1145/3620665.3640366](https://doi.org/10.1145/3620665.3640366)
- 3242 Antilogus, P., Astier, P., Doherty, P., Guyonnet, A., &
3243 Regnault, N. 2014, Journal of Instrumentation, 9,
3244 C03048, doi: [10.1088/1748-0221/9/03/C03048](https://doi.org/10.1088/1748-0221/9/03/C03048)
- 3245 Astropy Collaboration, Robitaille, T. P., Tollerud, E. J.,
3246 et al. 2013, A&A, 558, A33,
3247 doi: [10.1051/0004-6361/201322068](https://doi.org/10.1051/0004-6361/201322068)
- 3248 Astropy Collaboration, Price-Whelan, A. M., Sipőcz, B. M.,
3249 et al. 2018, AJ, 156, 123, doi: [10.3847/1538-3881/aabc4f](https://doi.org/10.3847/1538-3881/aabc4f)
- 3250 Astropy Collaboration, Price-Whelan, A. M., Lim, P. L.,
3251 et al. 2022, ApJ, 935, 167, doi: [10.3847/1538-4357/ac7c74](https://doi.org/10.3847/1538-4357/ac7c74)
- 3252 Baumann, M., Boch, T., Pineau, F.-X., et al. 2022, in
3253 Astronomical Society of the Pacific Conference Series,
3254 Vol. 532, Astronomical Data Analysis Software and
3255 Systems XXX, ed. J. E. Ruiz, F. Pierfederici, &
3256 P. Teuben, 7
- 3257 Bechtol, K., Sevilla-Noarbe, I., Drlica-Wagner, A., et al.
3258 2025, arXiv e-prints, arXiv:2501.05739,
3259 doi: [10.48550/arXiv.2501.05739](https://doi.org/10.48550/arXiv.2501.05739)
- 3260 Berk, A., Anderson, G. P., Bernstein, L. S., et al. 1999, in
3261 Society of Photo-Optical Instrumentation Engineers
3262 (SPIE) Conference Series, Vol. 3756, Optical
3263 Spectroscopic Techniques and Instrumentation for
3264 Atmospheric and Space Research III, ed. A. M. Larar,
3265 348–353, doi: [10.1117/12.366388](https://doi.org/10.1117/12.366388)
- 3266 Bernstein, G. M. 2022, gbdes: DECam instrumental
3267 signature fitting and processing programs,, Astrophysics
3268 Source Code Library, record ascl:2210.011
3269 <http://ascl.net/2210.011>
- 3270 Bernstein, G. M., & Jarvis, M. 2002, AJ, 123, 583,
3271 doi: [10.1086/338085](https://doi.org/10.1086/338085)
- 3272 Bernstein, G. M., Armstrong, R., Plazas, A. A., et al. 2017,
3273 PASP, 129, 074503, doi: [10.1088/1538-3873/aa6c55](https://doi.org/10.1088/1538-3873/aa6c55)
- 3274 Bertin, E. 2011, in Astronomical Society of the Pacific
3275 Conference Series, Vol. 442, Astronomical Data Analysis
3276 Software and Systems XX, ed. I. N. Evans,
3277 A. Accomazzi, D. J. Mink, & A. H. Rots, 435
- 3278 Bianco, F. B., Ivezić, Ž., Jones, R. L., et al. 2022, ApJS,
3279 258, 1, doi: [10.3847/1538-4365/ac3e72](https://doi.org/10.3847/1538-4365/ac3e72)
- 3280 Blum, R., & the Rubin Operations Team. 2020, Vera C.
3281 Rubin Observatory Data Policy, Data Management
3282 Operations Controlled Document RDO-013, NSF-DOE
3283 Vera C. Rubin Observatory. <https://ls.st/RDO-013>
- 3284 Boch, T., & Fernique, P. 2014, in Astronomical Society of
3285 the Pacific Conference Series, Vol. 485, Astronomical
3286 Data Analysis Software and Systems XXIII, ed.
3287 N. Manset & P. Forshay, 277
- 3288 Bonnarel, F., Dowler, P., Demleitner, M., Tody, D., &
3289 Dempsey, J. 2017, IVOA Server-side Operations for Data
3290 Access Version 1.0., IVOA Recommendation 17 May 2017
3291 doi: [10.5479/ADS/bib/2017ivoa.spec.0517B](https://doi.org/10.5479/ADS/bib/2017ivoa.spec.0517B)
- 3292 Bonnarel, F., Fernique, P., Bienaymé, O., et al. 2000,
3293 A&AS, 143, 33, doi: [10.1051/aas:2000331](https://doi.org/10.1051/aas:2000331)
- 3294 Bosch, J., Armstrong, R., Bickerton, S., et al. 2018, PASJ,
3295 70, S5, doi: [10.1093/pasj/psx080](https://doi.org/10.1093/pasj/psx080)
- 3296 Broughton, A., Utsumi, Y., Plazas Malagón, A. A., et al.
3297 2024, PASP, 136, 045003, doi: [10.1088/1538-3873/ad3aa2](https://doi.org/10.1088/1538-3873/ad3aa2)
- 3298 Burke, D. L., Rykoff, E. S., Allam, S., et al. 2018, AJ, 155,
3299 41, doi: [10.3847/1538-3881/aa9f22](https://doi.org/10.3847/1538-3881/aa9f22)
- 3300 Chambers, K. C., Magnier, E. A., Metcalfe, N., et al. 2016,
3301 arXiv e-prints, arXiv:1612.05560,
3302 doi: [10.48550/arXiv.1612.05560](https://doi.org/10.48550/arXiv.1612.05560)
- 3303 Choi, Y., Olsen, K. A. G., Carlin, J. L., et al. 2025, arXiv
3304 e-prints, arXiv:2507.01343,
3305 doi: [10.48550/arXiv.2507.01343](https://doi.org/10.48550/arXiv.2507.01343)
- 3306 de Vaucouleurs, G. 1948, Annales d'Astrophysique, 11, 247
- 3307 de Vaucouleurs, G. 1953, MNRAS, 113, 134,
3308 doi: [10.1093/mnras/113.2.134](https://doi.org/10.1093/mnras/113.2.134)
- 3309 Dowler, P., Bonnarel, F., & Tody, D. 2015, IVOA Simple
3310 Image Access Version 2.0., IVOA Recommendation 23
3311 December 2015
3312 doi: [10.5479/ADS/bib/2015ivoa.spec.1223D](https://doi.org/10.5479/ADS/bib/2015ivoa.spec.1223D)
- 3313 Dowler, P., Rixon, G., Tody, D., & Demleitner, M. 2019,
3314 Table Access Protocol Version 1.1., IVOA
3315 Recommendation 27 September 2019
3316 doi: [10.5479/ADS/bib/2019ivoa.spec.0927D](https://doi.org/10.5479/ADS/bib/2019ivoa.spec.0927D)
- 3317 Eggl, S., Juric, M., Moeyens, J., & Jones, L. 2020, in
3318 AAS/Division for Planetary Sciences Meeting Abstracts,
3319 Vol. 52, AAS/Division for Planetary Sciences Meeting
3320 Abstracts, 211.01
- 3321 Esteves, J. H., Utsumi, Y., Snyder, A., et al. 2023, PASP,
3322 135, 115003, doi: [10.1088/1538-3873/ad0a73](https://doi.org/10.1088/1538-3873/ad0a73)
- 3323 Euclid Collaboration, Romelli, E., Kümmel, M., et al. 2025,
3324 arXiv e-prints, arXiv:2503.15305,
3325 doi: [10.48550/arXiv.2503.15305](https://doi.org/10.48550/arXiv.2503.15305)
- 3326 Fagrelus, P., & Rykoff, E. S. 2025, Rubin Observatory
3327 Baseline Calibration Plan, Commissioning Technical
3328 Note SITCOMTN-086, NSF-DOE Vera C. Rubin
3329 Observatory, doi: [10.71929/rubin/2583850](https://doi.org/10.71929/rubin/2583850)

- 3330 Ferguson, P. S., Rykoff, E. S., Carlin, J. L., Saunders, C., &
3331 Parejko, J. K. 2025, The Monster: A reference catalog
3332 with synthetic ugrizy-band fluxes for the Vera C. Rubin
3333 observatory, Data Management Technical Note
3334 DMTN-277, NSF-DOE Vera C. Rubin Observatory,
3335 doi: [10.71929/rubin/2583688](https://doi.org/10.71929/rubin/2583688)
- 3336 Fernique, P., Allen, M. G., Boch, T., et al. 2015, *A&A*, 578,
3337 A114, doi: [10.1051/0004-6361/201526075](https://doi.org/10.1051/0004-6361/201526075)
- 3338 Fernique, P., Allen, M., Boch, T., et al. 2017, HiPS -
3339 Hierarchical Progressive Survey Version 1.0., IVOA
3340 Recommendation 19 May 2017
3341 doi: [10.5479/ADS/bib/2017ivoa.spec.0519F](https://doi.org/10.5479/ADS/bib/2017ivoa.spec.0519F)
- 3342 Fortino, W. F., Bernstein, G. M., Bernardinelli, P. H., et al.
3343 2021, *AJ*, 162, 106, doi: [10.3847/1538-3881/ac0722](https://doi.org/10.3847/1538-3881/ac0722)
- 3344 Gaia Collaboration, Montegriffo, P., Bellazzini, M., et al.
3345 2023a, *A&A*, 674, A33,
3346 doi: [10.1051/0004-6361/202243709](https://doi.org/10.1051/0004-6361/202243709)
- 3347 Gaia Collaboration, Vallenari, A., Brown, A. G. A., et al.
3348 2023b, *A&A*, 674, A1, doi: [10.1051/0004-6361/202243940](https://doi.org/10.1051/0004-6361/202243940)
- 3349 Górski, K. M., Hivon, E., Banday, A. J., et al. 2005, *ApJ*,
3350 622, 759, doi: [10.1086/427976](https://doi.org/10.1086/427976)
- 3351 Graham, A. W., & Driver, S. P. 2005, *PASA*, 22, 118,
3352 doi: [10.1071/AS05001](https://doi.org/10.1071/AS05001)
- 3353 Graham, M., Plante, R., Tody, D., & Fitzpatrick, M. 2014,
3354 *PyVO: Python access to the Virtual Observatory*,
3355 *Astrophysics Source Code Library*, record ascl:1402.004
- 3356 Graham, M. L., Carlin, J. L., Adair, C. L., et al. 2026,
3357 *Guidelines for User Tutorials*, Technical Note RTN-045,
3358 NSF-DOE Vera C. Rubin Observatory,
3359 doi: [10.71929/rubin/2584020](https://doi.org/10.71929/rubin/2584020)
- 3360 Gray, B. 2025, *find_orb: Orbit determination from*
3361 *observations*, https://github.com/Bill-Gray/find_orb
- 3362 Guy, L. P., Bechtol, K., Bellm, E., et al. 2026, Rubin
3363 Observatory Plans for an Early Science Program,
3364 Technical Note RTN-011, NSF-DOE Vera C. Rubin
3365 Observatory, doi: [10.71929/rubin/2584021](https://doi.org/10.71929/rubin/2584021)
- 3366 Heinze, A., Eggl, S., Juric, M., et al. 2022, in *AAS/Division*
3367 *for Planetary Sciences Meeting Abstracts*, Vol. 54,
3368 *AAS/Division for Planetary Sciences Meeting Abstracts*,
3369 504.04
- 3370 Heinze, A., Juric, M., & Kurlander, J. 2023, *heliolinx: Open*
3371 *Source Solar System Discovery Software*,
3372 <https://github.com/heliolinx/heliolinx>
- 3373 Hirata, C., & Seljak, U. 2003, *MNRAS*, 343, 459,
3374 doi: [10.1046/j.1365-8711.2003.06683.x](https://doi.org/10.1046/j.1365-8711.2003.06683.x)
- 3375 Holman, M. J., Payne, M. J., Blankley, P., Janssen, R., &
3376 Kuindersma, S. 2018, *AJ*, 156, 135,
3377 doi: [10.3847/1538-3881/aad69a](https://doi.org/10.3847/1538-3881/aad69a)
- 3378 Howard, J., Reil, K., Claver, C., et al. 2018, in *Society of*
3379 *Photo-Optical Instrumentation Engineers (SPIE)*
3380 *Conference Series*, Vol. 10700, *Ground-based and*
3381 *Airborne Telescopes VII*, ed. H. K. Marshall &
3382 J. Spyromilio, 107003D, doi: [10.1117/12.2312684](https://doi.org/10.1117/12.2312684)
- 3383 Illingworth, G., Magee, D., Bouwens, R., et al. 2016, *arXiv*
3384 *e-prints*, arXiv:1606.00841,
3385 doi: [10.48550/arXiv.1606.00841](https://doi.org/10.48550/arXiv.1606.00841)
- 3386 Ingraham, P., Fagrelus, P., Stubbs, C. W., et al. 2022, in
3387 *Society of Photo-Optical Instrumentation Engineers*
3388 *(SPIE) Conference Series*, Vol. 12182, *Ground-based and*
3389 *Airborne Telescopes IX*, ed. H. K. Marshall,
3390 J. Spyromilio, & T. Usuda, 121820R,
3391 doi: [10.1117/12.2630185](https://doi.org/10.1117/12.2630185)
- 3392 Ivezić, Ž., Kahn, S. M., Tyson, J. A., et al. 2019a, *ApJ*,
3393 873, 111, doi: [10.3847/1538-4357/ab042c](https://doi.org/10.3847/1538-4357/ab042c)
- 3394 Ivezić, Ž., Kahn, S. M., Tyson, J. A., et al. 2019b, *ApJ*,
3395 873, 111, doi: [10.3847/1538-4357/ab042c](https://doi.org/10.3847/1538-4357/ab042c)
- 3396 Jarvis, M., et al. 2021, *Mon. Not. Roy. Astron. Soc.*, 501,
3397 1282, doi: [10.1093/mnras/staa3679](https://doi.org/10.1093/mnras/staa3679)
- 3398 Jenness, T., & Dubois-Felsmann, G. P. 2025, IVOA
3399 Identifier Usage at the Rubin Observatory, Data
3400 Management Technical Note DMTN-302, NSF-DOE Vera
3401 C. Rubin Observatory, doi: [10.71929/rubin/2583848](https://doi.org/10.71929/rubin/2583848)
- 3402 Jenness, T., Voutsinas, S., Dubois-Felsmann, G. P., &
3403 Salnikov, A. 2024, *arXiv e-prints*, arXiv:2501.00544,
3404 doi: [10.48550/arXiv.2501.00544](https://doi.org/10.48550/arXiv.2501.00544)
- 3405 Jenness, T., Bosch, J. F., Salnikov, A., et al. 2022, in
3406 *Society of Photo-Optical Instrumentation Engineers*
3407 *(SPIE) Conference Series*, Vol. 12189, *Software and*
3408 *Cyberinfrastructure for Astronomy VII*, 1218911,
3409 doi: [10.1117/12.2629569](https://doi.org/10.1117/12.2629569)
- 3410 Jones, R. L., Yoachim, P., Ivezić, Ž., Neilsen Jr., E. H., &
3411 Ribeiro, T. 2021, *Survey Strategy and Cadence Choices*
3412 *for the Vera C. Rubin Observatory Legacy Survey of*
3413 *Space and Time (LSST)*, Project Science Technical Note
3414 PSTN-051, NSF-DOE Vera C. Rubin Observatory,
3415 doi: [10.71929/rubin/2584084](https://doi.org/10.71929/rubin/2584084)
- 3416 Juric, M. 2025, *mpsky: Multi-purpose sky catalog*
3417 *cross-matching*, <https://github.com/mjuric/mpsky>
- 3418 Jurić, M., Ciardi, D., Dubois-Felsmann, G., & Guy, L.
3419 2019, *LSST Science Platform Vision Document*, Systems
3420 *Engineering Controlled Document LSE-319*, NSF-DOE
3421 Vera C. Rubin Observatory, doi: [10.71929/rubin/2587242](https://doi.org/10.71929/rubin/2587242)
- 3422 Jurić, M., Axelrod, T. S., Becker, A. C., et al. 2023, *Data*
3423 *Products Definition Document*, Systems Engineering
3424 *Controlled Document LSE-163*, NSF-DOE Vera C. Rubin
3425 Observatory, doi: [10.71929/rubin/2587118](https://doi.org/10.71929/rubin/2587118)

- 3426 Kannawadi, A. 2025, Consistent galaxy colors with
 3427 Gaussian-Aperture and PSF photometry, Data
 3428 Management Technical Note DMTN-190, NSF-DOE Vera
 3429 C. Rubin Observatory, doi: [10.71929/rubin/2583849](https://doi.org/10.71929/rubin/2583849)
- 3430 Kron, R. G. 1980, *ApJS*, 43, 305, doi: [10.1086/190669](https://doi.org/10.1086/190669)
- 3431 Kuijken, K. 2008, *A&A*, 482, 1053,
 3432 doi: [10.1051/0004-6361:20066601](https://doi.org/10.1051/0004-6361:20066601)
- 3433 Lange, T., Nordby, M., Pollek, H., et al. 2024, in *Society of
 3434 Photo-Optical Instrumentation Engineers (SPIE)
 3435 Conference Series*, Vol. 13096, Ground-based and
 3436 Airborne Instrumentation for Astronomy X, ed. J. J.
 3437 Bryant, K. Motohara, & J. R. D. Vernet, 130961O,
 3438 doi: [10.1117/12.3019302](https://doi.org/10.1117/12.3019302)
- 3439 Léget, P. F., Astier, P., Regnault, N., et al. 2021, *A&A*,
 3440 650, A81, doi: [10.1051/0004-6361/202140463](https://doi.org/10.1051/0004-6361/202140463)
- 3441 Lim, K.-T. 2023, Proposal and Prototype for Prompt
 3442 Processing, Data Management Technical Note
 3443 DMTN-219, NSF-DOE Vera C. Rubin Observatory,
 3444 doi: [10.71929/rubin/2585429](https://doi.org/10.71929/rubin/2585429)
- 3445 Louys, M., Tody, D., Dowler, P., et al. 2017, Observation
 3446 Data Model Core Components, its Implementation in the
 3447 Table Access Protocol Version 1.1., IVOA
 3448 Recommendation 09 May 2017
 3449 doi: [10.5479/ADS/bib/2017ivoa.spec.0509L](https://doi.org/10.5479/ADS/bib/2017ivoa.spec.0509L)
- 3450 LSST Dark Energy Science Collaboration (LSST DESC),
 3451 Abolfathi, B., Alonso, D., et al. 2021, *ApJS*, 253, 31,
 3452 doi: [10.3847/1538-4365/abd62c](https://doi.org/10.3847/1538-4365/abd62c)
- 3453 Lupton, R., Blanton, M. R., Fekete, G., et al. 2004, *PASP*,
 3454 116, 133, doi: [10.1086/382245](https://doi.org/10.1086/382245)
- 3455 Lust, N. B., Jenness, T., Bosch, J. F., et al. 2023, *arXiv
 3456 e-prints*, arXiv:2303.03313,
 3457 doi: [10.48550/arXiv.2303.03313](https://doi.org/10.48550/arXiv.2303.03313)
- 3458 Mandelbaum, R., Hirata, C. M., Seljak, U., et al. 2005,
 3459 *MNRAS*, 361, 1287,
 3460 doi: [10.1111/j.1365-2966.2005.09282.x](https://doi.org/10.1111/j.1365-2966.2005.09282.x)
- 3461 Megias Homar, G., Kahn, S. M., Meyers, J. M., Crenshaw,
 3462 J. F., & Thomas, S. J. 2024, *The Astrophysical Journal*,
 3463 974, 108, doi: [10.3847/1538-4357/ad6cdc](https://doi.org/10.3847/1538-4357/ad6cdc)
- 3464 Megias Homar, G., Tighe, R., Thomas, S., et al. 2024, in
 3465 *Ground-based and Airborne Telescopes X*, ed. H. K.
 3466 Marshall, J. Spyromilio, & T. Usuda, Vol. 13094,
 3467 International Society for Optics and Photonics (SPIE),
 3468 130943C, doi: [10.1117/12.3019031](https://doi.org/10.1117/12.3019031)
- 3469 Melchior, P., Moolekamp, F., Jerdee, M., et al. 2018,
 3470 *Astronomy and Computing*, 24, 129,
 3471 doi: [10.1016/j.ascom.2018.07.001](https://doi.org/10.1016/j.ascom.2018.07.001)
- 3472 Mueller, F., et al. 2023, in *ASP Conf. Ser.*, Vol. TBD,
 3473 ADASS XXXII, ed. S. Gaudet, S. Gwyn, P. Dowler,
 3474 D. Bohlender, & A. Hincks (San Francisco: ASP), in
 3475 press. <https://dmtn-243.lsst.io>
- 3476 Naghib, E., Yoachim, P., Vanderbei, R. J., Connolly, A. J.,
 3477 & Jones, R. L. 2019, *The Astronomical Journal*, 157, 151,
 3478 doi: [10.3847/1538-3881/aafece](https://doi.org/10.3847/1538-3881/aafece)
- 3479 NSF-DOE Vera C. Rubin Observatory. 2021, *Rubin
 3480 Observatory LSST Tutorials [Computer Software]*,
 3481 NSF-DOE Vera C. Rubin Observatory,
 3482 doi: [10.11578/rubin/dc.20250909.20](https://doi.org/10.11578/rubin/dc.20250909.20)
- 3483 NSF-DOE Vera C. Rubin Observatory. 2025a, *Legacy
 3484 Survey of Space and Time Data Preview 1 [Data set]*,
 3485 NSF-DOE Vera C. Rubin Observatory,
 3486 doi: [10.71929/RUBIN/2570308](https://doi.org/10.71929/RUBIN/2570308)
- 3487 NSF-DOE Vera C. Rubin Observatory. 2025b, *Legacy
 3488 Survey of Space and Time Data Preview 1: raw dataset
 3489 type [Data set]*, NSF-DOE Vera C. Rubin Observatory,
 3490 doi: [10.71929/RUBIN/2570310](https://doi.org/10.71929/RUBIN/2570310)
- 3491 NSF-DOE Vera C. Rubin Observatory. 2025c, *Legacy
 3492 Survey of Space and Time Data Preview 1: visit_image
 3493 dataset type [Data set]*, NSF-DOE Vera C. Rubin
 3494 Observatory, doi: [10.71929/RUBIN/2570311](https://doi.org/10.71929/RUBIN/2570311)
- 3495 NSF-DOE Vera C. Rubin Observatory. 2025d, *Legacy
 3496 Survey of Space and Time Data Preview 1:
 3497 template_coadd dataset type [Data set]*, NSF-DOE Vera
 3498 C. Rubin Observatory, doi: [10.71929/RUBIN/2570314](https://doi.org/10.71929/RUBIN/2570314)
- 3499 NSF-DOE Vera C. Rubin Observatory. 2025e, *Legacy
 3500 Survey of Space and Time Data Preview 1:
 3501 difference_image dataset type [Data set]*, NSF-DOE Vera
 3502 C. Rubin Observatory, doi: [10.71929/RUBIN/2570312](https://doi.org/10.71929/RUBIN/2570312)
- 3503 NSF-DOE Vera C. Rubin Observatory. 2025f, *Legacy
 3504 Survey of Space and Time Data Preview 1: Source
 3505 searchable catalog [Data set]*, NSF-DOE Vera C. Rubin
 3506 Observatory, doi: [10.71929/RUBIN/2570323](https://doi.org/10.71929/RUBIN/2570323)
- 3507 NSF-DOE Vera C. Rubin Observatory. 2025g, *Legacy
 3508 Survey of Space and Time Data Preview 1: Object
 3509 searchable catalog [Data set]*, NSF-DOE Vera C. Rubin
 3510 Observatory, doi: [10.71929/RUBIN/2570325](https://doi.org/10.71929/RUBIN/2570325)
- 3511 NSF-DOE Vera C. Rubin Observatory. 2025h, *Legacy
 3512 Survey of Space and Time Data Preview 1: ForcedSource
 3513 searchable catalog [Data set]*, NSF-DOE Vera C. Rubin
 3514 Observatory, doi: [10.71929/RUBIN/2570327](https://doi.org/10.71929/RUBIN/2570327)
- 3515 NSF-DOE Vera C. Rubin Observatory. 2025i, *Legacy
 3516 Survey of Space and Time Data Preview 1: DiaSource
 3517 searchable catalog [Data set]*, NSF-DOE Vera C. Rubin
 3518 Observatory, doi: [10.71929/RUBIN/2570317](https://doi.org/10.71929/RUBIN/2570317)
- 3519 NSF-DOE Vera C. Rubin Observatory. 2025j, *Legacy
 3520 Survey of Space and Time Data Preview 1: DiaObject
 3521 searchable catalog [Data set]*, NSF-DOE Vera C. Rubin
 3522 Observatory, doi: [10.71929/RUBIN/2570319](https://doi.org/10.71929/RUBIN/2570319)

- 3523 NSF-DOE Vera C. Rubin Observatory. 2025k, Legacy
 3524 Survey of Space and Time Data Preview 1:
 3525 ForcedSourceOnDiaObject searchable catalog [Data set],
 3526 NSF-DOE Vera C. Rubin Observatory,
 3527 doi: [10.71929/RUBIN/2570321](https://doi.org/10.71929/RUBIN/2570321)
- 3528 NSF-DOE Vera C. Rubin Observatory. 2025l, Legacy
 3529 Survey of Space and Time Data Preview 1: SSOBJect
 3530 searchable catalog [Data set], NSF-DOE Vera C. Rubin
 3531 Observatory, doi: [10.71929/RUBIN/2570335](https://doi.org/10.71929/RUBIN/2570335)
- 3532 NSF-DOE Vera C. Rubin Observatory. 2025m, Legacy
 3533 Survey of Space and Time Data Preview 1: SSSource
 3534 searchable catalog [Data set], NSF-DOE Vera C. Rubin
 3535 Observatory, doi: [10.71929/RUBIN/2570333](https://doi.org/10.71929/RUBIN/2570333)
- 3536 NSF-DOE Vera C. Rubin Observatory. 2025n, Legacy
 3537 Survey of Space and Time Data Preview 1: CcdVisit
 3538 searchable catalog [Data set], NSF-DOE Vera C. Rubin
 3539 Observatory, doi: [10.71929/RUBIN/2570331](https://doi.org/10.71929/RUBIN/2570331)
- 3540 NSF-DOE Vera C. Rubin Observatory. 2025o, Legacy
 3541 Survey of Space and Time Data Preview 1: survey
 3542 property dataset type [Data set], NSF-DOE Vera C.
 3543 Rubin Observatory, doi: [10.71929/RUBIN/2570315](https://doi.org/10.71929/RUBIN/2570315)
- 3544 Oke, J. B., & Gunn, J. E. 1983, *ApJ*, 266, 713,
 3545 doi: [10.1086/160817](https://doi.org/10.1086/160817)
- 3546 O'Mullane, W., Economou, F., Huang, F., et al. 2024a, in
 3547 *Astronomical Society of the Pacific Conference Series*,
 3548 Vol. 535, *Astronomical Data Analysis Software and Systems*
 3549 XXXI, ed. B. V. Hugo, R. Van Rooyen, & O. M.
 3550 Smirnov, 227, doi: [10.48550/arXiv.2111.15030](https://doi.org/10.48550/arXiv.2111.15030)
- 3551 O'Mullane, W., AlSaiyad, Y., Chiang, J., et al. 2024b, in
 3552 *Society of Photo-Optical Instrumentation Engineers*
 3553 (SPIE) Conference Series, Vol. 13101, *Software and*
 3554 *Cyberinfrastructure for Astronomy VIII*, ed. J. Ibsen &
 3555 G. Chiozzi, 131012B, doi: [10.1117/12.3018005](https://doi.org/10.1117/12.3018005)
- 3556 Onken, C. A., Wolf, C., Bessell, M. S., et al. 2019, *PASA*,
 3557 36, e033, doi: [10.1017/pasa.2019.27](https://doi.org/10.1017/pasa.2019.27)
- 3558 Park, H. Y., Nomerotski, A., & Tsybychev, D. 2017,
 3559 *Journal of Instrumentation*, 12, C05015,
 3560 doi: [10.1088/1748-0221/12/05/C05015](https://doi.org/10.1088/1748-0221/12/05/C05015)
- 3561 Petrosian, V. 1976, *ApJL*, 210, L53,
 3562 doi: [10.1086/18230110.1086/182253](https://doi.org/10.1086/18230110.1086/182253)
- 3563 Plazas, A. A., Shapiro, C., Smith, R., Huff, E., & Rhodes,
 3564 J. 2018, *Publications of the Astronomical Society of the*
 3565 *Pacific*, 130, 065004, doi: [10.1088/1538-3873/aab820](https://doi.org/10.1088/1538-3873/aab820)
- 3566 Plazas Malagón, A. A., Digel, S. W., Roodman, A.,
 3567 Broughton, A., & LSST Camera Team. 2025, *LSSTCam*
 3568 *and LSSTComCam Focal Plane Layouts*, Camera
 3569 Technical Note CTN-001, NSF-DOE Vera C. Rubin
 3570 Observatory, doi: [10.71929/rubin/2584019](https://doi.org/10.71929/rubin/2584019)
- 3571 Plazas Malagón, A. A., Waters, C., Broughton, A., et al.
 3572 2025, *Journal of Astronomical Telescopes, Instruments,*
 3573 *and Systems*, 11, 011209,
 3574 doi: [10.1117/1.JATIS.11.1.011209](https://doi.org/10.1117/1.JATIS.11.1.011209)
- 3575 Porter, M. N., Tucker, D. L., Smith, J. A., & Adair, C. L.
 3576 2025, *Photometric Transformation Relations for the*
 3577 *LSST Data Preview 1*, Technical Note RTN-099,
 3578 NSF-DOE Vera C. Rubin Observatory,
 3579 doi: [10.71929/rubin/3006074](https://doi.org/10.71929/rubin/3006074)
- 3580 Refregier, A. 2003, *ARA&A*, 41, 645,
 3581 doi: [10.1146/annurev.astro.41.111302.102207](https://doi.org/10.1146/annurev.astro.41.111302.102207)
- 3582 Reiss, D. J., & Lupton, R. H. 2016, *Implementation of*
 3583 *Image Difference Decorrelation*, Data Management
 3584 Technical Note DMTN-021, NSF-DOE Vera C. Rubin
 3585 Observatory, doi: [10.71929/rubin/2586490](https://doi.org/10.71929/rubin/2586490)
- 3586 Roodman, A., Rasmussen, A., Bradshaw, A., et al. 2024, in
 3587 *Society of Photo-Optical Instrumentation Engineers*
 3588 (SPIE) Conference Series, Vol. 13096, *Ground-based and*
 3589 *Airborne Instrumentation for Astronomy X*, ed. J. J.
 3590 Bryant, K. Motohara, & J. R. D. Vernet, 130961S,
 3591 doi: [10.1117/12.3019698](https://doi.org/10.1117/12.3019698)
- 3592 Rubin, V. C., & Ford, Jr., W. K. 1970, *ApJ*, 159, 379,
 3593 doi: [10.1086/150317](https://doi.org/10.1086/150317)
- 3594 Rubin, V. C., Ford, Jr., W. K., & Thonnard, N. 1980, *ApJ*,
 3595 238, 471, doi: [10.1086/158003](https://doi.org/10.1086/158003)
- 3596 Rubin Observatory Science Pipelines Developers. 2025, *The*
 3597 *LSST Science Pipelines Software: Optical Survey*
 3598 *Pipeline Reduction and Analysis Environment*, Project
 3599 Science Technical Note PSTN-019, NSF-DOE Vera C.
 3600 Rubin Observatory, doi: [10.71929/rubin/2570545](https://doi.org/10.71929/rubin/2570545)
- 3601 Rubin's Survey Cadence Optimization Committee, Bauer,
 3602 F. E., Brough, S., et al. 2022, *Survey Cadence*
 3603 *Optimization Committee's Phase 1 Recommendation*,
 3604 Project Science Technical Note PSTN-053, NSF-DOE
 3605 Vera C. Rubin Observatory, doi: [10.71929/rubin/2584276](https://doi.org/10.71929/rubin/2584276)
- 3606 Rubin's Survey Cadence Optimization Committee, Bauer,
 3607 F. E., Bianco, F. B., et al. 2023, *Survey Cadence*
 3608 *Optimization Committee's Phase 2 Recommendations*,
 3609 Project Science Technical Note PSTN-055, NSF-DOE
 3610 Vera C. Rubin Observatory, doi: [10.71929/rubin/2585249](https://doi.org/10.71929/rubin/2585249)
- 3611 Rubin's Survey Cadence Optimization Committee, Bianco,
 3612 F. B., Jones, R. L., et al. 2025, *Survey Cadence*
 3613 *Optimization Committee's Phase 3 Recommendations*,
 3614 Project Science Technical Note PSTN-056, NSF-DOE
 3615 Vera C. Rubin Observatory, doi: [10.71929/rubin/2585402](https://doi.org/10.71929/rubin/2585402)
- 3616 Rykoff, E. S., Tucker, D. L., Burke, D. L., et al. 2023, *arXiv*
 3617 *e-prints*, arXiv:2305.01695,
 3618 doi: [10.48550/arXiv.2305.01695](https://doi.org/10.48550/arXiv.2305.01695)

- 3619 Saunders, C. 2024, Astrometric Calibration in the LSST
3620 Pipeline, Data Management Technical Note DMTN-266,
3621 NSF-DOE Vera C. Rubin Observatory,
3622 doi: [10.71929/rubin/2583846](https://doi.org/10.71929/rubin/2583846)
- 3623 Schutt, T., Jarvis, M., Roodman, A., et al. 2025, The Open
3624 Journal of Astrophysics, 8, 26, doi: [10.33232/001c.132299](https://doi.org/10.33232/001c.132299)
- 3625 Sérsic, J. L. 1963, Boletín de la Asociación Argentina de
3626 Astronomía La Plata Argentina, 6, 41
- 3627 Sersic, J. L. 1968, Atlas de Galaxias Australes (Cordoba,
3628 Argentina: Observatorio Astronomico)
- 3629 Shanks, T., Metcalfe, N., Chehade, B., et al. 2015,
3630 MNRAS, 451, 4238, doi: [10.1093/mnras/stv1130](https://doi.org/10.1093/mnras/stv1130)
- 3631 SLAC National Accelerator Laboratory, & NSF-DOE Vera
3632 C. Rubin Observatory. 2024, LSST Commissioning
3633 Camera, SLAC National Accelerator Laboratory (SLAC),
3634 Menlo Park, CA (United States),
3635 doi: [10.71929/RUBIN/2561361](https://doi.org/10.71929/RUBIN/2561361)
- 3636 Slater, C. T., Ivezić, Ž., & Lupton, R. H. 2020, AJ, 159, 65,
3637 doi: [10.3847/1538-3881/ab6166](https://doi.org/10.3847/1538-3881/ab6166)
- 3638 Smith, G. E. 2010, Rev. Mod. Phys., 82, 2307,
3639 doi: [10.1103/RevModPhys.82.2307](https://doi.org/10.1103/RevModPhys.82.2307)
- 3640 Stalder, B., Reil, K., Claver, C., et al. 2020, in Society of
3641 Photo-Optical Instrumentation Engineers (SPIE)
3642 Conference Series, Vol. 11447, Ground-based and
3643 Airborne Instrumentation for Astronomy VIII, ed. C. J.
3644 Evans, J. J. Bryant, & K. Motohara, 114470L,
3645 doi: [10.1117/12.2561132](https://doi.org/10.1117/12.2561132)
- 3646 Stalder, B., Reil, K., Aguilar, C., et al. 2022, in Society of
3647 Photo-Optical Instrumentation Engineers (SPIE)
3648 Conference Series, Vol. 12184, Ground-based and
3649 Airborne Instrumentation for Astronomy IX, ed. C. J.
3650 Evans, J. J. Bryant, & K. Motohara, 121840J,
3651 doi: [10.1117/12.2630184](https://doi.org/10.1117/12.2630184)
- 3652 Stalder, B., Munoz, F., Aguilar, C., et al. 2024, in Society
3653 of Photo-Optical Instrumentation Engineers (SPIE)
3654 Conference Series, Vol. 13094, Ground-based and
3655 Airborne Telescopes X, ed. H. K. Marshall, J. Spyromilio,
3656 & T. Usuda, 1309409, doi: [10.1117/12.3019266](https://doi.org/10.1117/12.3019266)
- 3657 Swinbank, J. D., Axelrod, T. S., Becker, A. C., et al. 2020,
3658 Data Management Science Pipelines Design, Data
3659 Management Controlled Document LDM-151, NSF-DOE
3660 Vera C. Rubin Observatory, doi: [10.71929/rubin/2587108](https://doi.org/10.71929/rubin/2587108)
- 3661 Taranu, D. S. 2025, The MultiProFit astronomical source
3662 modelling code, Data Management Technical Note
3663 DMTN-312, NSF-DOE Vera C. Rubin Observatory,
3664 doi: [10.71929/rubin/2584108](https://doi.org/10.71929/rubin/2584108)
- 3665 Taylor, M. 2011, TOPCAT: Tool for OPerations on
3666 Catalogues And Tables., Astrophysics Source Code
3667 Library, record ascl:1101.010
- 3668 Thomas, S., Connolly, A., Crenshaw, J. F., et al. 2023, in
3669 Adaptive Optics for Extremely Large Telescopes
3670 (AO4ELT7), 67, doi: [10.13009/AO4ELT7-2023-069](https://doi.org/10.13009/AO4ELT7-2023-069)
- 3671 Tonry, J. L., Denneau, L., Heinze, A. N., et al. 2018, PASP,
3672 130, 064505, doi: [10.1088/1538-3873/aabadf](https://doi.org/10.1088/1538-3873/aabadf)
- 3673 Wainer, T. M., Davenport, J. R. A., Bellm, E. C., et al.
3674 2025, Research Notes of the American Astronomical
3675 Society, 9, 171, doi: [10.3847/2515-5172/adecef](https://doi.org/10.3847/2515-5172/adecef)
- 3676 Wang, D. L., Monkewitz, S. M., Lim, K.-T., & Becla, J.
3677 2011, in State of the Practice Reports, SC '11 (New
3678 York, NY, USA: ACM), 12:1–12:11,
3679 doi: [10.1145/2063348.2063364](https://doi.org/10.1145/2063348.2063364)
- 3680 Waters, C. Z., Magnier, E. A., Price, P. A., et al. 2020,
3681 ApJS, 251, 4, doi: [10.3847/1538-4365/abb82b](https://doi.org/10.3847/1538-4365/abb82b)
- 3682 Whitaker, K. E., Ashas, M., Illingworth, G., et al. 2019,
3683 ApJS, 244, 16, doi: [10.3847/1538-4365/ab3853](https://doi.org/10.3847/1538-4365/ab3853)
- 3684 Wu, X., Roby, W., Goldian, T., et al. 2019, in Astronomical
3685 Society of the Pacific Conference Series, Vol. 521,
3686 Astronomical Data Analysis Software and Systems
3687 XXVI, ed. M. Molinaro, K. Shortridge, & F. Pasian, 32
- 3688 Xin, B., Claver, C., Liang, M., et al. 2015, ApOpt, 54,
3689 9045, doi: [10.1364/AO.54.009045](https://doi.org/10.1364/AO.54.009045)
- 3690 Yoachim, P. 2022, Survey Strategy: Rolling Cadence,
3691 Project Science Technical Note PSTN-052, NSF-DOE
3692 Vera C. Rubin Observatory, doi: [10.71929/rubin/2584109](https://doi.org/10.71929/rubin/2584109)
- 3693 Yoachim, P., Jones, L., Eric H. Neilsen, J., & Becker, M. R.
3694 2024, lsst/rubin_scheduler: v3.0.0, v3.0.0 Zenodo,
3695 doi: [10.5281/zenodo.13985198](https://doi.org/10.5281/zenodo.13985198)
- 3696 Zhang, T., Almoubayyed, H., Mandelbaum, R., et al. 2023,
3697 MNRAS, 520, 2328, doi: [10.1093/mnras/stac3350](https://doi.org/10.1093/mnras/stac3350)